



Virginia Commonwealth University  
**VCU Scholars Compass**

---

Theses and Dissertations

Graduate School

---

2023

# Investigating the Dynamics and Fragmentation of Nitroaromatic Radical Cations Through Femtosecond Time-Resolved Mass Spectrometry and Computational Chemistry

Hugo Andres Lopez Pena

Follow this and additional works at: <https://scholarscompass.vcu.edu/etd>

 Part of the [Physical Chemistry Commons](#)

© The Author

---

Downloaded from

<https://scholarscompass.vcu.edu/etd/7316>

This Dissertation is brought to you for free and open access by the Graduate School at VCU Scholars Compass. It has been accepted for inclusion in Theses and Dissertations by an authorized administrator of VCU Scholars Compass. For more information, please contact [libcompass@vcu.edu](mailto:libcompass@vcu.edu).

Virginia Commonwealth University

Doctoral Thesis

---

**Investigating the Dynamics and Fragmentation of Nitroaromatic  
Radical Cations Through Femtosecond Time-Resolved Mass  
Spectrometry and Computational Chemistry**

---

**Author:** *Hugo Andrés López Peña*

**Supervisor:** *Katharine M. Tibbetts*

*A thesis submitted in fulfillment of the requirements  
for the degree of Doctor of Philosophy  
in the*

Department of Chemistry

May 1st, 2023



# Abstract

Chemists have sought to control molecular dissociation with lasers for decades. Effective control of unimolecular dissociation was only achieved with the development of high-intensity ultrashort pulsed lasers and coherent control techniques that operate on timescales faster than vibrational energy redistribution, which occurs in a range of  $10^{-8}$  to  $10^{-13}$  seconds. In view of this, our lab has specialized in the study of polyatomic radical cations using femtosecond time-resolved mass spectrometry (FTRMS). The interest in radical cations stems from the fact that they are highly reactive species that contribute to many physical, chemical, and biological processes. For instance, radical cations and anions participate in shock initiation of detonated energetic materials used as explosives and propellants. In this regard, we have studied some nitroaromatic radical cations commonly used as models for energetic materials to obtain insights into their dynamic behavior. We will discuss some results involving the dynamics of vibrational wave packets and rearrangement/fragmentation pathways.

Concerning vibrational wave packet dynamics, we employed computational chemistry to predict the most efficient probe wavelength for our experimental measurements on nitrobenzene cation demonstrating the feasibility and convenience of this approach. We also investigated pump-probe control schemes to manipulate fragmentation product yields in *p*-nitrotoluene (PNT) cation.

Finally, we investigated the dissociation dynamics and fragmentation pathways of *o*-nitroaniline, a model compound for the military explosive 2,4,6-triamino-1,3,5-trinitrobenzene (TATB). This model seems to capture the hydrogen bonding features that lead to energetically unfavorable rearrangement/fragmentation pathways in TATB. We expect that our experimental and computational results provide insights into the inherent stability of this molecule that explains the low sensitivity (and therefore relatively high safety) of TATB as an explosive.

# Contents

<b>Abstract</b>	<b>i</b>
<b>1 Introduction</b>	<b>1</b>
1.1 Motivation . . . . .	1
1.2 Time-resolved spectroscopy and the pump-probe approach . . . . .	2
<b>2 A few concepts of dynamics in quantum systems</b>	<b>4</b>
2.1 Split-operator approach . . . . .	5
2.1.1 Harmonic potential . . . . .	7
2.2 Vibrational wave packet . . . . .	9
<b>3 Quantum chemistry methods</b>	<b>11</b>
3.1 Born–Oppenheimer approximation . . . . .	11
3.2 Slater determinants . . . . .	12
3.3 Categories of electronic structure methods . . . . .	13
3.4 Wave function theory methods . . . . .	13
3.4.1 Hartree–Fock method . . . . .	13
3.4.2 Coupled-cluster method . . . . .	17
3.5 Density functional theory methods . . . . .	19
3.5.1 Functionals . . . . .	21
3.6 Basis sets . . . . .	23
3.7 Excited state methods . . . . .	24
3.7.1 Time-dependent density functional theory . . . . .	24
3.7.2 Equation-of-motion coupled-cluster singles and doubles . . . . .	25
<b>4 Predicting the best probe for nitroaromatic cations</b>	<b>26</b>
4.1 Introduction . . . . .	26

4.2	Methods	28
4.2.1	Theory	28
4.2.2	Experiment	31
4.3	Results	33
4.3.1	Computational results	33
4.3.2	Pump-probe measurements	38
4.3.3	Quantitative analysis of oscillatory dynamics	40
4.3.4	Comparison of nitrobenzene and nitrotoluenes	42
4.4	Discussion	42
4.5	Conclusions	45
<b>5</b>	<b>Controlling fragmentation products with selective wave packet excitation</b>	<b>47</b>
5.1	Introduction	47
5.2	Materials and Methods	49
5.2.1	Experiments	49
5.2.2	Computations	50
5.3	Results	50
5.3.1	Pump-probe measurements	50
5.3.2	Coherent control of torsional wave packet excitation	54
5.3.3	Assignment of $650\text{ cm}^{-1}$ wave packet	56
5.4	Discussion	60
<b>6</b>	<b>Photodissociation dynamics of the unusually stable ONA Cation</b>	<b>64</b>
6.1	Introduction	64
6.2	Methods	66
6.2.1	Experiment	66
6.2.2	Theory	66
6.3	Results and Discussion	69
6.3.1	Electronic structure of ONA and $\text{ONA}^+$	69
6.3.2	FTRMS measurements	70
6.3.3	Molecular dynamics simulations	74
6.3.4	Dissociation pathways	76
6.4	Conclusions	80

<b>7</b>	<b>Conclusions and future work</b>	<b>82</b>
<b>A</b>		<b>85</b>
<b>B</b>		<b>96</b>
<b>C</b>		<b>102</b>
	<b>Bibliography</b>	<b>115</b>

# List of Figures

2.1	Evolution of a Gaussian function on a harmonic potential under the split-operator approach . . . . .	9
2.2	Schematic representation of the generation of a vibrational wave packet (WP) with an ultrashort laser pulse . . . . .	10
4.1	Experimental (black) and computed infrared spectra at the B3LYP/Def2TZVPP (red) and M06/Def2TZVPP (blue) levels of theory for NB. . . . .	30
4.2	Experimental UV-vis spectra for NB in methanol (black) and chloroform (dashed magenta) and comparison with computed spectra at the B3LYP/Def2TZVPP (red) and M06/Def2TZVPP (blue) levels of theory. . . .	31
4.3	Geometrical structures for neutral and cationic NB optimized at the B3LYP/Def2TZVPP level of theory. Bond lengths are in Å and torsional angles in degrees. . . . .	33
4.4	Potential energy surface corresponding to the C <sub>6</sub> H <sub>5</sub> -NO <sub>2</sub> bond stretching in NB cation calculated at the B3LYP/Def2TZVPP level of theory. Charges on each fragment are indicated at C-N distances of 1.45 Å and 6.50 Å. The estimation of the ZPE is shown as a dashed black line. The energies for 1300, 800, and 650 nm photons, relative to the ZPE, are shown as dark red, magenta, and orange dashed lines respectively. . . . .	34
4.5	(a) Potential energy surfaces for the ground ionic state D <sub>0</sub> and the first ten excited states D <sub>1</sub> through D <sub>10</sub> as a function of the C-C-N-O dihedral angle. Energies corresponding to 1300, 800 and 650 nm photons are shown for comparison. (b) Oscillator strengths between the ground ionic state D <sub>0</sub> and the excited states D <sub>1</sub> through D <sub>10</sub> as a function of the C-C-N-O dihedral angle. All the calculations were done at the B3LYP/Def2TZVPP level of theory. . . .	35

4.6	Calculated wave packet trajectories over the $D_0$ PES (red dots and line) using 0 (bright green dashed line), 0.03 (turquoise solid line), and 0.24 eV (dark green dotted line) of excess energy. . . . .	37
4.7	(a) Mass spectra of NB taken with 1300 nm pump only (dark red, bottom), 800 nm probe (magenta, middle), and 650 nm probe (orange, top) at 4 ps delay. (b) Difference mass spectra between the 800 nm and 650 nm probe spectra and pump-only spectrum in (a). The signals for parent ion $NB^+$ (red), $C_6H_5^+$ (blue), and $C_4H_3^+$ (green) are highlighted. . . . .	38
4.8	Transient ion signals from $NB^+$ obtained with (a) 800 nm and (b) 650 nm probe pulses. Probe intensity is $10^{13} \text{ W cm}^{-2}$ (top panels) and $10^{12} \text{ W cm}^{-2}$ (bottom panels). Insets magnify the 70–830 fs range to show the oscillations, curves within the inset have been shifted vertically to show oscillatory behavior more clearly. . . . .	39
4.9	Residual ion signals (left) and FFT power spectra (right). . . . .	41
4.10	Transient ion signals of parent ions $M^+$ (red and orange) and $[M-NO_2]^+$ (dark and light blue) for NB (a), 4-NT (b), 2-NT (c), and 3-NT (d). Bond dissociation energies (BDE) of the C–N bond calculated at the B3LYP/Def2TZVPP level for these four radical cations are also shown. . . . .	43
5.1	(A) Mass spectrum of $PNT^+$ taken with 1300 nm pump only (dark red) and the difference spectra relative to the pump-only spectrum taken with 800 nm (magenta), 650 nm (orange), and 400 nm (blue) probe pulses at the indicated delays. (B) Transient ion signals for $PNT^+$ , $C_7H_7^+$ , $C_5H_5^+$ , and $C_3H_3^+$ taken at each probe wavelength. Each signal is normalized to its yield at negative pump-probe delay. . . . .	52
5.2	(A) Oscillatory ion signals for $PNT^+$ and selected fragment ions obtained by subtracting off the incoherent contributions to signal fitting via eq C.1. (B) FFT amplitudes obtained from the signals in (A) with indicated frequencies at $80 \text{ cm}^{-1}$ and $650 \text{ cm}^{-1}$ (for 800 nm probe). . . . .	54

5.3	(A) Geometrical structures for optimized neutral and cationic PNT. Bond lengths are in Å and torsional angles in degrees. (B) Normal mode at 604.32 $\text{cm}^{-1}$ for the optimized PNT cation. The calculations were performed at the B3LYP/def2-TZVPP level of theory. . . . .	55
5.4	Computed potential energy surfaces (A) and oscillator strengths (B) for $\text{PNT}^+$ along the C–C–N–O dihedral angle. . . . .	57
5.5	Computed potential energy surfaces (A) and oscillator strengths (B) for $\text{PNT}^+$ along C–N bond distance under different C–C–N–O dihedral angles. . . . .	60
5.6	Fractional yields of $\text{PNT}^+$ , $\text{C}_7\text{H}_7^+$ , $\text{C}_5\text{H}_5^+$ , and $\text{C}_3\text{H}_3^+$ from eq 5.2 obtained using 800 nm, 650 nm, and 400 nm probe wavelengths at intensities from 2 – 15 $\text{TW cm}^{-2}$ . . . . .	62
6.1	Initial photochemical reaction pathways of ONA and TATB. . . . .	65
6.2	(a) Geometric structures of ONA at the $S_0$ and $D_0$ geometries calculated at the CAM-B3LYP/6-311+G* level. (b) Electronic excited states of $\text{ONA}^+$ at the $S_0$ and $D_0$ geometries calculated at the EOM-CCSD/6-311+G* level. (c) Oscillator strengths of transitions out of $D_0$ for $\text{ONA}^+$ at the $S_0$ and $D_0$ geometries, with approximate spectra of the probe wavelengths in FTRMS. . . . .	70
6.3	Mass spectrum of ONA taken with 1300 nm pump only (top) and difference spectra relative to the pump only spectrum taken with a 400 nm probe pulse at 100 fs delay (bottom). . . . .	71
6.4	Transient ion dynamics of $\text{ONA}^+$ with inset water cross correlation signal, and fragments from the direct pathway (blue/magenta), NNR pathway (green), and H transfer pathway (yellow/orange). The black dots are data points and solid lines are fits to eq (C6) . . . . .	73
6.5	$\text{ONA}^+$ under the $S_0$ geometry. The atoms show the corresponding labeling. . . . .	75
6.6	Sample trajectory. . . . .	76
6.7	Direct pathway for $\text{ONA}^+$ fragmentation calculated at the CAM-B3LYP/6-311+G* level of theory. . . . .	77
6.8	NNR pathway for $\text{ONA}^+$ fragmentation calculated at the CAM-B3LYP/6-311+G* level of theory. . . . .	78

6.9	First part of the H transfer pathway for $\text{ONA}^+$ fragmentation calculated at the CAM-B3LYP/6-311+G* level of theory. . . . .	79
6.10	Second part of the H transfer pathway for $\text{ONA}^+$ fragmentation calculated at the CAM-B3LYP/6-311+G* level of theory. . . . .	80
A1	Experimental (black) and computed infrared spectra using the B3LYP functional with different basis sets for NB. . . . .	85
A2	Experimental (black) and computed infrared spectra using the M06 functional with different basis sets for NB. . . . .	85
A3	Experimental (black) and computed UV-Vis spectra using the B3LYP and M06 functionals with different basis sets for NB. . . . .	86
A4	Ion signals (dots) of $\text{NB}^+$ (red) and $\text{C}_6\text{H}_5^+$ (blue) obtained with 650 nm probe pulses at $10^{12} \text{ W cm}^{-2}$ , with fits to eq 1 in Chapter 4 (black lines) and components $T_1$ , $T_2$ , and $T_3$ (solid, dotted, and dashed lines). $\text{C}_6\text{H}_5^+$ did not require a $T_3$ component. . . . .	86
A5	Mass spectra of NB (magenta), ONT (red), MNT (green), and PNT (blue) taken with 1300 nm pump only. . . . .	86
B1	Ion signal of $\text{O}_2$ versus pump-probe delay with Gaussian fit. The 70 fs FWHM for the cross-correlation is taken as the width of the 400 nm probe pulse because the 1300 nm pump pulse has width of $\sim 20$ fs. . . . .	96
B2	Transient ion signals from 1300 nm pump and 800 nm probe. The low-amplitude fast oscillations (highlighted by the magnification of ion signals and dotted lines) are less visible than using 1500 nm pump (Figures 1A and 2A). . . . .	97
B3	Transient ion signals and curve fitting to eq C.1 or B.2. Fit coefficients given in Tables S1–S3. . . . .	97
C1	Transients for each probe wavelength. . . . .	114

# List of Tables

4.1	Calculated adiabatic and vertical ionization energies for NB and comparison to experimental values in literature, in units of eV. Numbers within parentheses are signed errors with respect to experimental quantities. . . . .	30
4.2	Excitation energies (EE) and oscillator strengths ( $f$ ) for NB cation with $90^\circ$ C–C–N–O dihedral angle at the B3LYP/Def2TZVPP and EOM-EE-CCSD/6-311+G* levels of theory . . . . .	36
4.3	Coefficients for $\text{NB}^+$ transients fit to eq (C.1). $I$ : probe intensity in $\text{W cm}^{-2}$ . . . . .	40
5.1	Curve fitting coefficients for coherent dynamics of ion signals: oscillation amplitude ( $a$ ), coherent lifetime ( $T_1$ ), oscillation period ( $t$ ), and phase ( $\phi$ ). . . . .	53
5.2	Excitation energies (EE) and oscillator strengths ( $f$ ) for $\text{PNT}^+$ with a C–C–N–O dihedral angle of $87.4^\circ$ at the B3LYP/def2-TZVPP and EOM-EE-CCSD/6-311+G* levels of theory. . . . .	58
6.1	Calculated adiabatic and vertical ionization energies for ONA and comparison to experimental values in literature. $a$ Ref. <sup>1</sup> $b$ Ref. <sup>2</sup> . . . . .	67
A1	Geometric coordinates for neutral and cationic NB optimized at the B3LYP/Def2TZVPP level. . . . .	87
A2	Root-mean-square distance (RMSD) and modified RMSD (MRMSD, see definition on Chapter 4) between neutral and cationic NB optimized at the B3LYP/Def2TZVPP level. Values are given in Å. . . . .	87
A3	Calculated harmonic frequencies ( $\text{cm}^{-1}$ ) and intensities for NB using the B3LYP functional with different basis sets. . . . .	88
A4	Calculated harmonic frequencies ( $\text{cm}^{-1}$ ) and intensities for NB using the M06 functional with different basis sets. . . . .	89

A5	Calculated harmonic frequencies ( $\text{cm}^{-1}$ ) and intensities for NB cation using the B3LYP functional with different basis sets. . . . .	90
A6	Calculated harmonic frequencies ( $\text{cm}^{-1}$ ) and intensities for NB cation using the M06 functional with different basis sets. . . . .	91
A7	Calculated excitation energies (eV) and oscillator strengths (a.u.) for NB using the B3LYP functional with different basis sets under the TDDFT formalism. . . . .	92
A8	Calculated excitation energies (eV) and oscillator strengths (a.u.) for NB using the M06 functional with different basis sets under the TDDFT formalism. . . . .	92
A9	Calculated excitation energies (eV) and oscillator strengths (a.u.) for NB cation using the B3LYP functional with different basis sets under the TDDFT formalism. . . . .	92
A10	Calculated excitation energies (eV) and oscillator strengths (a.u.) for NB cation using the M06 functional with different basis sets under the TDDFT formalism. . . . .	93
A11	Excitation energies (EE) and oscillator strengths ( $f$ ) for NB cation at the optimized neutral and cation geometries at the EOM-EE-CCSD/6-311+G* level of theory. . . . .	93
A12	Coefficients extracted from transients at 650 nm, $10^{12} \text{ W cm}^{-2}$ fitted to eq (1). . . . .	94
A13	Coefficients extracted from transients at 650 nm, $10^{13} \text{ W cm}^{-2}$ fitted to eq (1). . . . .	94
A14	Coefficients extracted from transients at 800 nm, $10^{12} \text{ W cm}^{-2}$ fitted to eq (1). . . . .	95
A15	Coefficients extracted from transients at 800 nm, $10^{13} \text{ W cm}^{-2}$ fitted to eq (1). . . . .	95
B1	Fit coefficients for 400 nm probe. . . . .	98
B2	Fit coefficients for 650 nm probe. . . . .	98
B3	Fit coefficients for 800 nm probe. . . . .	98
B4	Optimized geometric coordinates for neutral PNT . . . . .	99
B5	Optimized geometric coordinates for PNT cation . . . . .	99
B6	Harmonic vibrational frequencies and intensities for optimized PNT cation . . . . .	100
B7	Geometric coordinates for PNT cation with C–C–N–O dihedral angle of $87.4^\circ$ . . . . .	101
B8	Excitation energies (EE) and oscillator strengths ( $f$ ) for PNT cation at the neutral optimized geometry (C–C–N–O dihedral angle of $0.1^\circ$ ) at the B3LYP/Def2TZVPP and EOMEE-CCSD/6-311+G* levels of theory . . . . .	101

B9	Excitation energies (EE) and oscillator strengths ( $f$ ) for optimized PNT cation (C–C–N–O dihedral angle of $52.7^\circ$ ) at the B3LYP/Def2TZVPP and EOMEE- CCSD/6-311+G* levels of theory . . . . .	101
C1	Cartesian coordinates for neutral ONA optimized at the CAM-B3LYP/6-311+G* level. . . . .	102
C2	Cartesian coordinates for ONA cation optimized at the CAM-B3LYP/6-311+G* level. . . . .	103
C3	Excited state energies and oscillator strengths for neutral ONA. . . . .	103
C4	Excited state energies and oscillator strengths for ONA cation at the $S_0$ geometry. . . . .	104
C5	Excited state energies and oscillator strengths for ONA cation at the $D_0$ geometry. . . . .	104
C6	Coefficients extracted from curve fitting for direct dissociation pathways. . . . .	105
C7	Coefficients extracted from curve fitting for NNR and H transfer pathways. . . . .	105
C8	Cartesian coordinates for INT1c and INT2c optimized at the CAM-B3LYP/6-311+G* level. . . . .	106
C9	Cartesian coordinates for INT3c and INT4c optimized at the CAM-B3LYP/6-311+G* level. . . . .	106
C10	Cartesian coordinates for INT5c and INT6c optimized at the CAM-B3LYP/6-311+G* level. . . . .	107
C11	Cartesian coordinates for INT7c optimized at the CAM-B3LYP/6-311+G* level. . . . .	107
C12	Direct pathway energies (E) calculated at the CAM-B3LYP/6-311+G* level. Energies include ZPE. . . . .	108
C13	NNR pathway energies (E) calculated at the CAM-B3LYP/6-311+G* level. Energies include ZPE. . . . .	108
C14	H transfer pathway energies (E) calculated at the CAM-B3LYP/6-311+G* level. Energies include ZPE. . . . .	109
C15	Harmonic frequencies ( $\text{cm}^{-1}$ ) and intensities ( $\text{km mol}^{-1}$ ) for transition states within direct pathway, calculated at the CAM-B3LYP/6-311+G* level. . . . .	110

C16	Harmonic frequencies ( $\text{cm}^{-1}$ ) and intensities ( $\text{km mol}^{-1}$ ) for transition states within NNR pathway, calculated at the CAM-B3LYP/6-311+G* level. . . . .	111
C17	Harmonic frequencies ( $\text{cm}^{-1}$ ) and intensities ( $\text{km mol}^{-1}$ ) for transition states within H transfer pathway,calculated at the CAM-B3LYP/6-311+G* level (TS1c to TS4c). . . . .	112
C18	Harmonic frequencies ( $\text{cm}^{-1}$ ) and intensities ( $\text{km mol}^{-1}$ ) for transition states within H transfer pathway,calculated at the CAM-B3LYP/6-311+G* level (TS5c to TS8c). . . . .	113

# List of Abbreviations

<b>FTRMS</b>	femtosecond time-resolved mass spectrometry
<b>TDSE</b>	time-dependent Schrödinger equation
<b>FWHM</b>	full-width at half-maximum
<b>HF</b>	Hartree-Fock
<b>SD</b>	Slater determinant
<b>DFT</b>	density functional theory
<b>TDDFT</b>	time-dependent density functional theory
<b>EOM-CCSD</b>	equation-of-motion excitation-energies coupled cluster singles and doubles
<b>AIMD</b>	ab initio molecular dynamics
<b>BOMD</b>	Born–Oppenheimer molecular dynamics
<b>PES</b>	potential energy surface
<b>OPA</b>	optical parametric amplifier
<b>BBO</b>	$\beta$ -barium borate
<b>NB</b>	nitrobenzene
<b>PNT</b>	<i>p</i> -nitrotoluene
<b>ONA</b>	<i>o</i> -nitroaniline
<b>ONT</b>	<i>o</i> -nitrotoluene
<b>TATB</b>	2,4,6-triamino-1,3,5-trinitrobenzene
<b>TEMPO</b>	2,2,6,6-tetramethylpiperidine-N-oxyl
<b>TAS</b>	transient absorption spectroscopy

## Chapter 1

# Introduction

### 1.1 Motivation

This section is adapted from Refs. 3 and 4:

Tibbetts, K. M. Coherent Vibrational and Dissociation Dynamics of Polyatomic Radical Cations. *Chem. Eur. J.* **2019**, 25, 8431–8439.

Ampadu Boateng, D.; Gutsev, G. L.; Jena, P.; Tibbetts, K. M. Dissociation Dynamics of 3- and 4-Nitrotoluene Radical Cations: Coherently Driven C–NO<sub>2</sub> Bond Homolysis. *J. Chem. Phys.* **2018**, 148, 134305.

Polyatomic radical cations play a fundamental role in many physical, chemical, and biological processes. The reactions of aromatic radical cations and hydrogen atoms contribute to the formation of complex organic molecules observed in the interstellar medium.<sup>5</sup> The stability of electron-donor radical cations in organic photovoltaics influences the rate of charge separation and transport, and thereby the device efficiency.<sup>6</sup> Radical cations formed upon oxidation by photoexcited Ru(bpy) act as intermediates in catalytic photoredox reactions for organic synthesis applications.<sup>7</sup> In biological systems, ionizing radiation generates radical cations in the DNA sugar-phosphate backbone and nucleobases, which can ultimately lead to DNA damage and diseases such as cancer.<sup>8</sup> The formation of radical cations in biological antioxidants, such as carotenoids and flavonoids, both mitigates these damaging radiation effects and contributes to light-harvesting efficiency in photosynthesis.<sup>9</sup> Decomposition mechanisms in energetic materials used as explosives and propellants can be initiated by radical cations and anions.<sup>10</sup> It is particularly in this last area of research, that our lab has specialized.

Understanding the detonation mechanisms of energetic materials used in military<sup>11</sup> and

mining<sup>12</sup> operations has been an active area of research for decades. While extensive studies have unraveled mechanisms of stored energy released in bulk energetic materials,<sup>13–17</sup> initial dissociation mechanisms of isolated energetic molecules still constitute an active area of investigation.<sup>18–22</sup> In energetic materials, excited electronic states and molecular ions are thought to drive initial energy release processes based on the observation of tribological luminescence<sup>23,24</sup> Thus, understanding relaxation and dissociation processes from excited states and ions of isolated energetic molecules is needed to fully understand initial excitation events in energetic materials, which may facilitate longstanding goals such as developing photoactive high explosives that can be initiated by lasers.<sup>25</sup> In this context, the final aim of the lab is to study the dynamics and the initial dissociation mechanism of real explosives such as 2,4,6-trinitrotoluene (TNT) and 1,3,5-triamino-2,4,6-trinitrobenzene (TATB), to name a few, through an initial study of different model molecules. This work contains studies on three of these model molecules: nitrobenzene (NB), *p*-nitrotoluene (PNT), and *o*-nitroaniline (ONA).

## 1.2 Time-resolved spectroscopy and the pump-probe approach

In time-resolved spectroscopy we are specifically interested in studying fundamental systems at the atomic and molecular level, where the laws of quantum mechanics dictate the dynamics. In quantum mechanics, the complex wave function  $\Psi(\mathbf{r}, t)$  provides a complete description of the system; at any given time, knowledge of  $\Psi(\mathbf{r}, t)$  yields information about an object's dynamical variables such as position, momentum, or energy. These quantities are called observables, as one can measure (observe) their values in a given system. Time-resolved spectroscopy involves measuring observables for quantum systems whose wave functions are prepared in a well-defined initial state and subsequently evolve in time.

In order to investigate the dynamic behavior of an atomic or molecular system we need to perform a series of measurements of the system at different times. We will find it useful to think about a generic time-domain spectroscopy experiment as a “pump–probe” interrogation of the quantum system. An applied pump pulse prepares the system, originally in equilibrium, in some new state. In general, this state will be away from dynamic equilibrium (nonstationary), and so the system will evolve in time. Natural molecular timescales (picoseconds for rotations, femtoseconds for vibrations, and attoseconds for electronic dynamics) tend to be much shorter than the time resolution achievable with state-of-the-art

electronic detectors. Therefore, one needs to gate the dynamics initiated by the pump with a sufficiently fast probe pulse.<sup>26</sup> Optical time resolution, given by the light pulse duration, has long surpassed electronic time resolution by several orders of magnitude, and so time-resolved experiments typically gate the measurement using a probe pulse. The probe pulse interrogates the system, leading to the detection of a final product such as a charged particle or scattered photon. Since most experimental measurements are destructive (they modify the quantum state) and less than 100% efficient, they are carried out on ensembles of identically prepared molecules; a new measurement at each time delay between the pump and probe pulses is carried out on a new ensemble of molecules.

The whole suite of time-resolved spectroscopic techniques can be thought of as different implementations of this basic approach. The pump and probe can be laser pulses in the infrared, visible, ultraviolet, or X-ray regions of the spectrum, or accelerated charged particles such as electrons that originate from either inside or outside the quantum system. In the particular case of the experiments described in this work we make use of two femtosecond laser pulses, one in the near infrared and the other in the visible region. The effect of the probe beam is measured by the detection of molecular charged species by means of a time-of-flight mass spectrometric setup.

## Chapter 2

# A few concepts of dynamics in quantum systems

Some portions of this chapter have been adapted from Refs. 27 and 28:

Weinacht, T. *Time-resolved spectroscopy : an experimental perspective*; Textbook series in physical sciences; CRC Press, Taylor Francis Group: Boca Raton, 2019.

Ohmori, K. Wave-Packet and Coherent Control Dynamics. *Annual Review of Physical Chemistry* **2009**, 60, 487–511.

As discussed previously, our primary quantity of interest in time-domain spectroscopy is  $\Psi(\mathbf{r}, t)$ , the wave function describing the quantum system. For even the simplest example of the hydrogen atom,  $\Psi(\mathbf{r}, t)$  has six spatial degrees of freedom (three each for the proton and electron) as well as two spin degrees of freedom. One often begins by considering the full-wave function to be a product of spin and spatial portions, focusing on the spatial part initially while ignoring the spin. As the complexity of the system grows, the possible degrees of freedom that can be included in  $\Psi(\mathbf{r}, t)$  increases but for the following discussion we will focus on a one-dimensional spatial wave function.

By experimentally measuring  $\Psi(\mathbf{r}, t)$  at many different times, one can map out how the wave function evolves. However, one cannot directly measure the complete wave function, and much of the work in experimental time-domain spectroscopy is determining exactly what is being measured and how additional measurements might provide access to different aspects of  $\Psi(\mathbf{r}, t)$ . This is especially true for multidimensional systems, and the “art” of experimental science is often putting together as complete a picture as possible of the time-dependent wave function from the pieces that one captures in a collection of measurements.

The primary goal of this chapter is to develop an intuitive understanding of some aspects of field-free quantum dynamics in one dimension. We attempt to accomplish this by interpreting numerical solutions to the time-dependent Schrödinger equation (TDSE). Thus, we begin this chapter outlining an approach for solving the TDSE numerically using the split-operator<sup>29</sup> method since it is intuitive and physical to a good extent.

## 2.1 Split-operator approach

In our actual pump-probe experiment, we are interested in following the dynamics of the system after an ultrashort laser pump pulse prepares it in a particular state. The evolution of the system starts as soon as the electric field associated with the pump pulse is over and therefore, we are interested in the quantum dynamical description of the system without any applied field, and so we begin with the one-dimensional TDSE for a time-independent Hamiltonian:

$$i\frac{\partial\Psi(x,t)}{\partial t} = \hat{H}\Psi(x,t) \quad (2.1)$$

This equation is separable and has the following solution:

$$\Psi(x,t) = e^{-i\hat{H}t}\Psi(x,0) \quad (2.2)$$

where  $e^{-i\hat{H}t}$  is the time-evolution operator (or propagator) for the quantum state under the Hamiltonian  $\hat{H}$ . The time-evolution operator is often called  $U(t,0)$ , which carries an initial wave function at  $t = 0$  to a final wave function at time  $t$ :

$$\Psi(x,t) = U(t,0)\Psi(x,0) \quad (2.3)$$

If one knows the initial wave function and the Hamiltonian, it is possible to calculate the wave function at any other time. However, in most cases, applying the evolution operator for a finite time interval is a nontrivial task. This can be seen by noting that the Hamiltonian is a sum of kinetic and potential terms:

$$\hat{H} = \hat{T} + \hat{V} = \frac{\hat{p}^2}{2m} + V(x) \quad (2.4)$$

where  $\hat{p}$  is the momentum operator, which expressed in the position basis is  $\hat{p} = -i\hbar\partial/\partial x$ . The kinetic and potential operators do not generally commute and this implies that  $e^{-i\hat{H}t} \neq e^{-i\hat{T}t}e^{-i\hat{V}t}$ . While this factorization is not possible for finite times  $t$ , it would greatly aid in calculating the time evolution of  $\Psi$ . In particular, one could first implement the potential portion of the time-evolution operator in position space (acting on  $\Psi(x)$ ), Fourier transform the wave function to momentum space, and then implement the kinetic portion in momentum space (acting on  $\Psi(p)$ ). This avoids the complexity of operating with  $\hat{p}^2$  in position space, where it is a differential operator.

Since we can perform the calculations using a computer, a solution is to break up the propagator into a series of small intervals  $\Delta t$  (for  $N$  total intervals with  $N\Delta t = t$ ). Then we have (omitting the "hats" for simplicity):

$$e^{-iHt} = e^{-iH\Delta t}e^{-iH\Delta t} \dots e^{-iH\Delta t} \quad (2.5)$$

Now the implementation of the factorized time-evolution operator can be carried out for each small interval as described earlier, with an error that scales favorably with  $\Delta t$ . It is possible to find a  $\Delta t$  value for which the error is tolerable, while the time for the calculation is manageable. The recipe for implementing the propagator from  $t = 0$  to a final time  $t$  is

$$\Psi(x, t) = U(t, 0)\Psi(x, 0) = \prod_n U(n\Delta t, (n-1)\Delta t)\Psi(x, 0) = \prod_n e^{-iT\Delta t}e^{-iV\Delta t}\Psi(x, 0) \quad (2.6)$$

For each term in the product, we carry out the potential part of the propagator in position space, Fourier transform the wave function to momentum space, carry out the kinetic part of the propagator in momentum space, and finally Fourier transform back to position space. This four-step process amounts to

$$\Psi'(x, t + \Delta t) = e^{-iV\Delta t}\Psi(x, t) \quad (2.7)$$

$$\Psi'(p, t + \Delta t) = \frac{1}{\sqrt{2\pi}} \int_{-\infty}^{\infty} \Psi'(x, t + \Delta t) e^{-ipx} dx \quad (2.8)$$

$$\Psi''(p, t + \Delta t) = e^{-iT\Delta t}\Psi'(p, t + \Delta t) \quad (2.9)$$

$$\Psi''(x, t + \Delta t) = \frac{1}{\sqrt{2\pi}} \int_{-\infty}^{\infty} \Psi''(p, t + \Delta t) e^{+ixp} dp \quad (2.10)$$

where  $\Psi(x, t)$  is the wave function at the beginning of the interval and  $\Psi''(x, t + \Delta t)$  is the new wave function at time  $t + \Delta t$ . This sequence is repeated for each  $\Delta t$ , with  $\Psi''(x, t + \Delta t)$  serving as the new initial wave function for the next step.

### 2.1.1 Harmonic potential

Given the important role that vibrational dynamics play in time-resolved spectroscopy, we consider a diatomic molecule as our bound system. If one is primarily interested in the relative motion of the two atoms, the problem can be treated in one dimension by defining a reduced mass and using the internuclear separation as the relevant degree of freedom. As a simple example, two hydrogen atoms can form a bond, essentially sharing the two valence electrons between them. This bond establishes a minimum potential energy separation about which the two hydrogen nuclei reside. The motion of the nuclei in this potential is what gives rise to molecular vibrations. Near the minimum of the potential, the curve is nearly harmonic, and like all continuous functions near an equilibrium, it is well approximated by a parabola. We therefore continue our discussion considering the one-dimensional quantum harmonic oscillator with  $V(x)$  of the form:

$$V(x) = \frac{1}{2}m\omega^2x^2 \quad (2.11)$$

where  $m$  is the mass of the particle and  $\omega$  represents the classical angular frequency of oscillation. The time-independent, stationary-state solutions for this potential are calculated in most textbooks using either an algebraic approach with raising and lowering operators, or through a series solution to the differential equation. The primary result is that the eigenstates can be written in terms of the Hermite polynomials multiplying a Gaussian function and have evenly spaced energies:

$$E_n = \left(n + \frac{1}{2}\right)\hbar\omega \quad (2.12)$$

where  $n$  is the quantum number of the state.

We will employ the split-operator approach to describe how a wave function  $\Psi(x, t)$  evolves in the potential given by Eq. 2.11. Considering an initial Gaussian wave function of the form:

$$\Psi(x, t = 0) = Ae^{-a(x-x_0)^2} \quad (2.13)$$

where  $A$  is an amplitude determined by normalization,  $x_0$  is the center position, and  $a$  is related to the standard deviation of the wave function. Offsetting the Gaussian from the center of the well by twice its full-width at half-maximum (FWHM), the evolution of the wave function and the corresponding width and position are shown in Fig. 2.1. The upper-left panel plots the initial wave function, while the upper-right panel shows the wave function after four periods of oscillation. Note that both the central position and spread of the wave function have returned to their original values. The spread of the wave function is given by its standard deviation  $\sigma_x = \sqrt{\langle (x - \langle x \rangle)^2 \rangle}$ . The lower-left panel plots the wave function at the end of the simulation, when it is roughly in the middle of the well. At this location in its period, the wave function is at its widest. The lower-right panel plots the position and width of  $\Psi(x, t)$  as functions of time. The oscillation in  $\langle x \rangle$  is characteristic of any bound potential and the width of the wave function ( $\sigma_x$ ) also oscillates but at twice the frequency.

For this special case of the harmonic oscillator, the natural dispersion of the wave function in the TDSE is balanced by the parabolic shape of the potential. We will see later that this is no longer the case for real molecular systems but we expect that this discussion gives a solid intuition on the behaviour of vibrational dynamics.

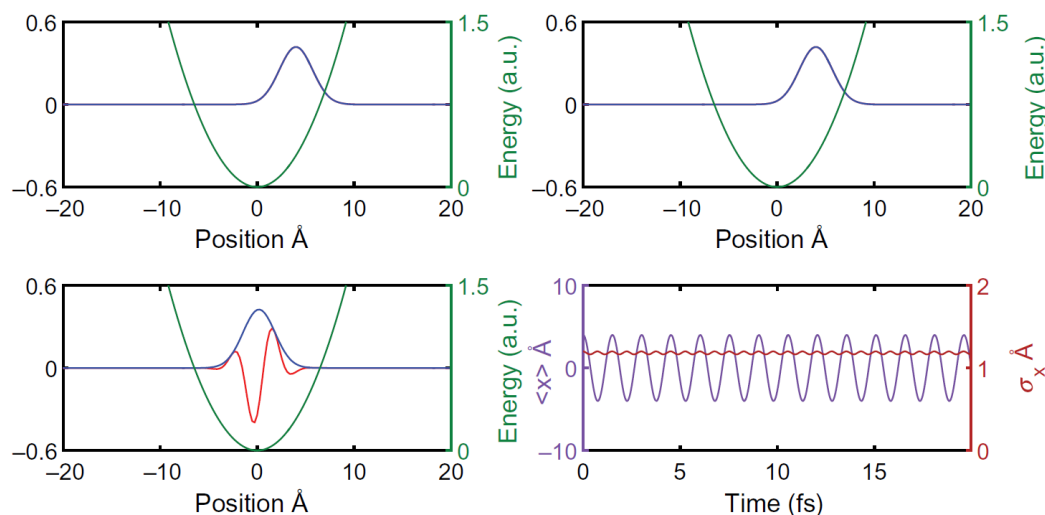


Figure 2.1: Evolution of a Gaussian function on a harmonic potential under the split-operator approach. First three panels: magnitude (blue) and real part (red) of  $\Psi(x, t)$  at three different times. Right axis depicts the potential (green). Bottom-right panel: position ( $\langle x \rangle$ ) and standard deviation ( $\sigma_x$ ) of the wave function versus time. Reproduced from Ref. [27](#) with permission from Taylor and Francis Group LLC.

## 2.2 Vibrational wave packet

The previous section discussed the dynamics of a Gaussian function under the influence of a harmonic potential. Here, we will elaborate on the connection of these concepts with the actual pump-probe experiments performed for this work. Molecular vibrations have time scales of around  $10^{-13}$  s and the development of femtosecond laser techniques makes it possible to follow the motions of molecular systems as they occur.<sup>[30](#)</sup> The requirement is that the system is excited on a timescale shorter than the vibrational period.<sup>[28,30](#)</sup> Figure [4.6](#) shows schematically a diatomic molecule irradiated with an ultrashort optical pulse. If the duration of the pulse is shorter than the classical vibrational period of the molecule, the bandwidth of the pulse is then broad enough to cover multiple vibrational eigenstates (with different transition frequencies represented schematically as  $\omega_0, \dots, \omega_5$ ). Those eigenstates are thus coherently superposed to give constructive or destructive interferences as functions of time and space to create a spatially localized wave function. This superposition of vibrational eigenstates is called a vibrational wave packet.

Since the vibrational eigenstates can be written in terms of Hermite polynomials multiplying a Gaussian function it sounds reasonable to assume that the coherent superposition of some of these vibrational eigenstates, the wave packet, has a Gaussian functional form.

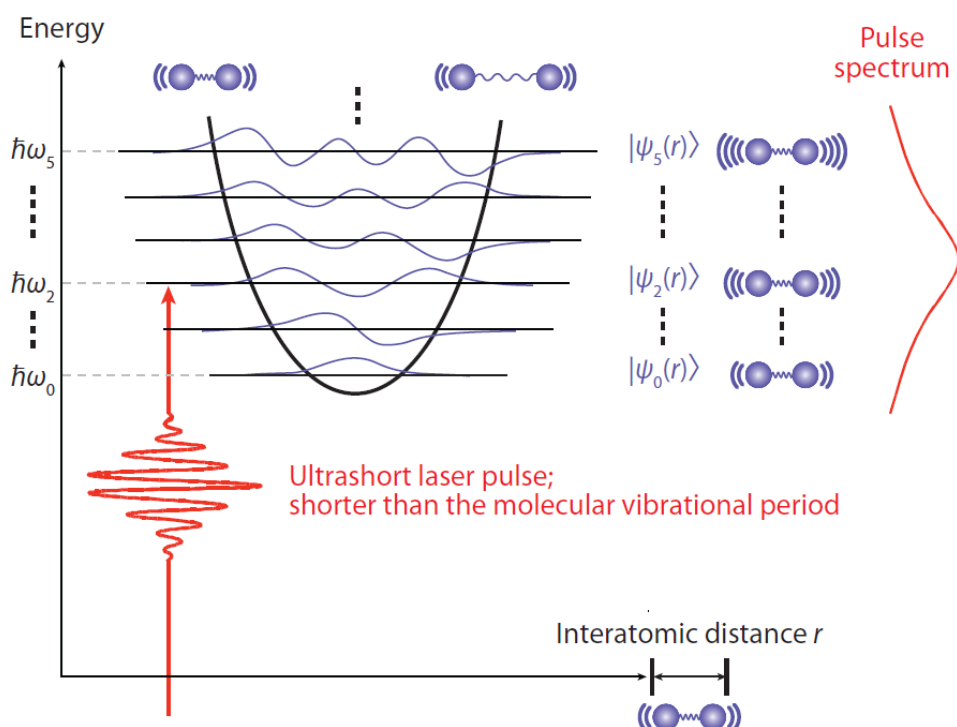


Figure 2.2: Schematic representation of the generation of a vibrational wave packet (WP) with an ultrashort laser pulse. Adapted from Ref. 28 with permission from Annual Reviews.

This is precisely the initial Gaussian function described by Eq. 2.13 which was considered as the starting point of the split-operator dynamic approach. The evolution of the wave packet can be considered as a field-free process because the pulse that prepares the wave packet is very short in comparison with the vibrational period. For example, the vibrational period of a diatomic iodine molecule is 131 fs while the typical duration of a pulse that can be generated in our current experiment is between 20 and 30 fs.

## Chapter 3

# Quantum chemistry methods

Some portions of this chapter have been adapted from Refs. 31 and 32:

Wu, X.; Su, P. In *Quantum Chemistry in the age of machine learning*; Dral, P. O., Ed.; Elsevier, 2022; p 3–25.

Jensen, F. *Introduction to computational chemistry*, 3rd ed.; John Wiley Sons: Chichester, UK, 2017.

Quantum chemistry (QC) refers to the application of quantum mechanics to study the chemical and physical properties of atoms, molecules, and materials. It is generally accepted that the first QC calculation was performed by the German physicists Walter Heitler and Fritz London on the hydrogen molecule in 1927. Now, QC has become an irreplaceable tool for chemists to explore fundamental scientific questions in chemistry and related fields. This chapter briefly introduces the QC methods employed in this work.

### 3.1 Born–Oppenheimer approximation

The solution of the Schrödinger equation for molecular systems is the primary task of QC. However, an exact solution cannot be obtained for multi-electron systems. The time-independent Hamiltonian in atomic units for a multi-electronic molecule is:

$$\hat{H} = - \sum_i^{N_{elec}} \frac{1}{2} \nabla_i^2 - \sum_a^{N_{nuclei}} \frac{1}{2} \nabla_a^2 - \sum_a^{N_{nuclei}} \sum_i^{N_{elec}} \frac{1}{|R_a - r_i|} + \sum_i^{N_{elec}} \sum_{j>i}^{N_{elec}} \frac{1}{|r_i - r_j|} + \sum_a^{N_{nuclei}} \sum_{b>a}^{N_{nuclei}} \frac{1}{|R_a - R_b|} \quad (3.1)$$

This Hamiltonian contains the electron kinetic operators (first term), nuclear kinetic operators (second term), nucleus-electron attractive potential operators (third term), electron–electron

repulsion (fourth term), and nucleus-nucleus repulsion (final term). The Born–Oppenheimer (BO) approximation is introduced in order to simplify the Hamiltonian. In the BO approximation, the coupling between the nuclear and the electronic wave function is neglected. In most cases, the coupling between two electronic states is not strong, i.e., the energy difference between two electronic states is big enough so that a small displacement of nuclei will not change the electronic state, making the BO approximation valid, which allows the separation of electrons (light particles) from nuclei (heavy particles) on time scales, resulting in a considerable simplification.

According to this approximation, the total Hamiltonian operator can be expressed as the sum of electronic Hamiltonian and nuclear Hamiltonian. The electronic Hamiltonian is written as:

$$\hat{H}_{el} = - \sum_i^{Nelec} \frac{1}{2} \nabla_i^2 - \sum_a^{Nnuclei} \sum_i^{Nelec} \frac{1}{|R_a - r_i|} + \sum_i^{Nelec} \sum_{j>i}^{Nelec} \frac{1}{|r_i - r_j|} \quad (3.2)$$

## 3.2 Slater determinants

According to the Pauli principle, the wave function of a multi-electron atom or molecule should be antisymmetric with respect to the exchange of two electrons. Antisymmetrization leads to Fermi holes, preventing the close approach of the electrons with the same spin and reducing the repulsion energy between them. Thus, the many-electron function can be approximately written as the antisymmetrized product of  $N$  one-electron functions in the form of a Slater determinant (SD):

$$\psi(r_1, r_2, \dots, r_N) = \frac{1}{\sqrt{N!}} \begin{vmatrix} \phi_1(r_1) & \phi_2(r_1) & \cdots & \phi_N(r_1) \\ \phi_1(r_2) & \phi_2(r_2) & \cdots & \phi_N(r_2) \\ \vdots & \vdots & \cdots & \vdots \\ \phi_1(r_N) & \phi_2(r_N) & \cdots & \phi_N(r_N) \end{vmatrix} \quad (3.3)$$

In equation 3.3  $\phi_1, \dots, \phi_N$  refer to spin orbitals. The solution of the Schrödinger equation involves calculations of all pairwise interactions between electrons and electrons and nuclei (see Eq. 3.2), which becomes analytically intractable for more than a two-body problem (one nucleus and one electron). This leads to the fact that the Schrödinger equation cannot be solved exactly for multi-electron systems.

### 3.3 Categories of electronic structure methods

Molecular electronic structure methods can be commonly divided into two categories, those based on wave function theory (WFT) and those derived from density functional theory (DFT). Within WFT, there are also two categories, valence bond (VB) method and molecular orbital (MO) methods. VB method was developed by W. Heitler, F. London, J. C. Slater and L. Pauling. One of the significant advantages of VB theory is its visually intuitive wave function. The physical basis of VB theory is that a chemical bond arises from the spin-exchange between two electrons. Thus, it aims to construct wave functions in which all possible bonding patterns are described in terms of spin coupling. As such, VB theory deals with multi-reference wave functions constructed directly from atomic orbitals (AOs), which are usually non-orthogonal for different atoms, whereas MO-based methods usually use orthogonal delocalized orbitals. The MO method was introduced in 1929 by Friedrich Hund and Robert S. Mulliken, which describes electrons by mathematical functions delocalized over an entire molecule. Since the 1960s, the MO method has become an irreplaceable tool for interpretation of molecular properties and chemical reactions.

### 3.4 Wave function theory methods

#### 3.4.1 Hartree–Fock method

The Hartree–Fock (HF) method seeks to approximately solve the electronic Schrödinger equation with the assumption that the wave function can be approximated by a single SD made up of one set of spin orbitals. The HF method is a wave function based approach based on an independent particle model, which reduces the many-electron problem to independent single-electron problems. It means that the interactions between the particles are approximated by taking all interactions into account in an average fashion.

The HF method is derived from the variational principle, which is applied to an energy functional that includes Lagrange multipliers for orthonormal constraints and defines the HF matrix for each orbital. First, by using the Condon–Slater rules, the energy of a single determinant can be expressed as:

$$E = - \sum_{i=1}^n h_{ii} + \frac{1}{2} \sum_{i=1}^n \sum_{j=1}^n (J_{ij} - K_{ij}) \quad (3.4)$$

where  $J_{ij}$  and  $K_{ij}$  are the Coulomb and exchange integral between spin orbitals  $i$  and  $j$ , respectively:

$$J_{ij} = \langle ij|ij \rangle = \int \int d\tau_1 d\tau_2 \phi_i^*(1) \phi_j^*(2) \frac{1}{r_{12}} \phi_i(1) \phi_j(2) \quad (3.5)$$

$$K_{ij} = \langle ij|ji \rangle = \int \int d\tau_1 d\tau_2 \phi_i^*(1) \phi_j^*(2) \frac{1}{r_{12}} \phi_j(1) \phi_i(2) \quad (3.6)$$

$h_{ii}$  is the one-electron integral

$$h_{ii} = \langle i|\hat{h}(1)|i \rangle = \int d\tau_1 \phi_i^*(1) \hat{h}(1) \phi_i(1) \quad (3.7)$$

where  $\hat{h}(1)$  is the one-electron operator including the electronic kinetic energy operator and the electron-nucleus potential operator shown in Eq. 3.2.

The objective now is to determine a set of MOs that makes the energy a minimum or at least stationary with respect to a change in the orbitals. The variation must be carried out to ensure that MOs remain orthogonal and normalized. Since  $E$  varies subjected to a constraint that the spin orbitals are orthonormal,

$$\langle i|j \rangle - \delta_{ij} = 0 \quad (3.8)$$

where  $\langle i|j \rangle$  is the Dirac notation of the inner product of two spin orbitals,

$$\langle i|j \rangle = \int d\tau \phi_i^* \phi_j \quad (3.9)$$

and  $\delta_{ij}$  is the Kronecker delta,

$$\delta_{ij} = \begin{cases} 1, & \text{if } i = j, \\ 0, & \text{if } i \neq j. \end{cases} \quad (3.10)$$

A constrained optimization by using Lagrange multipliers can be expressed as:

$$\delta \left( E - \sum_{ij} \varepsilon_{ij} (\langle i|j \rangle - \delta_{ij}) \right) = 0 \quad (3.11)$$

$$\sum_i \delta h_{ii} + \frac{1}{2} \sum_i \sum_j (\delta J_{ij} - \delta K_{ij}) - \sum_i \sum_j \varepsilon_{ij} \delta \langle i|j \rangle = 0 \quad (3.12)$$

where  $\varepsilon_{ij}$  refers to the Lagrange multiplier matrix elements, and the notation  $\delta$  indicates the variation of the functional. This leads to the following equation for a particular electron labeled as 1:

$$\sum_i \int \delta \phi_i^*(1) \left[ \hat{h}(1) \phi_i(1) + \sum_j (\hat{J}_j(1) - \hat{K}_j(1)) \phi_i(1) - \sum_j \varepsilon_{ij} \phi_j(1) \right] d\tau_1 + c.c. = 0 \quad (3.13)$$

In Eq. 3.13, c.c. is the complex conjugate of the summation ahead.  $\delta \phi_i$  indicates the variation of the spin orbital  $\phi_i$  ( $\phi_i \rightarrow \phi_i + \delta \phi_i$ ).  $\hat{J}(1)$  and  $\hat{K}(1)$  operators are related with the interaction of electron 1 with all the other electrons in the system and we can define them in the following way:

$$\hat{J}(1) = \sum_j \hat{J}_j(1) \quad \hat{K}(1) = \sum_j \hat{K}_j(1) \quad (3.14)$$

Considering this, Eq. 3.13 leads to the expression:

$$(\hat{h}(1) + \hat{J}(1) - \hat{K}(1)) \phi_i(1) = \sum_{ij} \varepsilon_{ij} \phi_j(1) \quad (3.15)$$

The terms within the parentheses define the so-called Fock operator, which is an effective one-electron energy operator. It describes the kinetic energy of an electron, the attraction to all the nuclei, and the interaction to all the other electrons. Eq. 3.15 may be simplified by choosing a unitary transformation that makes the matrix of Lagrange multipliers diagonal. This particular set of MOs is called canonical MOs and thus transforms Eq. 3.15 into a set of pseudo-eigenvalue equations:

$$\hat{F}(1) \phi_i(1) = \varepsilon_i \phi_i(1) \quad (3.16)$$

where  $\varepsilon_i$  is the orbital energy of the Hartree–Fock orbital.

$$\varepsilon_i = \langle i | \hat{h}(1) | i \rangle + \sum_j [\langle ij | ij \rangle - \langle ij | ji \rangle] \quad (3.17)$$

The HF equations form a set of pseudo-eigenvalue equations as the Fock operator depends on all the occupied MOs (via the Coulomb and exchange operators). A specific Fock operator can only be determined if all the other occupied orbitals are known and therefore the self-consistent field (SCF) procedure must be employed to solve the problem.

Rewriting the energy of a single SD showed in Eq. 3.4 using some of the definitions in this section and considering the nuclear-nuclear repulsion energy ( $V_{NN}$ ), the total HF energy of a molecule is expressed as:

$$E_{HF} = \sum_i^n \langle i | \hat{h}(1) | i \rangle + \frac{1}{2} \sum_i \sum_j [\langle ij | ij \rangle - \langle ij | ji \rangle] + V_{NN} \quad (3.18)$$

Comparing Eqs. 3.17 and 3.18 (and leaving aside the nuclear-nuclear repulsion term) it is clear that the total energy is not simply a sum of MO energies.

An electron at  $\mathbf{r}$  is viewed as interacting with an “averaged charge density” or “mean-field”, arising from the  $N - 1$  remaining electrons. Originally, the HF calculations were performed using numerical methods to solve the differential equations but this turned out to be complex. To overcome this difficulty, Roothaan proposed a procedure which expresses MOs as linear combinations of a set of known functions, called basis functions, leading to the so-called Hartree–Fock–Roothaan method. By using the expansion of basis functions for MOs,

$$\phi_i = \sum_{s=1}^b c_{si} \chi_s \quad (3.19)$$

where  $\{\phi_i\}$  are MOs,  $\{\chi_s\}$  are basis functions, and  $\{c_{si}\}$  are the expansion coefficients be determined. By this expansion, the variation of the orbitals can be represented by the variation of the expansion coefficients. Considering this, the total HF energy can be expressed as:

$$E_{HF} = \sum_{pq}^b D_{pq} h_{pq} + \frac{1}{2} \sum_{pqrs}^b D_{pq} D_{rs} [\langle pr | qs \rangle - \langle pr | sq \rangle] + V_{NN} \quad (3.20)$$

where  $b$  is the number of basis functions and  $D_{pq}$  is the density matrix element:

$$D_{pq} = \sum_i^n c_{pi} c_{qi} \quad (3.21)$$

The Roothaan expansion procedure allows one to find the HF wave function using matrix algebra. The solution of the Hartree–Fock–Roothaan method depends on the orbitals. Hence, we need to guess some initial orbitals and then refine our guesses iteratively. As such, Hartree–Fock–Roothaan method is a self-consistent field (SCF) method. In the SCF procedure, the calculation has converged if all corresponding matrix elements differ by negligible amounts from those in the previous step. One then uses the converged SCF wave function to calculate molecular properties.

Notice that the HF formalism mentioned above is the generalized form based on spin orbitals. Spin orbitals are the products of a spatial orbital and a spin function. Considering the occupation of electrons with  $\alpha$  or  $\beta$  spin on a spatial orbital, there are three kinds of HF methods. For multi-electron closed-shell systems without unpaired electrons, we can pair two electrons, one with  $\alpha$  and one with  $\beta$  spin, in one spatial orbital and get restricted Hartree–Fock (RHF). If this restriction is removed by letting different spins be located at different spatial orbitals, we obtain unrestricted Hartree–Fock (UHF). If the restriction of doubly occupied MOs is kept for open-shell systems, we have the restricted open-shell Hartree–Fock (ROHF) method. ROHF and UHF can be employed for systems with more than one unpaired electron (open-shell system).

### 3.4.2 Coupled-cluster method

The coupled-cluster (CC) method is based on the HF wave function. The method employs a total excitation operator  $\hat{T}$  that is defined as:

$$\hat{T} = \hat{T}_1 + \hat{T}_2 + \dots + \hat{T}_n \quad (3.22)$$

where  $n$  represents the number of electrons being promoted or excited from occupied to virtual orbitals (therefore the name of total excitation operator for  $\hat{T}$ ).

The CC wave function is obtained through the action of the operator  $e^{\hat{T}}$  on the HF wave function  $\psi_0$ :

$$|\psi_{CC}\rangle = e^{\hat{T}}|\psi_0\rangle \quad (3.23)$$

The exponent of an operator can be expressed in terms of a Taylor series expansion

$$e^{\hat{T}} = 1 + \hat{T} + \frac{\hat{T}^2}{2!} + \frac{\hat{T}^3}{3!} + \dots = \sum_{n=0} \frac{\hat{T}^n}{n!} \quad (3.24)$$

The operators  $\hat{T}_1$  and  $\hat{T}_2$  for the excitation of one and two electrons respectively are defined as

$$\hat{T}_1 = \sum_{i,a} t_i^a \hat{T}_i^a \quad \hat{T}_i^a |\psi_0\rangle = |\psi_i^a\rangle \quad (3.25)$$

$$\hat{T}_2 = \sum_{i<j,a<b} t_{ij}^{ab} \hat{T}_{ij}^{ab} \quad \hat{T}_{ij}^{ab} |\psi_0\rangle = |\psi_{ij}^{ab}\rangle \quad (3.26)$$

All the excitation operators  $\hat{T}^n$  will affect the HF ground state, any truncation in the CC method only refers to the excitation operators, the Taylor-series expansion will not be truncated.

The goal of the CC method is to find the coefficients  $t_i^a, t_{ij}^{ab}, \dots$ . The Schrödinger equation in the CC method is

$$\hat{H} e^{\hat{T}} |\psi_0\rangle = E_{CC} e^{\hat{T}} |\psi_0\rangle \quad (3.27)$$

Multiplying by  $\langle\psi_0|$  on the left gives

$$\langle\psi_0|\hat{H}|e^{\hat{T}}\psi_0\rangle = E_{CC}\langle\psi_0|e^{\hat{T}}\psi_0\rangle \quad (3.28)$$

Since  $e^{\hat{T}}|\psi_0\rangle = (1 + \hat{T} + \frac{1}{2}\hat{T}^2 + \dots)|\psi_0\rangle = |\psi_0\rangle + \hat{T}|\psi_0\rangle + \frac{1}{2}\hat{T}^2|\psi_0\rangle + \dots$ , all terms except the first one contain only determinants with at least one spin orbital different from  $|\psi_0\rangle$ . Consequently, the CC ground-state energy can be expressed as:

$$E_{CC} = \langle\psi_0|\hat{H}|e^{\hat{T}}\psi_0\rangle \quad (3.29)$$

So far, there is no truncation of the excitation operator. In practice, one uses a truncated excitation operator to approximate the actual one. If  $\hat{T}_1$  and  $\hat{T}_2$  are included the method is called coupled-cluster singles and doubles (CCSD).

### 3.5 Density functional theory methods

Density functional theory (DFT) claims that the energy of the ground state of a system of interacting particles within an external potential is a functional of the density of the particles and that density is univocally determined by the external potential.<sup>33</sup> For molecular systems, the previously mentioned particles are electrons and the external potential is that induced by atomic nuclei.

It is also demonstrated that the global minimum of the energy functional is the exact energy of the ground state of the system. This energy is determined by a particular electronic density, the ground state density.<sup>33</sup> Once this electronic density is known a complete description of the system is achieved.

The original formulation of DFT deals with a system of interacting particles but this leads to a difficult problem. To surpass this difficulty, Kohn and Sham<sup>34</sup> replaced the original system of interacting particles with one of independent particles incorporating the real system effects in an additional term. Finding the electronic density within the Kohn-Sham approach is equivalent to a self-consistent eigenvalue problem whose solution lies in solving an independent particle equation for each electronic state  $j$ :

$$\left( -\frac{1}{2}\nabla^2 + v_{\text{ext}}(r) + \int \frac{\rho(r')}{|r-r'|} dr' + v_{\text{XC}}[\rho] \right) \psi_j(r) = \varepsilon_j(r) \psi_j(r) \quad (3.30)$$

This equation is expressed in atomic units and the set  $\{\psi_j\}$  is known as the set of Kohn-Sham orbitals. The first term within the parenthesis is related with the electronic kinetic energy, the second contains information about the external potential created by the atomic nuclei, the third comes from the Coulombic repulsion between the electrons ( $\rho(r')$  is the electronic density at position  $r'$ ), and the last of the terms is the so-called exchange and correlation potential, related with the correction to energy for treating the electronic states using separate equations as if the electrons were independent particles.

The expression for the exchange and correlation potential is not known exactly, however, many approximations for it have been proposed. The first approximation, proposed by Kohn and Sham,<sup>34</sup> is based on the idea that the exchange and correlation energy for a system of interacting particles can be approximated by that of an electron gas with uniform density at each point of space, assuming in this way that the exchange and correlation potential depends only of local density factors:

$$E_{XC}[\rho] = \int \rho(r) \varepsilon_{XC}^{hom}(\rho(r)) dr \quad (3.31)$$

where  $\varepsilon_{XC}^{hom}(\rho(r))$  is the exchange and correlation energy of a homogeneous gas that has the same density as the one for the real system at point  $r$ . Additionally:

$$v_{XC} = \frac{\delta E_{XC}}{\delta \rho(r)} \quad (3.32)$$

The potential  $v_{XC}$  can be divided in its exchange and correlation contributions. The exchange part is known exactly for an electron gas thanks to the Thomas-Fermi-Dirac model<sup>35</sup> while the correlation part has only been approximated. This way of writing the exchange and correlation potential receives the name of local density approximation (LDA). This can be extended to the local spin density approximation (LSDA) for those cases where the  $\alpha$  and  $\beta$  densities are not equal. Perdew<sup>36</sup> has described a hierarchy of approximate treatments of the exchange-correlation term as “Jacob’s Ladder”. The ladder is grounded in Hartree-Fock (HF) theory here on earth, and reaches to heaven, where the exact functional is found. Along the way are five rungs, each defining a set of assumptions made in creating an exchange-correlation expression.

The next approximation to the exchange and correlation part comes from taking the LDA as the first term of a Taylor expansion in the density and considering higher order terms. In this way, the exchange and correlation energy can be written in a more general form as:

$$E_{XC}[\rho] = \int \rho(r) \varepsilon_{XC}^{hom}(\rho) F_{XC}[\rho(r), \nabla \rho(r), \nabla^2 \rho(r), \dots] dr \quad (3.33)$$

where  $F_{XC}$  is a factor that modifies the LDA expression according to the density variation in the neighbourhood of the point being considered. This way of expressing the exchange and correlation energy is called gradient expansion approximation (GEA).<sup>37</sup> Particularly, the expansion up to the first order is known as generalized gradient approximation (GGA)<sup>38</sup> and is the second rung on Jacob’s Ladder. The third rung, containing the so-called meta-GGA functionals, includes a dependence on the Laplacian of the density ( $\nabla^2 \rho$ ) or on the kinetic energy density. The fourth row, the hyper-GGA or hybrid functionals, includes a dependence on exact HF exchange. Finally, the fifth row incorporates the unoccupied Kohn-Sham orbitals. This is most widely accomplished within the so-called double hybrid functionals.

### 3.5.1 Functionals

Here we will briefly discuss the concepts behind the functionals used in this work. The method is denoted with an acronym that defines the exchange functional and the correlation functional in that order. For the exchange component, the most widely used is one proposed by Becke.<sup>39</sup> It introduces a correction term to LSDA that involves the density derivative (a GGA functional). The letter “B” signifies its use as the exchange term. Of the many correlation functionals, the two most widely used are due to Lee, Yang, and Parr<sup>40</sup> (referred to as LYP) and by Perdew and Wang<sup>41</sup> (referred to as PW91). While the PW91 functional depends on the derivative of the density (a GGA functional), the LYP functional depends on  $\nabla^2\rho$  (a meta-GGA functional). So the BPW91 designation indicates the use of the Becke exchange functional with the Perdew–Wang 91 correlation functional. Therefore, as a whole, the BPW91 is a GGA functional for the reasons previously discussed.

The hybrid methods combine the exchange–correlation functionals with some admixture of the HF exchange term and are among the most widely used functionals. The dominant DFT method for the last decades is the hybrid B3LYP functional,<sup>42,43</sup> which includes Becke’s exchange functional along with the LYP correlation functional:

$$E_{XC}^{B3LYP} = (1 - a)E_X^{LSDA} + aE_X^{HF} + bE_X^B + (1 - c)E_C^{LSDA} + cE_C^{LYP} \quad (3.34)$$

The three variables (a, b, and c) are the origin of the “3” in the acronym. Since these variables are fit to reproduce experimental data, B3LYP (and all other hybrid methods) contains some degree of “semiempirical” nature.

DFT methods sometimes are found to display systematic errors for certain properties and, once identified, efforts are made to fix these errors. One such identified error was in the calculation of excitation energies for charge transfer and to some extent also Rydberg states by time-dependent DFT (TDDFT) methods, where excitation energies often were underestimated by a factor of two. This is related to the general problem of most DFT methods to overdelocalize the electron density, that is delocalized systems are predicted to be artificially lower in energy than localized systems.<sup>32</sup> The full discussion on the origins of this errors are beyond the scope of this work but the fix that has been proposed is to partition the electron–electron Coulomb operator for the exchange energy (only) into a short- and a long-range

part, usually done by the standard error function as shown below, since this facilitates the calculation of the resulting integrals, where the  $\omega$  parameter controls the partitioning between the two parts:<sup>44</sup>

$$\frac{1}{|r_1 - r_2|} = \frac{1}{r_{12}} = \frac{1 - \text{erf}(\omega r_{12})}{r_{12}} + \frac{\text{erf}(\omega r_{12})}{r_{12}} \quad (3.35)$$

$$\text{erf}(x) = \frac{2}{\sqrt{\pi}} \int_0^x e^{-t^2} dt$$

The trick is to use different exchange functionals for the short- and long-range parts. The most common is to employ a density exchange functional for the short-range part and the (exact) HF expression for the long-range part. If the density exchange part by itself contains a fraction of HF exchange, the interpolation is between that fraction and 100%, rather than between 0 and 100%. The long-range HF exchange ensures that the DFT overdelocalization of charge separation is removed and yields much improved excitation energies for charge-transfer states. This kind of functionals are called *range-separated* or *long-range corrected* functionals. The  $\omega$  parameter in equation 3.35 determines when to switch between the short- and long-range parts. One of the first functionals to employ this idea was the CAM-B3LYP,<sup>45</sup> which builds upon the B3LYP method. The  $\omega$ B97X is similarly a range-separated version of the B97 functional containing a moderate (17) number of empirical parameters.<sup>46</sup> Determining the optimal  $\omega$  parameter can be done, for example, by fitting to experimental thermodynamic data, and a typical  $\omega$  value is 0.30–0.50 bohr<sup>-1</sup>.

One of the serious shortcomings of standard DFT methods is the inability to describe dispersion forces (part of van der Waals-type interactions).<sup>47</sup> Although dispersion is a short-ranged weak interaction, it is cumulative, and therefore becomes increasingly important as the system gets larger. Stefan Grimme has proposed to include dispersion by additive empirical terms, much like the van der Waals energy term in force field methods.<sup>48</sup> The parameterization in the earliest models simply included an  $R^{-6}$  energy term for each atom pair, with an atom dependent  $C_6$  parameter. The method has been refined by including higher-order terms ( $R^{-8}$ ,  $R^{-10}$ ) to better describe the medium-range dispersion and making the parameters depend on the atomic environment in terms of the number of directly bonded atoms. Adding such attractive energy terms has the potential problem of divergence for short interatomic distances and is consequently often used in connection with a damping function:

$$\Delta E_{disp} = - \sum_{n=6(8,10)} s_n \sum_{AB}^{atoms} \frac{C_n^{AB}}{R_{AB}^n} f_{damp}(R_{AB}) \quad (3.36)$$

A complication is that the parameterization of the dispersion correction depends on the underlying exchange-correlation functional, as different functionals via their parameterization may include some of the short-range interaction, and this can be taken into account by a functional-dependent scaling factor  $s_n$  in Equation 3.36. Such dispersion corrected methods are denoted with a D/D2/D3 after the DFT acronym, as, for example,  $\omega$ B97XD.

### 3.6 Basis sets

A basis set is a collection of basis functions that spans a space in which a problem is solved.<sup>32</sup> We would like to span the infinite space with flexible functions adapting to local chemical environment, but this would necessitate the use of the infinitely large *complete basis set* (CBS), which is obviously impossible in practice. Thus, any basis set is finite, which inevitably introduces an error compared to the CBS limit which in some cases can be estimated. The actual form of the basis functions varies strongly depending on the approach taken and common types of basis functions include Slater, Gaussian, polynomial, wavelets, and plane waves. While basis functions can be evaluated on a grid in space, we often prefer to use chemically intuitive and physically meaningful atom-centered basis functions (atomic orbitals, AOs), which are combined into MOs giving rise to the linear combination of atomic orbitals (LCAO)-MO approach. AOs can be represented by products of the radial and angular momentum parts, with the radial part defining the distance-behavior (e.g., having terms  $\exp(-\zeta \mathbf{r})$  in the Slater-type orbitals or  $\exp(-\alpha \mathbf{r}^2)$  in the Gaussian-type orbitals, where  $\zeta$  and  $\alpha$  are exponents and  $\mathbf{r}$  is the distance to the nucleus ensuring that the functions go toward zero for large distances), while the angular momentum part defines the shape of the orbital. Thus, AOs are conveniently described in notations common to chemists such as 1s, 2p<sub>x</sub>, or 3d<sub>xy</sub>.

The Gaussian-type orbitals are among the most popular because they allow for fast evaluation of integrals, leading to many Gaussian-type basis sets such as STO-3G, 6-31G, 6-311G, and aug-cc-pV6Z in the order of increasing size. Basis set STO-3G is a minimum (or single- $\zeta$ ) basis set for a minimum description of the orbitals of a neutral atom, which uses three

so-called primitive Gaussian orbitals fitted to a Slater-type orbital (hence STO). 6-31G and 6-311G belong to the Gaussian-type split-valence basis sets of double- and triple- $\zeta$  type respectively. Split-valence double- $\zeta$  means that each valence orbital is split into two parts with one part represented by three Gaussians and another by one Gaussian (hence “31”); the core orbitals are not split and are represented by six Gaussians (hence “6”). Aug-cc-pV6Z is one of the most timeconsuming yet very accurate basis sets. Here, cc-pV6Z stands for correlation-consistent, polarized valence 6- $\zeta$ , and aug stands for augmenting with diffuse primitive basis functions (particularly important for anions).

## 3.7 Excited state methods

### 3.7.1 Time-dependent density functional theory

Density functional theory can, in analogy to wave function methods, be extended to include time-dependent (external) electric potentials,<sup>49</sup> and this allows a description of, for example, excited states and frequency-dependent polarizability. The Hohenberg–Kohn theorem only holds for electron densities describing the time-independent ground state, but the Runge–Gross theorem<sup>50</sup> states that the unique one-to-one correspondence between an external potential and the electron density holds both in time-dependent and time-independent cases.

However, the full time-dependent treatment of DFT is not normally used since the most common applications fall in the regime of weak perturbations, where only the linear response is considered. Therefore, the response of the system is calculated by perturbation theory. The perturbation is usually an oscillating electric field, which in the dipole approximation can be written as

$$V_{ext}(t) = \mu F \cos(\omega t) \quad (3.37)$$

where  $\omega$  is the frequency,  $F$  is the strength of the field, and  $\mu$  is the dipole operator. The weak perturbation regime corresponds to the situation where the external electric field is significantly smaller than the field generated by the nuclear charge. For an electron in a hydrogen atom at a distance of 1 bohr, the nuclear field is  $\sim 5 \times 10^9$  V/m, which corresponds to a laser intensity of  $\sim 4 \times 10^{16}$  W/cm<sup>2</sup>.

Under this perturbational treatment, we have the **A** and **B** matrix elements given by:

$$A_{ij}^{ab} = \delta_{ij}\delta_{ab}(\varepsilon_a - \varepsilon_i) + \langle ij|ab \rangle + \langle ij|f_{xc}|ab \rangle \quad (3.38)$$

$$B_{ij}^{ab} = \langle ij|ab \rangle + \langle ij|f_{xc}|ab \rangle \quad (3.39)$$

with *ij* and *ab* denoting occupied and virtual orbitals as the common practice. We can see that the first term in the **A** matrix element corresponds to the difference in orbital energies between an occupied and virtual orbital. Then we have an exchange-type two-electron term in the second and first terms of **A** and **B** matrix elements respectively. Finally, the last term in both cases is related to exchange-correlation (XC) interaction with  $f_{xc}$  being called the XC kernel. It is the functional derivative of the corresponding potential:

$$f_{xc}(\mathbf{r}, t, \mathbf{r}', t') = \frac{\delta V_{xc}[\rho](\mathbf{r}, t)}{\delta \rho(\mathbf{r}', t')} \quad (3.40)$$

With the (**Y**, **Z**) vector representing the real and imaginary parts of the first-order response of the density to a time-dependent weak perturbation, the following result is obtained (with \* denoting complex conjugation):

$$\begin{pmatrix} \mathbf{A} & \mathbf{B} \\ \mathbf{B}^* & \mathbf{A}^* \end{pmatrix} \begin{pmatrix} \mathbf{Y} \\ \mathbf{Z} \end{pmatrix} = \omega \begin{pmatrix} 1 & 0 \\ 0 & -1 \end{pmatrix} \begin{pmatrix} \mathbf{Y} \\ \mathbf{Z} \end{pmatrix} \quad (3.41)$$

### 3.7.2 Equation-of-motion coupled-cluster singles and doubles

Equation-of-motion (EOM) CCSD is a method for excited states based on the coupled-cluster singles and doubles approach. In the EOM formalism, target states  $\psi$  are described as excitations from a reference state  $\psi_0$ :  $\psi = R\psi_0$ , where  $R$  is a general excitation operator. Different EOM models are defined by choosing the reference state and the form of the operator  $R$ .

In the EOM models for electronically excited states (EOM-EE), the reference is the closed-shell ground state Hartree-Fock determinant, and the operator  $R$  conserves the number of  $\alpha$  and  $\beta$  electrons. The reference states for EOM-IP/EA are determinants for  $N+1/N-1$  electron states, and the excitation operator  $R$  is ionizing or electron-attaching, respectively.

## Chapter 4

# Predicting the best probe for nitroaromatic cations

This chapter is an adapted version of the work in Ref. 51:

López Peña, H. A.; Ampadu Boateng, D.; McPherson, S. L.; Tibbetts, K. M. Using Computational Chemistry to Design Pump–Probe Schemes for Measuring Nitrobenzene Radical Cation Dynamics. *Physical Chemistry Chemical Physics* **2021**, 23 (23), 13338–13348.

### 4.1 Introduction

Polyatomic radical cations are highly reactive species that contribute to many physical, chemical, and biological processes. For instance, radical cations and anions participate in shock initiation of detonated energetic materials used as explosives and propellants;<sup>52</sup> generation of radical cations in DNA nucleobases and the sugar-phosphate backbone upon exposure to ionizing radiation induces DNA damage;<sup>8</sup> and radical cations of polycyclic aromatic hydrocarbons (PAHs) undergo numerous reactions that form other complex molecules in the interstellar medium.<sup>53</sup>

Intense femtosecond laser excitation coupled to mass spectrometry has been used for decades to study dissociation in radical cations because the short pulse duration induces rapid ionization prior to dissociative electronic excited state population, resulting in less molecular fragmentation.<sup>54</sup> In particular, excitation with near-infrared wavelengths ( $\sim 1200$ – $1600$  nm) is widely observed to suppress fragmentation compared to excitation with the 800 nm Ti:Sapphire wavelength.<sup>55–61</sup> The high yield of intact molecular ion is attributed to increased

contribution of adiabatic electron tunneling to the ionization process, thereby enhancing population of the ground electronic state of the cation.<sup>56,59</sup> However, extensive molecular fragmentation is still observed when the laser wavelength is resonant with an electronic transition between the ground electronic state and an excited state of the cation.<sup>57–65</sup>

Time-resolved pump-probe measurements are widely used to gain insight into how population of electronic excited states in radical cations induces dissociation.<sup>3,4,66–83</sup> Many of these experiments have identified time-dependent oscillations in transient ion yields due to the preparation of a coherent superposition of vibrational states, i.e., a vibrational wave packet, by the pump pulse and its subsequent excitation by the time-delayed probe pulse.<sup>3,4,66–78</sup> Complementary theoretical calculations of the participating electronic potential energy surfaces have uncovered mechanisms of dissociation via wave packet excitation. For instance, wave packet dynamics along the I–C–Br bending coordinate in  $\text{CH}_2\text{IBr}^+$  create a dynamic resonance between the  $D_0$  and  $D_3$  electronic states that results in loss of neutral iodine to form  $\text{CH}_2\text{Br}^+$ .<sup>67,68</sup> In acetophenone cation, wave packet dynamics along the torsional  $\text{CH}_3\text{CO}-\text{C}_6\text{H}_5$  twisting coordinate result in excitation from  $D_0$  to  $D_2$  at a dihedral angle of  $90^\circ$ , leading to loss of  $\text{CH}_3$  to form  $\text{C}_6\text{H}_5\text{CO}^+$ .<sup>71,72</sup>

The known importance of electronic resonances to dissociation of radical cations has motivated the use of resonant probe wavelengths in time-resolved measurements,<sup>77–83</sup> as is common practice in time-resolved studies of dynamics on neutral electronic excited states.<sup>84–89</sup> Nevertheless, many time-resolved measurements on radical cations use the readily available 800 nm wavelength for probing cation dynamics.<sup>3,4,66–75</sup> It would stand to reason that selecting the excitation wavelength to be resonant with electronic transitions in radical cations would enhance the amplitudes of the coherent oscillations resulting from vibrational wave packet dynamics. Computations of electronic potential energy surfaces can efficiently predict geometry-dependent electronic transitions in radical cations,<sup>67,68,71,72</sup> making computational chemistry a potentially powerful tool for designing pump-probe control schemes to measure coherent vibrational dynamics.

In this work, we use time-dependent density functional theory (TDDFT) calculations of the electronic potential energy surfaces of the nitrobenzene (NB) cation to predict the most efficient excitation wavelength and verify this prediction with time-resolved mass spectrometric measurements. As a common model for nitroaromatic explosives such as TNT,<sup>90,91</sup>

NB has been subject to mass spectrometry studies using strong-field femtosecond laser excitation,<sup>90–93</sup> although no time-resolved studies on NB have been reported to the best of our knowledge. We found that the  $D_0 \rightarrow D_4$  transition in nitrobenzene cation has strong coupling at a C–NO<sub>2</sub> dihedral angle of 90° with a  $\sim 2$  eV energy gap, making the transition nearly resonant with 650 nm excitation. Efficient geometry-dependent excitation at 650 nm is confirmed in pump-probe measurements, where oscillations in ion yields were enhanced by a factor of  $\sim 2$ –5 as compared to excitation at 800 nm. Similar enhancement of oscillation amplitudes with 650 nm excitation is also observed in the cations of the related molecules 2-NT and 4-NT. These results suggest that using computational chemistry to determine the best probe wavelength for time-resolved experiments can enhance the measurement of prepared vibrational coherent states, which is advantageous for coherent control and quantum information applications.

## 4.2 Methods

### 4.2.1 Theory

Our density functional theory (DFT) calculations were conducted using Gaussian 16 software<sup>94</sup> employing the restricted Kohn-Sham formalism for neutral species and the unrestricted formalism for cationic species. We used the BPW91<sup>95</sup> functional, within the generalized gradient approximation (GGA), for preliminary geometry and ground-state energy calculations alongside with the 6-311G\* and 6-311+G\* basis sets.<sup>96</sup> After these preliminary calculations, neutral and cation geometries were optimized with the hybrid GGA B3LYP,<sup>40,42</sup> the hybrid meta-GGA M06,<sup>97</sup> and the long-range-corrected hybrid GGA CAM-B3LYP<sup>45</sup> and  $\omega$ B97XD<sup>46</sup> functionals in their different combinations with the 6-311+G\*,<sup>96</sup> CBSB7,<sup>98</sup> AUG-cc-pVDZ,<sup>99</sup> and Def2TZVPP<sup>100</sup> basis sets. The convergence threshold for total energy was set to  $10^{-8}$  eV while the force threshold was set to  $10^{-3}$  eV/Å.

The calculated adiabatic and vertical ionization energies in units of eV, along with comparison to photoelectron spectroscopy experiments<sup>101,102</sup> are given in Table 4.1. The numbers shown within parentheses are the signed errors of calculated values with respect to the corresponding experimental quantities with negative numbers indicating underestimation and positive numbers indicating overestimation. Clearly, the BPW91 functional used

for preliminary calculations performed poorly. Long-range-corrected hybrid GGA CAM-B3LYP and  $\omega$ B97XD functionals overestimated adiabatic and vertical ionization energies in all cases with the combinations CAM-B3LYP/AUG-cc-pVDZ,  $\omega$ B97XD/AUG-cc-pVDZ, and  $\omega$ B97XD/Def2TZVPP giving deviations around 1 eV from the vertical experimental value. Estimations obtained with the M06 functional agree within 0.15 and 0.05 eV to the experimental adiabatic and vertical values respectively with the M06/Def2TZVPP level of theory giving the most accurate results. The agreement for B3LYP calculations falls within 0.09 and 0.04 eV for adiabatic and vertical quantities with the combinations with the CBSB7, AUG-cc-pVDZ, and Def2TZVPP basis sets performing accurate estimations of both experimental quantities. Particularly, the value obtained at the B3LYP/Def2TZVPP level of theory matches the vertical experimental measurement. Due to these reasons we decided to undergo further benchmarking considering the B3LYP and M06 functionals and their combination with the Def2TZVPP basis set.

Additionally, we calculated the vertical ionization energy at the equation-of-motion ionization-potential coupled-cluster singles and doubles (EOM-IP-CCSD)<sup>103</sup> level in conjunction with the 6-311+G\* basis set considering NB optimized geometry at the B3LYP/Def2TZVPP level using Q-Chem 5.3.<sup>104</sup> The optimized geometries of neutral NB and NB cation obtained at the B3LYP/Def2TZVPP level of theory are given in the Appendix A, Table A1.

The frequencies and intensities of the vibrational modes in both the neutral molecule and the cation were calculated via normal mode analysis. In neutral NB, the values of the harmonic vibrational frequencies depended on whether the B3LYP or the M06 functional was used but, given a certain functional, the frequencies and intensities did not depend strongly on the basis set chosen. Figure 4.1 shows the comparison between the predicted infrared spectra for the neutral molecule at the B3LYP/Def2TZVPP (red) and M06/Def2TZVPP (blue) levels to the experimental gas-phase spectrum obtained from NIST.<sup>105</sup> The calculated harmonic frequencies match the experimental peaks reasonably well in the range of  $\sim 500$ - $2000\text{ cm}^{-1}$ , but it is evident that the B3LYP/Def2TZVPP level of theory offers the best estimation. This agreement indicates the effectiveness of the method and suggests that the computed cation frequencies should be reasonably accurate. Figures A1 and A2 of the Appendix A show the comparison between the experimental infrared spectrum and the calculated spectra using the B3LYP and M06 functionals in combination with all the basis sets explored in this study. Full

method	IE <sub>ad</sub>	IE <sub>vert</sub>
B3LYP/6-311+G*	9.69 (0.09)	10.03 (0.04)
B3LYP/CBSB7	9.61 (0.01)	9.96 (-0.03)
B3LYP/AUG-cc-pVDZ	9.62 (0.02)	9.97 (-0.02)
B3LYP/Def2TZVPP	9.64 (0.04)	9.99 (0.00)
M06/6-311+G*	9.75 (0.15)	10.04 (0.05)
M06/CBSB7	9.70 (0.10)	10.01 (0.02)
M06/AUG-cc-pVDZ	9.70 (0.10)	9.98 (-0.01)
M06/Def2TZVPP	9.64 (0.04)	9.95 (-0.04)
CAM-B3LYP/6-311+G*	9.89 (0.29)	10.13 (0.14)
CAM-B3LYP/CBSB7	9.81 (0.21)	10.07 (0.08)
CAM-B3LYP/AUG-cc-pVDZ	9.81 (0.21)	11.01 (1.02)
CAM-B3LYP/Def2TZVPP	9.83 (0.23)	10.09 (0.10)
$\omega$ B97XD/6-311+G*	9.83 (0.23)	10.09 (0.10)
$\omega$ B97XD/CBSB7	9.78 (0.18)	10.06 (0.07)
$\omega$ B97XD/AUG-cc-pVDZ	9.75 (0.15)	10.95 (0.96)
$\omega$ B97XD/Def2TZVPP	9.75 (0.15)	10.95 (0.96)
BPW91/6-311G*	9.26 (-0.34)	9.61 (-0.38)
BPW91/6-311+G*	9.36 (-0.25)	9.70 (-0.29)
EOM-IP-CCSD/6-311+G*		10.06 (0.07)
Expt.	9.6 <sup>a</sup>	9.99 <sup>b</sup>

<sup>a</sup> Ref. <sup>101</sup> <sup>b</sup> Ref. <sup>102</sup>

Table 4.1: Calculated adiabatic and vertical ionization energies for NB and comparison to experimental values in literature, in units of eV. Numbers within parentheses are signed errors with respect to experimental quantities.

tabulated results of the harmonic vibrational frequencies and their corresponding intensities for the neutral molecule and its cation are presented in the Appendix A, Tables A3 through A6.

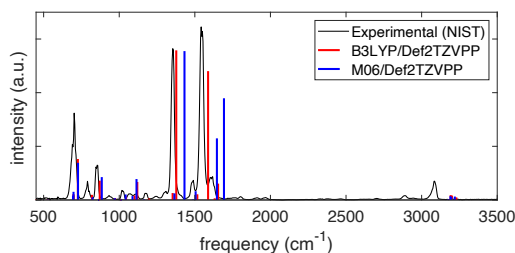


Figure 4.1: Experimental (black) and computed infrared spectra at the B3LYP/Def2TZVPP (red) and M06/Def2TZVPP (blue) levels of theory for NB.

To determine the excited-state energies of the neutral and cationic NB, we performed time-dependent DFT (TDDFT)<sup>106</sup> calculations using Gaussian 16. We calculated the first 10 singlet-singlet (for neutral NB) and doublet-doublet (for NB cation) transitions with the B3LYP and M06 functionals in combination with the above-mentioned four basis sets. We

found an analogous behavior to that of simulated IR spectra: the dependence on the functional was stronger than that of the basis set. Figure 4.2 shows the comparison of the experimental spectra for NB dissolved in methanol and in chloroform with the calculated ones at the B3LYP/Def2TZVPP and M06/Def2TZVPP levels. Experimental spectra in two solvents (see Section 4.2.2) are shown to illustrate any solvatochromic effects due to solvent polarity and ensure a reasonable comparison between experimental and calculated spectra. The better agreement of the computation at the B3LYP/Def2TZVPP level with the experiment follows in line with the previous bench-marking criteria. Unfortunately, the good performance of the B3LYP/Def2TZVPP level of theory in predicting the excitation spectrum of neutral NB cannot be extrapolated to NB radical cation. In section 4.3.1 we will present TDDFT excited-state calculations for NB radical cation at the B3LYP/Def2TZVPP level but those calculations will be further supported with selected calculations at the equation-of-motion excitation-energies coupled-cluster singles and doubles (EOM-EE-CCSD)<sup>103</sup> level. These EOM calculations were performed using Q-Chem 5.3. The comparison of the experimental UV-vis spectrum of NB dissolved in methanol with the spectra calculated using B3LYP and M06 functionals in combination with all the basis sets considered in this work can be seen in Figure A3 of the Appendix A. Full tabulated results of the excitation energies and their corresponding oscillator strengths for neutral and cationic NB are presented in Tables A7 through A10 of the Appendix A.

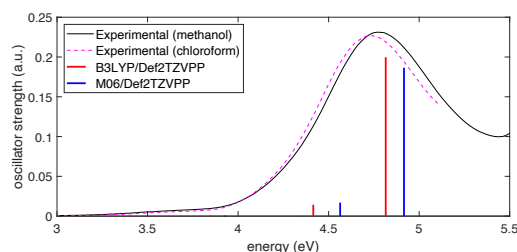


Figure 4.2: Experimental UV-vis spectra for NB in methanol (black) and chloroform (dashed magenta) and comparison with computed spectra at the B3LYP/Def2TZVPP (red) and M06/Def2TZVPP (blue) levels of theory.

## 4.2.2 Experiment

The experimental setups have been described in detail in our previous work.<sup>4,77,107,108</sup> Briefly, a commercial Ti:sapphire regenerative amplifier (Astrella, Coherent Inc.) with a center wavelength of 800 nm, energy of 2 mJ, and pulse duration of 30 fs was used to generate pump

and probe beams. Appropriate beam blocks and laser safety goggles were used at all times to minimize hazards of laser beam exposure. The pump beam was taken from the output of a commercial optical parametric amplifier (OPA, TOPAS prime) with the wavelength set to 1300 nm. Two probe beamlines were used: (i) 800 nm, taken from a small portion of the laser output split with a beamsplitter before the OPA;<sup>4,107</sup> and (ii) 650 nm, taken from a portion of the OPA output that was subsequently split with a beamsplitter and frequency-doubled in a  $\beta$ -barium borate (BBO) crystal.<sup>77</sup> The time-delay between the pump and each probe pulse was scanned using independently controlled motorized translational stages (ThorLabs, Inc) on each probe beamline. The energy of each probe pulse was controlled with a variable neutral density filter. Pulse durations measured with frequency-resolved optical gating (FROG) in our previous work<sup>4,77</sup> were 18 fs (1300 nm pump) and 25 fs (800 nm and 650 nm probes). The cross-correlation of pump and probe pulses, and therefore the temporal resolution of our experiment, was also measured in a previous work<sup>4</sup> and shown to follow a Gaussian shape with FWHM of  $26.1 \pm 0.2$  fs, consistent with the FROG measurements. For both setups, the pump and probe pulses were recombined on dichroic mirrors and directed colinearly through a 20 cm fused silica biconvex lens to focus into an ultrahigh vacuum chamber (base pressure  $2 \times 10^{-9}$  Torr) equipped with a custom built linear time-of-flight mass spectrometer (TOF-MS) described in detail in our previous publications.<sup>107,108</sup> Samples of nitrobenzene and 2-, 3-, and 4-nitrotoluene (Sigma Aldrich) were used as received and introduced into the vacuum chamber through a variable leak valve to reach working pressure in the range of  $1 - 3 \times 10^{-7}$  Torr measured at the MCP detector. Mass spectra were recorded with a 1 GHz digital oscilloscope at a sampling rate of 20 giga samples per second (GS/s) (LeCroy WaveRunner 610Zi). The reported mass spectra were averaged over 10,000 laser shots and transient ion signals obtained by averaging 30 pump-probe scans taken in time steps of 10 fs with 1000 laser shots averaged at each time step. The UV-vis spectra of NB at an approximate concentration of  $5 \times 10^{-5}$  M in methanol and chloroform were measured using a commercial UV-vis spectrophotometer (Agilent 8453).

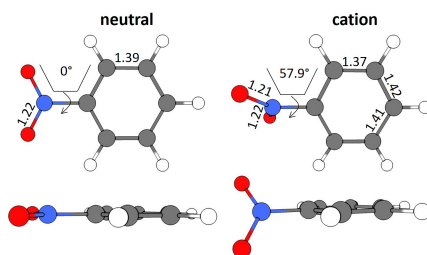


Figure 4.3: Geometrical structures for neutral and cationic NB optimized at the B3LYP/Def2TZVPP level of theory. Bond lengths are in Å and torsional angles in degrees.

## 4.3 Results

### 4.3.1 Computational results

The B3LYP/Def2TZVPP optimized geometry for neutral NB shifts from a  $0^\circ$  C–C–N–O dihedral angle to a  $57.9^\circ$  for the optimized cation, this being the most dramatic geometrical change between both structures (Figure 4.3). In order to confirm the previous assertion, we performed a quantitative measurement of geometric change between the two structures by means of what can be called modified root-mean-square distance (MRMSD) defined as  $\sqrt{\sum_{i=1}^n d_i^2}$  where the set of  $d_i$  values corresponds to the minimized distances between individual atoms in both structures. Using this definition, the MRMSD is 2.62 Å for oxygen atoms and 2.65 Å for all the atoms meaning that most of the geometric changes when going from the neutral to the cationic structure can be accounted for by the movement of the oxygen atoms. For a full list of MRMSD values see Table A2 of the Appendix A. Hence, motion along the C–NO<sub>2</sub> torsional coordinate is expected to dominate the nuclear dynamics of NB following ionization. This result also suggests that the C–NO<sub>2</sub> torsional mode may be coherently excited upon ionization to produce a vibrational wave packet in the C–NO<sub>2</sub> torsional mode. The frequency of this mode calculated using the B3LYP functional ranges from 31.8 to 67.6 cm<sup>−1</sup>, depending on the basis set used, with a value of 53.9 cm<sup>−1</sup> for the B3LYP/Def2TZVPP level of theory (Appendix A, Table A5). These computationally obtained values are in reasonable agreement with the experimental ion signal oscillations at 80 cm<sup>−1</sup> (see Section 4.3.3). The error between computed and experimental frequencies follows in line with that found in a previous work for same torsional mode in 4-NT cation for which computed and experimental frequencies of 46.1 and 85 cm<sup>−1</sup> respectively were found.<sup>4</sup>

Previous femtosecond mass spectrometry measurements on NB have identified the most

prominent ion signal as the  $\text{C}_6\text{H}_5^+$  fragment, obtained by  $\text{NO}_2$  loss from the parent  $\text{NB}^+$  ion.<sup>90–93</sup> To determine the energy needed for  $\text{C}_6\text{H}_5^+$  generation, we performed a relaxed potential energy surface scan for the C–N bond in  $\text{NB}^+$  using the ModRedundant keyword in Gaussian at the B3LYP/Def2TZVPP level of theory (Figure 4.4). The depth of the well obtained from this surface is around 1.58 eV. We estimated the zero point energy (ZPE) by adding the ZPE of the vibrational modes that heavily involve C–N bond stretching (modes 5, 10, 12, 21, 25, 27, 29, and 31, whose corresponding frequencies can be found in Table A5 of the Appendix A). The result of this estimation was 0.55 eV (dashed black line in Figure 4.4), which is reasonable since the total ZPE calculated by Gaussian, adding the ZPE for the 36 vibrational modes of NB, is 2.72 eV. Taking the ZPE into account it can be estimated that the minimum energy necessary for breaking the  $\text{C}_6\text{H}_5\text{--NO}_2$  bond is 1.03 eV (1.58–0.55 eV), less than the energy corresponding to 800 nm photons (1.55 eV) and very close to the energy of 1300 nm photons (0.95 eV) as can be seen in Figure 4.4.

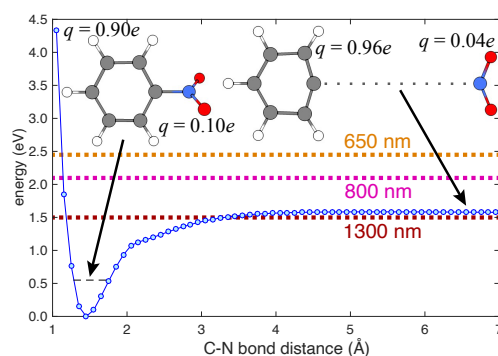


Figure 4.4: Potential energy surface corresponding to the  $\text{C}_6\text{H}_5\text{--NO}_2$  bond stretching in NB cation calculated at the B3LYP/Def2TZVPP level of theory. Charges on each fragment are indicated at C–N distances of 1.45 Å and 6.50 Å. The estimation of the ZPE is shown as a dashed black line. The energies for 1300, 800, and 650 nm photons, relative to the ZPE, are shown as dark red, magenta, and orange dashed lines respectively.

The ground and lowest 10 excited electronic potential energy surfaces (PESs) of NB cation along the C– $\text{NO}_2$  torsional coordinate were computed to determine potential electronic excitation pathways in NB following ionization (Figure 4.5). As seen in Figure 4.5a, these PESs are distributed within two groups: the first comprised by  $\text{D}_0$  to  $\text{D}_4$  and the second by  $\text{D}_5$  to  $\text{D}_{10}$ . It is evident that the  $\text{D}_2$  through  $\text{D}_4$  surfaces in the first group have a marked dependence on the dihedral angle, reaching their maximum energy value at  $90^\circ$ , whereas the surfaces within the second group have a less pronounced dependence on the dihedral angle. Figure 4.5a also shows the energies corresponding to 1300, 800, and 650 nm photons

for comparison (0.95, 1.55, and 1.91 eV respectively). Only the 650 nm photon energy is enough to promote the  $D_0 \rightarrow D_n$ ,  $n = 1, \dots, 4$  transitions by means of single photon processes at any geometry. Moreover, 650 nm is nearly resonant with the  $D_0 \rightarrow D_4$  transition at a dihedral angle of  $90^\circ$ . For 800 nm photons, the  $D_4$  surface is out of reach from  $D_0$  at most geometries, the  $D_3$  surface is accessible at some geometries, and the  $D_2$  surface is reachable at any geometry. 1300 nm photons can only reach the  $D_2$  through  $D_4$  surfaces from  $D_0$  at dihedral angles near  $0^\circ$ , i.e., near the neutral NB geometry.

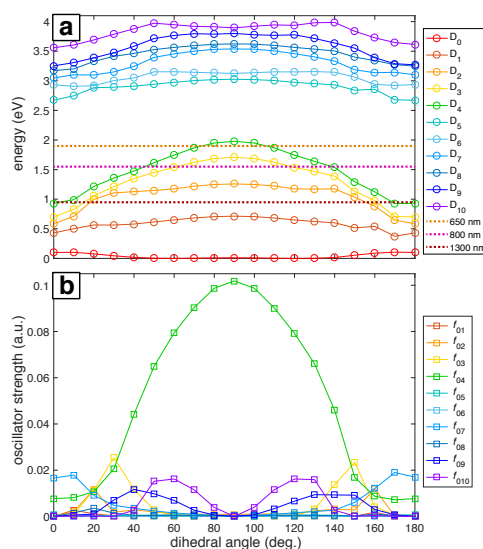


Figure 4.5: (a) Potential energy surfaces for the ground ionic state  $D_0$  and the first ten excited states  $D_1$  through  $D_{10}$  as a function of the C-C-N-O dihedral angle. Energies corresponding to 1300, 800 and 650 nm photons are shown for comparison. (b) Oscillator strengths between the ground ionic state  $D_0$  and the excited states  $D_1$  through  $D_{10}$  as a function of the C-C-N-O dihedral angle. All the calculations were done at the B3LYP/Def2TZVPP level of theory.

The importance of the dihedral angle for excitation probability is captured in the dependence of the oscillator strength on the dihedral angle (Figure 4.5b). Some of the oscillator strengths are very close to zero for all values of the dihedral angle, but  $f_{02}$ ,  $f_{03}$ ,  $f_{04}$ ,  $f_{07}$ ,  $f_{09}$ , and  $f_{010}$  have non-negligible values at different geometries. It is noteworthy that the oscillator strength for the  $D_0 \rightarrow D_4$  transition ( $f_{04}$ ) is particularly high and dependent on the geometry, reaching its maximum value at  $90^\circ$ . Moreover, this transition is the only one that has a substantial oscillator strength at  $90^\circ$  (Table 4.2). In order to support our TDDFT calculations we also performed some computations using a higher level of theory, EOM-EE-CCSD was the method chosen for this purpose in combination with the 6-311+G\* basis set. The geometries considered were the ones obtained after optimization at the B3LYP/Def2TZVPP level. Table

4.2 contains the results of these calculations for NB cation with 90° C–NO<sub>2</sub> torsional angle. Analogous EOM calculations for the optimized neutral and cation geometries are shown in Table A11 of Appendix A. Comparison of results in Table 4.2 shows that EOM calculations confirm the presence of an excited state with a substantial oscillator strength at 90° dihedral angle and with excitation energy around 2 eV, in line with the TDDFT calculations, and very importantly, with the experimental results to be discussed in the following sections. However, the ordering of the excited states is not in complete agreement since EOM results point out D<sub>3</sub> as the relevant state while TDDFT computations point to D<sub>4</sub>. This situation will be briefly discussed in Section 4.4.

transition	B3LYP/ Def2TZVPP		EOM-EE-CCSD/ 6-311+G*	
	EE (eV)	<i>f</i> (a.u.)	EE (eV)	<i>f</i> (a.u.)
D <sub>0</sub> → D <sub>1</sub>	0.73	0.0000	0.8099	0.000003
D <sub>0</sub> → D <sub>2</sub>	1.23	0.0010	1.9994	0.001317
D <sub>0</sub> → D <sub>3</sub>	1.70	0.0000	2.3372	0.115550
D <sub>0</sub> → D <sub>4</sub>	1.99	0.1039	2.4949	0.000116
D <sub>0</sub> → D <sub>5</sub>	3.03	0.0000	3.6971	0.001262
D <sub>0</sub> → D <sub>6</sub>	3.12	0.0000		
D <sub>0</sub> → D <sub>7</sub>	3.54	0.0004		
D <sub>0</sub> → D <sub>8</sub>	3.62	0.0002		
D <sub>0</sub> → D <sub>9</sub>	3.80	0.0000		
D <sub>0</sub> → D <sub>10</sub>	3.89	0.0000		

Table 4.2: Excitation energies (EE) and oscillator strengths (*f*) for NB cation with 90° C–C–N–O dihedral angle at the B3LYP/Def2TZVPP and EOM-EE-CCSD/6-311+G\* levels of theory

Having a substantial oscillator strength for the D<sub>0</sub> → D<sub>4</sub> transition at 90° implies that, as the vibrational wave packet propagates along the D<sub>0</sub> surface, it will have the highest probability of a one-photon excitation to the D<sub>4</sub> surface at that particular dihedral angle. Hence, we can expect that pump-probe measurements using 650 nm probe photons will most efficiently transfer ground-state NB<sup>+</sup> to the D<sub>4</sub> surface at pump-probe delays corresponding to the time needed for the wave packet to reach a 90° dihedral angle. To estimate this time we performed wave packet trajectory calculations<sup>71,109</sup> using the D<sub>0</sub> surface computed in fine increments of 2° (red dots, Figure 4.6) and fit to a smoothing spline (solid red line, Figure 4.6). The evolution of the dihedral angle of the wave packet centroid is determined by the equation of motion<sup>109</sup>

$$\frac{d\varphi}{dt} = \sqrt{\frac{2}{I} (V(\varphi(0)) - V(\varphi(t)) + \Delta)} \quad (4.1)$$

where  $\varphi$  is the dihedral angle,  $I$  is the reduced moment of inertia for the torsional motion,

and  $V(\varphi(t))$  is the potential energy dependent on the dihedral angle at a given time  $t$  (a point of the  $D_0$  surface). The quantity  $\Delta$  represents additional energy available from relaxation following vertical ionization. This equation was solved using the numerical integrator `ode45` in MATLAB with the computed reduced moment of inertia of  $4.46 \times 10^{-46}$  kg m<sup>2</sup>.

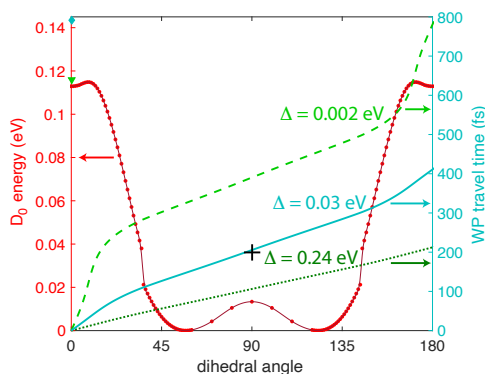


Figure 4.6: Calculated wave packet trajectories over the  $D_0$  PES (red dots and line) using 0 (bright green dashed line), 0.03 (turquoise solid line), and 0.24 eV (dark green dotted line) of excess energy.

From Figure 4.6 we can see a local minimum in the  $D_0$  surface at  $0^\circ$  dihedral angle; if we consider this surface as periodic, that local minimum constitutes a potential well. On the computed  $D_0$  surface, the wave packet will need at least  $\Delta \geq 0.002$  eV excess energy to surpass the barrier at  $\sim 9^\circ$  dihedral angle. It is reasonable to assume that the source of that energy is some fraction of the excess energy after ionization considered as the difference between vertical and adiabatic ionization energies. At the B3LYP/Def2TZVPP level, this excess energy is 0.35 eV (Table 4.1), giving an upper limit of  $\Delta = 0.24$  eV in eq (4.1). Figure 4.6 shows the wave packet trajectories along the  $D_0$  PES (red line) obtained with  $\Delta = 0.002$  eV (light green dashed line),  $\Delta = 0.03$  eV (turquoise solid line), and  $\Delta = 0.24$  eV (dark green dotted line). As expected, the time taken for the wave packet to reach a  $90^\circ$  dihedral angle changes with the value of  $\Delta$ , with times around 400, 200, and 100 fs for  $\Delta = 0, 0.03$ , and 0.24 eV, respectively. Therefore, the physically plausible assumption of using  $\Delta = 0.03$  eV, or 9% of the available relaxation energy, to “kick-start” the wave packet, leads to a trajectory in which the wave packet reaches the  $90^\circ$  torsional angle in  $\sim 200$  fs, a result that follows in line with the pump-probe experiments discussed in the following sections.

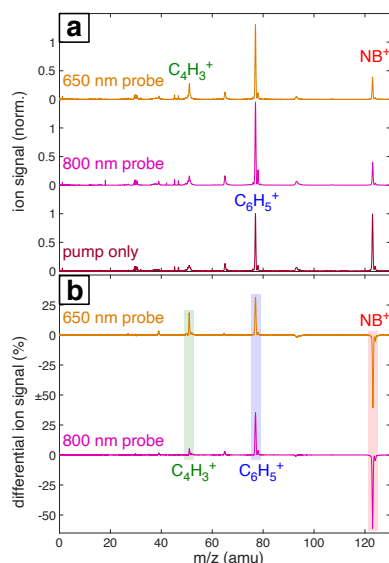


Figure 4.7: (a) Mass spectra of NB taken with 1300 nm pump only (dark red, bottom), 800 nm probe (magenta, middle), and 650 nm probe (orange, top) at 4 ps delay. (b) Difference mass spectra between the 800 nm and 650 nm probe spectra and pump-only spectrum in (a). The signals for parent ion  $NB^+$  (red),  $C_6H_5^+$  (blue), and  $C_4H_3^+$  (green) are highlighted.

### 4.3.2 Pump-probe measurements

Figure 6.3a shows the mass spectra of NB taken with  $7 \times 10^{13} \text{ W cm}^{-2}$ , 1300 nm pump pulses and  $1 \times 10^{13} \text{ W cm}^{-2}$  probe pulses at 800 nm and 650 nm, with the delay  $\tau$  between pump and probe pulses set to 4 ps. The bottom spectrum (dark red) obtained using only the 1300 nm ionizing pump pulse exhibits significant yields of parent molecular ion  $NB^+$  ( $m/z$  123) and  $C_6H_5^+$  ( $m/z$  77) with little additional fragmentation. Notably, the similar intensity of the parent  $NB^+$  and  $C_6H_5^+$  peaks stands in stark contrast to earlier measurements on NB using 800 nm fs excitation for ionization, where the  $C_6H_5^+$  signal was at least an order of magnitude more intense than the  $NB^+$  signal.<sup>90–92</sup> This result is expected on the basis of the computed PES along the C–N bond coordinate (Figure 4.4), which shows that 800 nm photons substantially exceed the energy needed for  $NO_2$  loss, whereas 1300 nm photons barely provide sufficient energy. When an 800 nm (middle spectrum, magenta) or 650 nm (top spectrum, orange) probe pulse is present at a 4 ps delay, the relative yield of the parent  $NB^+$  ion decreases by  $\sim 60\%$ , while the yields of the  $C_6H_5^+$  and  $C_4H_3^+$  ( $m/z$  51) fragments increase. These changes are further magnified in the difference spectra shown in Figure 6.3b. Whereas parent depletion and  $C_6H_5^+$  enhancement are similar for both 800 nm and 650 nm probe photons, the enhancement of  $C_4H_3^+$  is significantly higher using 650 nm photons. While the  $C_6H_5^+$  fragment is clearly the  $NO_2$  loss product from the parent ion, the origin of

the  $C_4H_3^+$  fragment has not been completely elucidated. Threshold photoelectron-photoion coincidence (TPEPICO) spectroscopy experiments suggest that the  $C_4H_3^+$  fragment can be formed from secondary dissociation of  $C_6H_5^+$ .<sup>110</sup>

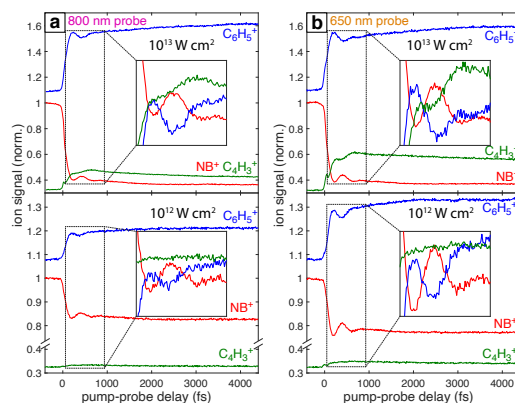


Figure 4.8: Transient ion signals from  $NB^+$  obtained with (a) 800 nm and (b) 650 nm probe pulses. Probe intensity is  $10^{13} \text{ W cm}^{-2}$  (top panels) and  $10^{12} \text{ W cm}^{-2}$  (bottom panels). Insets magnify the 70–830 fs range to show the oscillations, curves within the inset have been shifted vertically to show oscillatory behavior more clearly.

Figure 5.3.1 shows the transient signals of the ions highlighted in Figure 6.3 as a function of pump-probe delay ( $\tau$ ) using 800 nm (a) and 650 nm (b) probe pulses at intensities  $10^{13} \text{ W cm}^{-2}$  (top) and  $10^{12} \text{ W cm}^{-2}$  (bottom). All transients are normalized to the yield of  $NB^+$  at  $\tau < 0$ . Depletion in  $NB^+$  (red) and increase in  $C_6H_5^+$  (blue) signals at  $\tau > 0$  are observed under all conditions, with greater magnitude changes for high probe intensity (top panels) due to increased excitation probability. The yield of  $C_4H_3^+$  increases significantly for  $\tau > 0$  only at  $10^{13} \text{ W cm}^{-2}$ , with greater enhancement for the 650 nm wavelength. The antiphase oscillations in the yields of  $NB^+$  and  $C_6H_5^+$  (inset in each panel of Figure 5.3.1), with similar frequency to related aromatic molecules,<sup>4,69–72,77</sup> indicate that electronic excitation of the  $NB^+$  vibrational wave packet along the  $C-NO_2$  torsional mode (Figures 4.3 and 4.5) results in  $C_6H_5^+$  formation. The greater oscillation amplitude using the 650 nm wavelength, particularly at lower intensity (bottom panels), is consistent with the prediction based on the computed PESs in Figure 4.5 that 650 nm photons are more efficient at exciting the  $NB^+$  vibrational wave packet.

### 4.3.3 Quantitative analysis of oscillatory dynamics

To quantify the enhancement of oscillation amplitudes observed in the transient signals in Figure 5.3.1 using the 650 nm probe wavelength, nonlinear least squares curve fitting<sup>3,4,71–74,77</sup> was applied to the signals. The fit equation used for the transient ion signals in Figure 5.3.1 is

$$S(\tau) = ae^{-\tau/T_1} \cos\left(\frac{2\pi}{t}\tau + \phi\right) + be^{-\tau/T_2} + ce^{-\tau/T_3} + d \quad (4.2)$$

where  $a$ ,  $b$ , and  $c$  are amplitude coefficients,  $t$  is the oscillation period,  $T_1$  is the coherence lifetime,  $T_2$  and  $T_3$  are incoherent lifetimes (i.e., not associated with oscillations), and  $d$  is the ion yield as  $\tau \rightarrow \infty$ . Each transient signal at  $\tau \geq 70$  fs (i.e., after the pump pulse is over so the instrument response function can be ignored) was fit to eq (C.1) using nonlinear least-squares curve fitting in MATLAB, as illustrated in the Appendix A, Figure A4.

eq (C.1)	$a$	$T_1$ (fs)	$t$ (fs)	$\phi$ (rad)
650 nm, $I = 10^{13}$	$0.14 \pm 0.02$	$239 \pm 15$	$430 \pm 9$	$-0.08 \pm 0.09$
650 nm, $I = 10^{12}$	$0.11 \pm 0.02$	$242 \pm 15$	$426 \pm 10$	$-0.04 \pm 0.08$
800 nm, $I = 10^{13}$	$0.08 \pm 0.01$	$244 \pm 24$	$439 \pm 15$	$-0.13 \pm 0.19$
800 nm, $I = 10^{12}$	$0.05 \pm 0.01$	$225 \pm 41$	$426 \pm 10$	$-0.05 \pm 0.21$

Table 4.3: Coefficients for NB<sup>+</sup> transients fit to eq (C.1).  $I$ : probe intensity in W cm<sup>-2</sup>

Under all conditions, the parent NB<sup>+</sup> ion was fit to the complete eq C.1, C<sub>6</sub>H<sub>5</sub><sup>+</sup> fit to eq C.1 without the  $T_3$  component, and C<sub>4</sub>H<sub>3</sub><sup>+</sup> fit to the complete eq C.1 for 650 nm excitation at  $10^{13}$  W cm<sup>-2</sup> or without the oscillatory  $T_1$  component otherwise (Appendix A, Tables A12–A15). To compare the oscillatory dynamics observed under the four experimental conditions in Figure 5.3.1, the tabulated  $a$ ,  $T_1$ ,  $t$ , and  $\phi$  coefficients for the parent NB<sup>+</sup> ion extracted from curve fitting are reported in Table 5.1. For all four conditions, the coherence lifetime  $T_1$ , oscillation period  $t$ , and phase  $\phi$  agree to within the reported errors (95% confidence intervals from curve fitting). This result confirms that the same initial wave packet was prepared by the ionizing pump pulse because the parameters  $T_1$ ,  $t$ , and  $\phi$  are intrinsic to the wave packet dynamics. In contrast, the  $a$  coefficients associated with the oscillation amplitude are greater for 650 nm as compared to 800 nm excitation: the  $a$  value of  $0.11 \pm 0.02$  obtained with 650 nm is twice the  $0.05 \pm 0.01$  value obtained with 800 nm at the modest intensity of  $10^{12}$  W cm<sup>-2</sup>. This result is consistent with the more prominent oscillations visible in Figure 5.3.1b

as compared to Figure 5.3.1a. Greater values of  $a$  coefficients for the  $C_6H_5^+$  fragment are also observed with 650 nm probe as compared to 800 nm probe (Appendix A, Tables A12–A15).

To further illustrate the enhancement of the oscillatory ion signals using 650 nm excitation, the residual oscillatory ion signals obtained after subtraction of the incoherent components ( $T_2$  and  $T_3$  terms) from eq C.1 are plotted in Figure 4.9, left panel. This plot clearly shows the antiphase behavior of the oscillations in  $NB^+$  (red) and  $C_6H_5^+$  (blue), as indicated by the dotted lines at the minima of  $NB^+$  yield (200 and 630 fs). For 650 nm excitation at  $10^{13} \text{ W cm}^{-2}$ , the  $C_4H_3^+$  (green) fragment also exhibits antiphase oscillations with respect to  $NB^+$ . At both intensities, the larger-amplitude oscillations using 650 nm are apparent in the increased amplitude of the corresponding Fast Fourier Transform (FFT) peak at  $80 \text{ cm}^{-1}$  (dashed line) taken from the residual ion signals over the pump-probe delay range of 70–3000 fs (Figure 4.9, right panel). In particular, the  $80 \text{ cm}^{-1}$  peak intensity for  $NB^+$  at  $10^{12} \text{ W cm}^{-2}$  is approximately five times higher for 650 nm as compared to 800 nm excitation. Hence, quantification of the oscillations indicate an amplitude enhancement by a factor of  $\sim 2$ – $5$  using 650 nm for excitation as compared to 800 nm, consistent with the theoretical predictions from Figure 4.5.

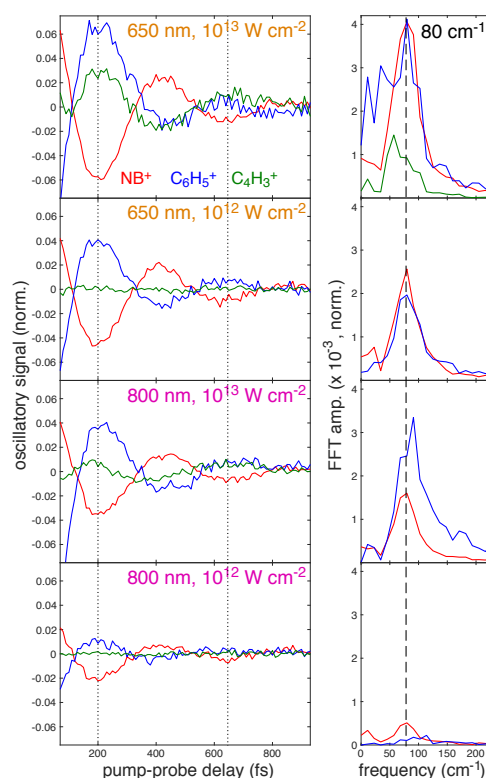


Figure 4.9: Residual ion signals (left) and FFT power spectra (right).

### 4.3.4 Comparison of nitrobenzene and nitrotoluenes

In order to further explore the effect of the probe excitation wavelength in the study of radical cation dynamics, we briefly discuss the occurrence of analogous behaviors in the closely related nitrotoluenes (NTs). Figure 4.10 shows the transient ion signals for the parent ions  $M^+$  and the  $\text{NO}_2$  loss products for 4-NT, 3-NT, and 2-NT as well as nitrobenzene for comparison. Measurements were taken with  $7 \times 10^{13} \text{ W cm}^{-2}$ , 1300 nm pump pulses and  $1 \times 10^{12} \text{ W cm}^{-2}$  probe pulses at 800 nm and 650 nm for all the molecules except for 3-NT, for which probe pulses of  $6 \times 10^{12} \text{ W cm}^{-2}$  were used. Among these four molecules, NB stands out in that the  $[M-\text{NO}_2]^+$  fragment has a higher yield than the parent ion  $M^+$  at negative delay, which is attributed to NB having the lowest C–N bond dissociation energy (BDE) as indicated in Figure 4.10. Although the BDE in 2-NT is similar (1.56 eV in NB vs. 1.58 eV in 2-NT), the 2-NT can undergo additional fragmentation pathways that compete with C–N cleavage,<sup>77</sup> as shown in the mass spectra in the Appendix A, Figure A5. Nevertheless, all these systems with the exception of 3-NT show a similar enhancement of the oscillatory dynamics with 650 nm excitation as compared with 800 nm. We note that the lack of enhanced  $[M-\text{NO}_2]^+$  yield in 2-NT can also be attributed to competition with other fragmentation pathways. Our previous finding that the optimized 2-NT cation has an excited state nearly resonant with 650 nm using TDDFT calculations at the  $\omega\text{B97XD/CBSB7}$  and  $\text{CAM-B3LYP/CBSB7}$  levels<sup>77</sup> further supports the main hypothesis explored in this work that computations can predict the best excitation wavelength. On the basis of these results, we can predict the existence of a resonant transition at 650 nm for 4-NT and the absence of such a resonance for 3-NT, which may be expected because 3-NT does not undergo torsional wave packet motion upon ionization.<sup>4</sup> We note that the common behavior of NB, 2-NT, and 4-NT cations with regards to torsional wave packet motion and accessible electronic transitions is similar to previous studies of acetophenone<sup>71,72</sup> and its methyl-substituted derivatives<sup>69,70</sup>: acetophenone, 2-methylacetophenone, and 4-methylacetophenone undergo torsional wave packet motion that can be excited with an 800 nm probe, whereas 3-methylacetophenone does not.

## 4.4 Discussion

It is common practice in time-resolved studies of radical cations to probe with the readily available 800 nm wavelength.<sup>3,4,66–75</sup> In this work we want to address whether theoretical

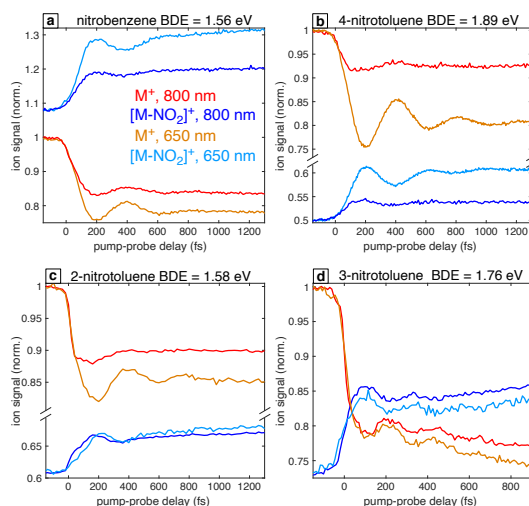


Figure 4.10: Transient ion signals of parent ions  $M^+$  (red and orange) and  $[M-NO_2]^+$  (dark and light blue) for NB (a), 4-NT (b), 2-NT (c), and 3-NT (d). Bond dissociation energies (BDE) of the C–N bond calculated at the B3LYP/Def2TZVPP level for these four radical cations are also shown.

computations can predict a more suitable wavelength for probing vibrational wave packet dynamics in radical cations. Indeed, the enhancement of wave packet oscillation amplitudes in NB cation at modest probe pulse intensity ( $10^{12} \text{ W cm}^{-2}$ ) using 650 nm as compared to 800 nm for excitation validates the computational results showing a geometry-dependent excitation probability from the  $D_0$  to  $D_4$  surface and resonance of the 650 nm excitation wavelength. These results will be further discussed in this section.

Both the 650 and 800 nm excitation wavelengths are capable of increasing the  $C_6H_5^+$  signal at the expense of the parent ion signal (Figure 6.3), even though only the 650 nm probe is capable of promoting the  $D_0 \rightarrow D_4$  transition for any geometry according to our TDDFT calculations (Figure 4.5a). This result is consistent with previous mass spectrometry studies using only one 800 nm pulse for ionization that show substantial  $C_6H_5^+$  ion signal and little parent ion,<sup>90–92</sup> and suggests that ionization of NB at 800 nm can populate one or more electronic excited states of the cation. Because the 800 nm wavelength can access the  $D_2$  excited state at all geometries, excitation to  $D_2$  is likely sufficient to produce  $NO_2$  loss, at least at geometries where its energy is above the estimated dissociation threshold of 1.03 eV (Figure 4.4). We cannot rule out the contribution of the  $D_3$  excited state to the dissociative event because 800 nm excitation is also able to promote the  $D_0 \rightarrow D_3$  transition for some geometries. The participation of the  $D_0 \rightarrow D_1$  transition can be excluded due to the negligible values of  $f_{01}$  (Figure 4.5b) and more importantly because the energy of the  $D_1$  excited state

at any geometry lies below the minimum energy to break the C–N bond. Hence, the key difference between 800 nm and 650 nm excitation is that only 650 nm gives full accessibility to the  $D_4$  surface, for which the coupling strength to  $D_0$  has a strong geometric dependence. This circumstance explains the enhanced oscillatory behavior for 650 nm excitation (Figures 5.3.1 and 4.9).

The observation that the 650 nm excitation is more efficient at generating the  $C_4H_3^+$  fragment as compared to the 800 nm excitation (Figure 6.3b) suggests that the excited state(s) involved should be at the reach of the 650 nm wavelength to a greater extent than for 800 nm. In addition, the finding of substantially enhanced  $C_4H_3^+$  yield at high probe intensity ( $10^{13}$  W cm $^{-2}$ , top panels of Figure 5.3.1) as compared to modest probe intensity ( $10^{12}$  W cm $^{-2}$ , bottom panels of Figure 5.3.1) supports the idea that the excited state(s) responsible for  $C_4H_3^+$  formation can only be reached by means of a two-photon process. These facts suggest that the two photon process(es) involved in the  $C_4H_3^+$  fragment production are more efficient for the 650 nm probe as compared to the 800 nm. Moreover, we can postulate the existence of a two-photon resonant process achievable only with the 650 nm excitation. After eliminating the incoherent part from the  $C_4H_3^+$  transient, the oscillatory nature of the transient is only observed with 650 nm probe, whereas the transient for the 800 nm probe only shows a feeble oscillatory behavior (Figure 4.9). Because the  $D_5$  and  $D_6$  PESs do not depend on the dihedral angle while the  $D_7$  to  $D_{10}$  PESs show a modest dependence (Figure 4.5a), we can postulate that the excited state(s) involved in the two photon process generating  $C_4H_3^+$  lie(s) between  $D_7$  and  $D_{10}$ . These states span an excitation energy range from 3.54 to 3.89 eV (Table 4.2), which can be reached with two 650 nm photons (3.82 eV). The dependence on geometry for the  $D_7$  to  $D_{10}$  PESs could be associated with the oscillatory behavior observed for the 650 nm probe. On the other hand, the energy corresponding to two 800 nm photons (3.10 eV) cannot reach the  $D_7$  and higher states. As a last observation we want to point out that the residual ion signal for  $C_4H_3^+$  shows antiphase coupling between  $NB^+$  and  $C_4H_3^+$  (Figure 4.9), suggesting that the  $C_4H_3^+$  fragment originates from the  $D_0$  surface of the parent ion. This result suggests that two-photon excitation of  $NB^+$  provides sufficient energy to further fragment initially formed  $C_6H_5^+$  into  $C_4H_3^+$ , as observed in TPEPICO studies.<sup>110</sup>

Collectively, the results of this work both illustrate how quantum chemical computations can predict the outcome of pump-probe measurements on radical cations and high-light similarities in the observed dynamics, and thereby the similar electronic structures,

of homologous radical cations. Hence, this work builds on previous studies wherein computed electronic PESs of cations including bromiodomethane,<sup>67,68</sup> acetophenone,<sup>71,72</sup> and azobenzene<sup>75</sup> are used to explain transient oscillatory dynamics of ion signals observed in pump-probe measurements. Moreover, this work demonstrates that computations of electronic PESs, even using the inexpensive TDDFT method, provide sufficiently accurate results to predict the best probe excitation wavelength in pump-probe measurements of nitrobenzene and closely related nitroaromatic compounds to maximize the visibility of vibrational wave packet dynamics. However, as the comparison of TDDFT and EOM results in Table 4.2 showed, our inexpensive TDDFT approach is not free of problems and still has room for improvement. Previous works have pointed out deficiencies on the TDDFT description of low-lying singlet excited states of polyacenes<sup>111,112</sup>, thiophene and short thienoacenes<sup>113</sup>, fused heteroaromatic rings<sup>114</sup>, and naphthol isomers<sup>115</sup> to name some examples. Further work should be carried out to fully elucidate the nature of the excited states of nitrobenzene and related nitroaromatic radical cations and to rationalize and possibly improve the drawbacks of their TDDFT description. It is important to emphasize that any extension of this TDDFT approach to different groups of molecules should be carefully evaluated with the aid of higher level methodologies.

Additionally, our results complement previous studies showing that selection of near-infrared wavelengths for the ionizing pump also enhances the visibility of oscillatory ion dynamics by more selectively populating the ground electronic state of the cation.<sup>71,73</sup> Finally, our results provide further evidence that similar coherent vibrational dynamics in radical cations are to be expected for families of homologous molecules.<sup>67,70,74</sup> In particular, the *ortho/para* directing nature of the nitro group is confirmed in our pump-probe measurements due to the completely different dynamics of 3-NT as compared to NB, 2-NT, and 4-NT (Figure 4.10).

## 4.5 Conclusions

We have demonstrated that TDDFT computations of electronic potential energy surfaces in the nitrobenzene radical cation can be used to predict the best choice of the probe wavelength in femtosecond time-resolved mass spectrometry measurements. It was found that the  $D_0 \rightarrow D_4$  transition is both resonant with 650 nm excitation and has a geometry-dependent

oscillator strength, with strongest coupling at a C–C–N–O dihedral angle of  $90^\circ$ . This result predicted the substantial enhancement by a factor of  $\sim 2\text{--}5$  in the ion yield oscillations observed in nitrobenzene cation as a function of pump-probe delay. The analogous behavior observed in the related molecules 2- and 4-nitrotoluene highlights that similar vibrational dynamics are to be expected in pump-probe measurements on homologous molecules. Collectively, our results point to the importance of rationally selecting the probe wavelength for time-resolved measurements of prepared vibrational coherent states on the basis of theoretical results. This knowledge can benefit design of coherent control schemes and quantum information applications.

## Chapter 5

# Controlling fragmentation products with selective wave packet excitation

This chapter is an adapted version of the work in Ref. [116](#):

López Peña, H. A.; Shusterman, J. M.; Ampadu Boateng, D.; Lao, K. U.; Tibbetts, K. M. Coherent Control of Molecular Dissociation by Selective Excitation of Nuclear Wave Packets. *Frontiers in Chemistry* **2022**, 10.

### 5.1 Introduction

Chemists have sought to control molecular dissociation with lasers for decades. Tunable monochromatic laser light was believed to enable “bond-selective chemistry” through resonant energy absorption at the vibrational frequency of the targeted bond<sup>[117](#)</sup>. However, early attempts to control bond-cleavage by tuning the laser frequency failed due to rapid intramolecular vibrational energy redistribution (IVR) across coupled vibrational modes<sup>[118](#)</sup>. Effective control of unimolecular dissociation was only achieved with the development of high-intensity ultrashort pulsed lasers and coherent control techniques that operate on timescales faster than IVR.

Coherent control over molecular dissociation has primarily been achieved by the “closed-loop” scheme of optimally designing shaped laser pulses with automated learning algorithms, initially proposed by Judson and Rabitz<sup>[119](#)</sup>. Gerber and co-workers reported the first experimental implementation of closed-loop control over ionization and dissociation of  $\text{CpFe(CO)}_2\text{Cl}$  (Cp = cyclopentadienyl) into  $\text{CpFeCOCl}^+$  or  $\text{FeCl}^+$ <sup>[120](#)</sup>. This success spurred the application of closed-loop control to selectively dissociate various molecules including

halogenated alkanes<sup>121–124</sup> and acetones<sup>122,125</sup>. However, shaped pulse control fails to enhance specific dissociation pathways in certain molecules including *p*-nitrotoluene<sup>126</sup>. Moreover, the “black box” nature of closed-loop control makes it difficult to fully understand the physical mechanisms by which an optimal pulse shape achieves product selectivity, even using additional specialized pulse shaping procedures<sup>127</sup>.

Understanding the physical mechanisms underlying coherent control of molecular dissociation can be achieved using two-pulse “pump-probe” excitation schemes<sup>128,129</sup>. Pump-probe measurements with complementary quantum chemical calculations of the relevant electronic potential energy surfaces (PESs) have revealed bond-cleavage mechanisms facilitated by coherent vibrational motions in the numerous organic cations<sup>3</sup>. For instance, coherent excitation of the I–C–Br bending mode in  $\text{CH}_2\text{IBr}^+$  upon strong-field ionization facilitates dissociation into  $\text{CH}_2\text{Br}^+$  upon excitation of the  $D_0 \rightarrow D_3$  transition at a specific point on the  $D_0$  PES<sup>67</sup>. Similarly, coherent vibrational motions along the phenyl–substituent torsional coordinate in the molecular cations of acetophenone<sup>71,72</sup> and nitrobenzene<sup>51</sup> facilitate  $\text{CH}_3$  and  $\text{NO}_2$  loss, respectively, upon excitation of the vibrational wave packet at  $90^\circ$  phenyl–substituent dihedral angle. Although pump-probe measurements advance understanding of molecular dissociation facilitated by coherent vibrational dynamics, they enable only limited control over relative fragment yields because the probe wavelength typically excites resonantly to a single electronic excited state. As a result, one preferential fragment or a specific distribution of fragments is usually observed.

In this work, we demonstrate selective coherent excitation to three different electronic excited states from ground-state *p*-nitrotoluene (PNT) cation using probe pulses at 800 nm, 650 nm, and 400 nm. This selective excitation results in different relative yields of the  $\text{C}_7\text{H}_7^+$ ,  $\text{C}_5\text{H}_5^+$ , and  $\text{C}_3\text{H}_3^+$  fragment ions depending on the probe wavelength. Strong field adiabatic ionization prepares a superposition of two vibrational wave packets in the  $D_0$  PES of PNT cation: the first along the C–C–N–O torsional coordinate identified in earlier work<sup>4</sup> and the second along the in-plane phenyl ring-stretching mode that includes C–N bond stretching. The torsional wave packet can be selectively excited to  $D_4$  at a C–C–N–O dihedral angle of  $90^\circ$  with 650 nm photons to produce primarily  $\text{C}_7\text{H}_7^+$ , or to  $D_6$  at a  $0^\circ$  dihedral angle with 400 nm photons to produce  $\text{C}_5\text{H}_5^+$  and  $\text{C}_3\text{H}_3^+$ . The ring-stretching wave packet can be selectively excited to  $D_2$  at a geometry with slightly elongated C–N bond length and  $90^\circ$  dihedral angle using 800 nm photons, producing exclusively  $\text{C}_7\text{H}_7^+$ . These results indicate

that careful choice of excitation wavelengths in two-pulse schemes can effectively control dissociation pathways in a complex organic molecule.

## 5.2 Materials and Methods

### 5.2.1 Experiments

Portions of the experimental setup have been described in our previous works<sup>4,77</sup>. Briefly, a commercial Ti:sapphire regenerative amplifier (Astrella, Coherent, Inc.) producing 30 fs, 800 nm, 2.2 mJ pulses was used to pump an optical parametric amplifier (OPA, TOPAS Prime) to produce sub-20 fs 1300 nm or 1500 nm pump pulses. The pump wavelength was 1300 nm for measurements with the 400 nm and 650 nm probes, whereas the pump wavelength was 1500 nm for measurements with the 800 nm probe for reasons that will be discussed in the Results section. The 650 nm probe pulse was obtained from OPA output split with a 50:50 (r:t) beam splitter and frequency doubled with a  $\beta$ -barium borate (BBO) crystal. The 800 nm probe pulse was obtained from the transmitted portion of the incident laser beam from a 90:10 (r:t) beam splitter prior to the OPA and down-collimated using a reflective telescope with reduction factor 2. The 400 nm probe pulse was obtained by down-collimating the 800 nm beam with a telescope with reduction factor 3.33 comprised of a plano-convex lens ( $f = 250$  mm) and plano-concave lens ( $f = -75$  mm) placed on a linear translation stage, followed by frequency doubling with a BBO crystal. The transmissive telescope geometry was necessary to allow for fine adjustment of the focal spot of the 400 nm probe beam to overlap with the focal spot of the 1300 nm pump beam when both are focused with the same plano-convex lens ( $f = 200$  mm). Both the 800 nm and 650 nm probe pulses have duration of  $\sim 25$  fs as measured by frequency-resolved optical gating<sup>4,77</sup>. The 400 nm probe pulse duration was estimated at 70 fs as measured by the cross-correlation of the O<sub>2</sub> signal from air in the mass spectrometer with 1300 nm pump/400 nm probe excitation (Appendix B, Figure B1). PNT (Sigma Aldrich, 99%) was introduced into the time-of-flight mass spectrometer (Jordan TOF) via an effusive inlet under gentle heating. Pump-probe measurements were taken over the delay range of -500 fs (probe before pump) to +2500 fs (pump before probe) in steps of 5 fs for the 800 nm probe and 10 fs otherwise. Mass spectra were recorded at each pump-probe delay and averaged over 1000 laser shots with a 1 GHz digital oscilloscope (LeCroy WaveRunner 610Zi).

### 5.2.2 Computations

Density functional theory (DFT) calculations were conducted using Gaussian 16 software<sup>130</sup> employing the restricted Kohn-Sham formalism for neutral species and the unrestricted formalism for cationic species. A previous work on PNT from our group<sup>4</sup> has identified the hybrid generalized gradient approximation (GGA) B3LYP functional<sup>42,43</sup> in combination with the def2-TZVPP<sup>131</sup> basis set as an adequate level of theory to describe this molecular system. Both the neutral and cation geometries of PNT were optimized within this level of theory. The convergence threshold for total energy was set to  $10^{-8}$  eV while the force threshold was set to  $10^{-3}$  eV/Å. Each geometric optimization was followed by harmonic frequency computations in order to confirm the stationary character of the state obtained.

To determine the excited-state energies of the PNT cation at different geometries, we performed single-point time-dependent DFT (TDDFT)<sup>106</sup> calculations using Gaussian 16. For each cation geometry, we calculated the first 10 doublet-doublet transitions at the B3LYP/def2-TZVPP level of theory. In section 5.3.2 we will present TDDFT excited-state calculations for PNT radical cation at the B3LYP/def2-TZVPP level but those calculations will be further supported with selected calculations at the equation-of-motion excitation-energies coupled-cluster singles and doubles (EOM-EE-CCSD)<sup>103</sup> level. Due to the high computational cost of EOM methods, we employ the smaller 6-311+G\* basis set. These EOM calculations were performed using Q-Chem 5.3<sup>132</sup>. It is important to clarify that both TDDFT and EOM calculations on the cation are done under field-free conditions, i.e., after the pump pulse is over (see further discussion on Section 5.3.1).

## 5.3 Results

### 5.3.1 Pump-probe measurements

Pump-probe measurements were conducted with pump intensity of  $6 \times 10^{13}$  W cm<sup>-2</sup>. Figure 5.1a shows the mass spectra of PNT<sup>+</sup> taken with only the 1300 nm pump pulse (bottom) and with pump-probe excitation using  $6 \times 10^{12}$  W cm<sup>-2</sup> probe pulses at 800 nm, 650 nm, and 400 nm (top). The pump-only spectrum is dominated by the intact PNT<sup>+</sup> cation at  $m/z$  137, with minor contribution from the C<sub>7</sub>H<sub>7</sub><sup>+</sup> fragment at  $m/z$  91. The greatest depletion in PNT<sup>+</sup> signal was observed at pump-probe delays of +160 fs for 800 nm probe, +200 fs for 650

nm probe, and +60 fs for 400 nm probe. As seen in Figure 5.1a, a substantial depletion in PNT<sup>+</sup> signal and concomitant rise in fragment ion signals occurs at the selected pump-probe delay for each probe wavelength. Whereas both the 800 nm and 650 nm probe wavelengths primarily enhance the yield of C<sub>7</sub>H<sub>7</sub><sup>+</sup> and to a lesser extent C<sub>5</sub>H<sub>5</sub><sup>+</sup> (*m/z* 65), the 400 nm probe enhances only C<sub>5</sub>H<sub>5</sub><sup>+</sup> and C<sub>3</sub>H<sub>3</sub><sup>+</sup> (*m/z* 39). This change in fragmentation pattern with different probe wavelengths indicates that *selective* fragmentation is possible using pump-probe excitation.

Figure 5.1b displays the transient ion signals of the PNT<sup>+</sup>, C<sub>7</sub>H<sub>7</sub><sup>+</sup>, C<sub>5</sub>H<sub>5</sub><sup>+</sup>, and C<sub>3</sub>H<sub>3</sub><sup>+</sup> fragments as a function of pump-probe delay using 800 nm (magenta), 650 nm (orange), and 400 nm (blue) probe wavelengths. Each ion signal is normalized to its respective yield at negative pump-probe delay. The large-amplitude oscillations in the PNT<sup>+</sup> and fragment ion signals with period 420 fs arise from the vibrational wave packet along the C–C–N–O torsional coordinate in PNT<sup>+</sup>, which we previously reported from pump-probe measurements with only 800 nm probe wavelength<sup>4</sup>. The present results show that the 650 nm probe wavelength produces larger-amplitude oscillations in PNT<sup>+</sup> with the same phase, which indicates that 650 nm more effectively excites the PNT<sup>+</sup> torsional wave packet than 800 nm. In contrast, the PNT<sup>+</sup> oscillations with the 400 nm probe have the opposite phase, which indicates 400 nm probe selectively excites the PNT<sup>+</sup> torsional wave packet at a different location on the PES along the torsional coordinate than the lower-energy probe wavelengths. Finally, additional low-amplitude fast oscillations with a period of ~55 fs are observed in the PNT<sup>+</sup> and C<sub>7</sub>H<sub>7</sub><sup>+</sup> signals only for the 800 nm probe. These oscillations were best resolved using a 1500 nm pump wavelength (shown in Figure 5.1b), although they are also visible using a 1300 nm pump wavelength (Appendix B, Figure B2).

To further interpret the oscillatory dynamics, transient ion signals as a function of pump-probe delay,  $\tau$ , were fit to the equation

$$S(\tau) = ae^{-\tau/T_1} \cos\left(\frac{2\pi}{t}\tau + \phi\right) + be^{-\tau/T_2} + c \quad (5.1)$$

where  $a$  and  $b$  are amplitude coefficients,  $t$  is the oscillation period,  $T_1$  is the coherence lifetime,  $T_2$  is a second lifetime not associated with oscillations, and  $c$  is the ion yield as  $\tau \rightarrow \infty$ . Each transient signal at  $\tau \geq 70$  fs (i.e., after the pump pulse is over so the instrument response function can be ignored) was fit to eq (C.1) using nonlinear least-squares

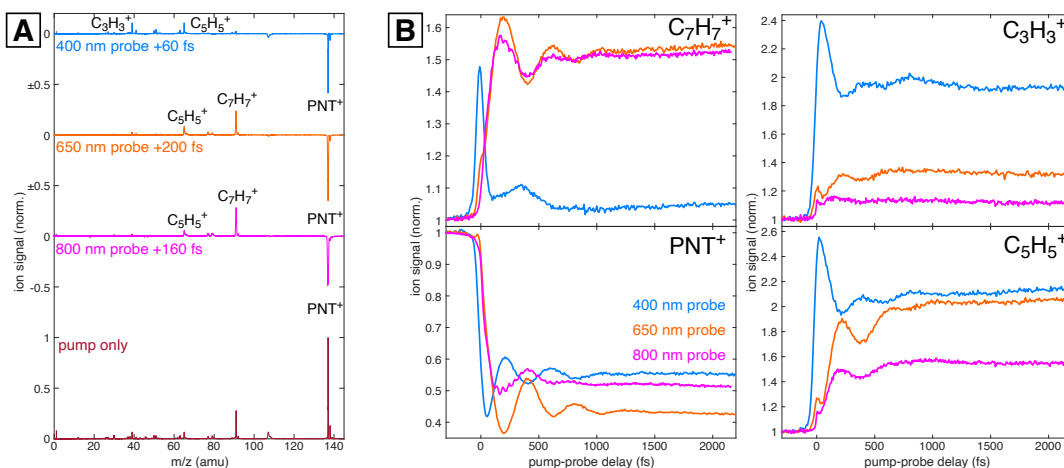


Figure 5.1: (A) Mass spectrum of  $\text{PNT}^+$  taken with 1300 nm pump only (dark red) and the difference spectra relative to the pump-only spectrum taken with 800 nm (magenta), 650 nm (orange), and 400 nm (blue) probe pulses at the indicated delays. (B) Transient ion signals for  $\text{PNT}^+$ ,  $\text{C}_7\text{H}_7^+$ ,  $\text{C}_5\text{H}_5^+$ , and  $\text{C}_3\text{H}_3^+$  taken at each probe wavelength. Each signal is normalized to its yield at negative pump-probe delay.

curve fitting in MATLAB. A full description of the extracted coefficients can be found in Appendix B, Figure B3 and Tables B1–B3. Further analyses need to be performed in order to now the population of cationic ground and excited states produced after ionization with the pump beam but, regardless the particular details, it is reasonable to assume that, when the probe beam arrives after a delay  $\geq 70$  fs, it will find the cation in the ground state after the corresponding electronic relaxation process. The validity of this assertion can be supported with the work of Kraus and coworkers<sup>133</sup> in which charge migration processes were demonstrated for the iodoacetylene cation. The documented phenomena occurs within the scale of less than 5 fs, well below the 70 fs delay used for our analysis. The fit coefficients corresponding to the oscillatory dynamics shown in Table 5.1 confirm both that each fragment ion oscillates  $\pi$  radians out of phase with respect to  $\text{PNT}^+$  and that the phase of the  $\text{PNT}^+$  signal shifts from approximately 0 radians for 650 nm excitation to  $\pi$  radians for 400 nm excitation. The oscillation period is  $\sim 420$  fs for both 650 nm and 400 nm probes, whereas the somewhat longer  $\sim 460$  fs oscillation period using the 800 nm probe arises from a poorer fit quality (see Appendix B, Figure B3).

Subtraction of the incoherent dynamics (second and third terms in eq C.1) allows for clearer visualization of the oscillatory dynamics and frequency analysis via fast Fourier Transform (FFT). Figure 5.2A displays the coherent transient ion dynamics of  $\text{PNT}^+$  and

$\lambda_{probe}$	ion	$a$	$T_1$ (fs)	$t$ (fs)	$\phi$ (rad)
400 nm	PNT <sup>+</sup>	$0.10 \pm 0.01$	$345 \pm 33$	$410 \pm 7$	$3.1 \pm 0.1$
	C <sub>5</sub> H <sub>5</sub> <sup>+</sup>	$0.03 \pm 0.01$	$370 \pm 120$	$421 \pm 20$	$0.3 \pm 0.3$
650 nm	PNT <sup>+</sup>	$0.25 \pm 0.01$	$308 \pm 15$	$425 \pm 4$	$0.05 \pm 0.04$
	C <sub>7</sub> H <sub>7</sub> <sup>+</sup>	$0.15 \pm 0.01$	$290 \pm 12$	$417 \pm 3$	$3.1 \pm 0.03$
	C <sub>5</sub> H <sub>5</sub> <sup>+</sup>	$0.09 \pm 0.01$	$252 \pm 17$	$438 \pm 9$	$3.3 \pm 0.1$
800 nm	PNT <sup>+</sup>	$0.15 \pm 0.02$	$210 \pm 16$	$464 \pm 11$	$0.45 \pm 0.07$
	C <sub>7</sub> H <sub>7</sub> <sup>+</sup>	$0.13 \pm 0.01$	$212 \pm 12$	$438 \pm 7$	$3.3 \pm 0.1$

Table 5.1: Curve fitting coefficients for coherent dynamics of ion signals: oscillation amplitude ( $a$ ), coherent lifetime ( $T_1$ ), oscillation period ( $t$ ), and phase ( $\phi$ ).

oscillatory fragment ions for each probe wavelength. A clear  $\pi$  phase shift in the PNT<sup>+</sup> signals (red) between the 400 nm probe and 650 nm or 800 nm probes is visible, as indicated by the dotted lines at 200, 620, and 1040 fs. Figure 5.2B displays the FFT amplitude of the signals shown in figure 5.2A. For all probe wavelengths the FFT spectra exhibit a strong peak at  $80\text{ cm}^{-1}$  assigned to the previously reported C–N–N–O torsional mode of PNT<sup>+</sup><sup>4</sup>. A closer inspection of the oscillations using the 800 nm probe (bottom panel of Figure 5.2A) reveals what seems to be the superposition of two coherent oscillations: one corresponding to the torsional mode already discussed and smaller amplitude oscillations corresponding to a faster vibrational mode. In line with these observations is the presence of two frequencies, at 80 and  $650\text{ cm}^{-1}$ , in the FFT of the 800 nm probe signal (bottom panel of Figure 5.2B). Additionally, it is worth noting that the superposition of vibrational modes is more evident around the first minimum of the oscillatory ion signal in PNT<sup>+</sup>. This fact will be further discussed in Section 5.3.3 with the aid of computational results.

In order to motivate forthcoming computational results, we present the optimized structures of neutral and cationic PNT at the B3LYP/def2-TZVPP level of theory in Figure 5.3. The corresponding coordinates are available within Appendix B (Tables B4 and B5). Relevant to this work are the following changes after electron detachment: the C–C–N–O dihedral angle goes from 0.1 to 52.7 degrees and a moderate distortion of the ring occurs. Additionally, the frequencies and corresponding intensities of the normal modes for PNT<sup>+</sup> are presented in Appendix B (Table B6). A careful analysis of these vibrational modes shows that the C–C–N–O torsional mode has a calculated frequency of  $58.96\text{ cm}^{-1}$ , in reasonable agreement with the experimental frequency of  $80\text{ cm}^{-1}$  (Figure 5.2B). Figure 5.3B shows the 12th normal mode calculated for the PNT cation. The relevance of this ring-stretching mode will be further discussed in Section 5.3.3. At this moment, it is enough to say that the

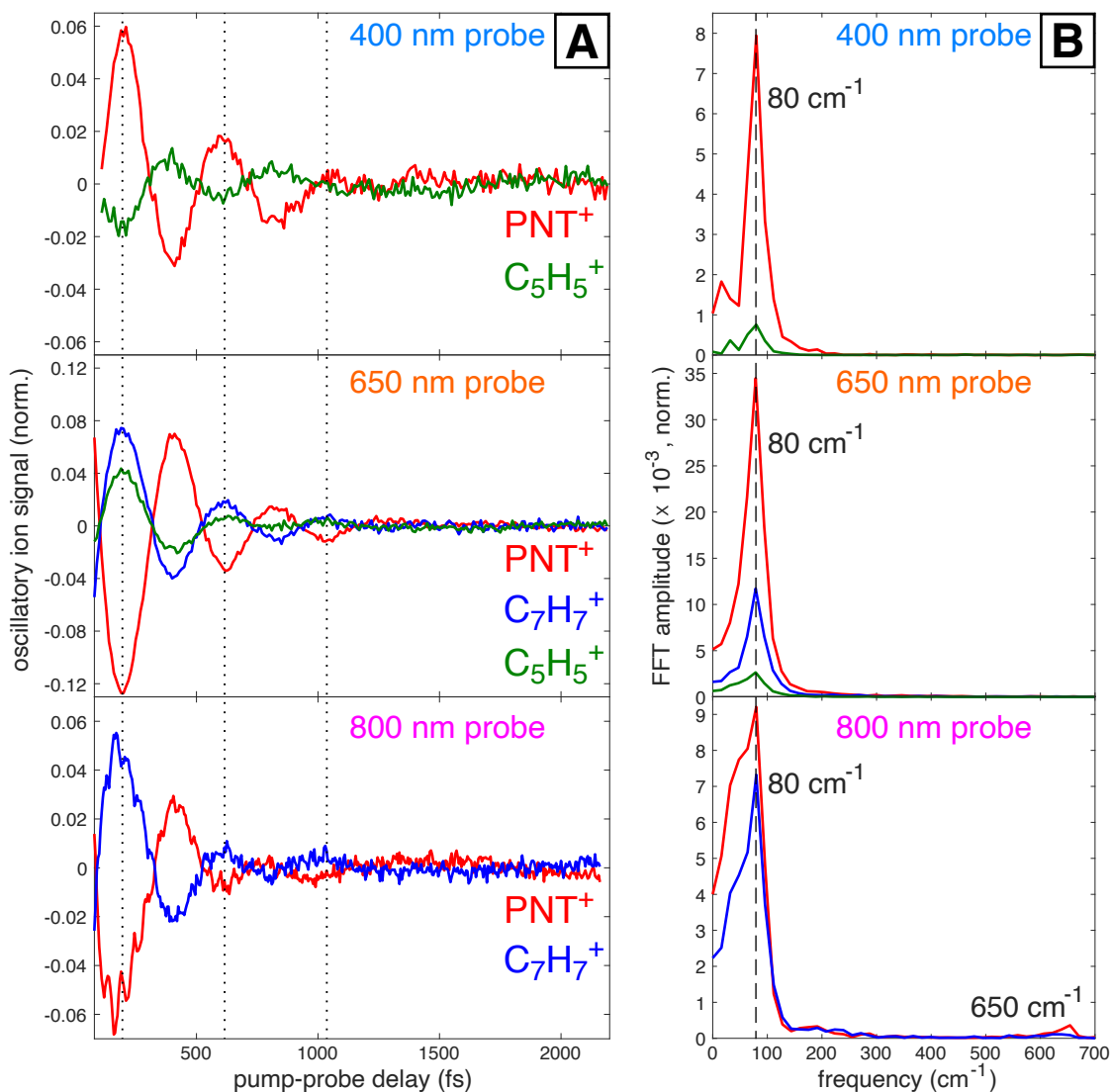


Figure 5.2: (A) Oscillatory ion signals for PNT<sup>+</sup> and selected fragment ions obtained by subtracting off the incoherent contributions to signal fitting via eq C.1. (B) FFT amplitudes obtained from the signals in (A) with indicated frequencies at 80 cm<sup>-1</sup> and 650 cm<sup>-1</sup> (for 800 nm probe).

calculated frequency of 604.32 cm<sup>-1</sup> fairly matches the experimental frequency of 650 cm<sup>-1</sup> shown in Figure 5.2B for the 800 nm probe.

### 5.3.2 Coherent control of torsional wave packet excitation

As mentioned in the previous section, a former work from our group has assigned the main coherent oscillations of PNT<sup>+</sup> to a torsional wave packet involving the C–C–N–O dihedral angle<sup>4</sup>. In order to explain the observation of different fragment distributions and ion yield dynamics depending on the wavelength of the probe beam, we used the following approach:

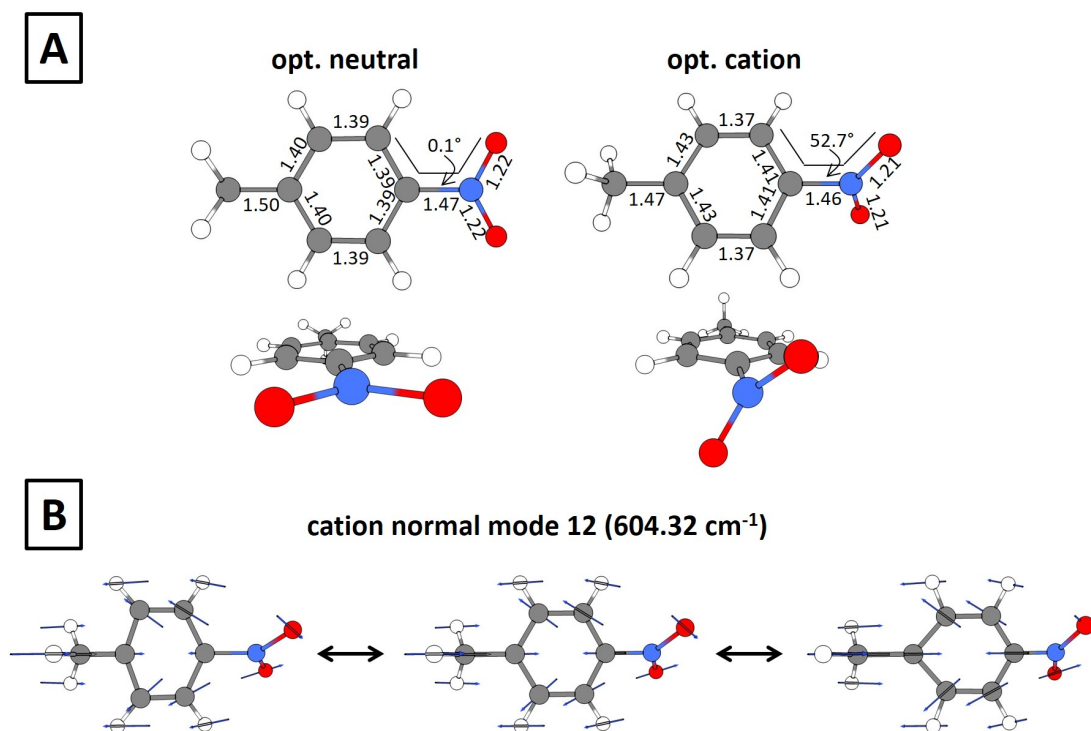


Figure 5.3: (A) Geometrical structures for optimized neutral and cationic PNT. Bond lengths are in Å and torsional angles in degrees. (B) Normal mode at 604.32 cm<sup>-1</sup> for the optimized PNT cation. The calculations were performed at the B3LYP/def2-TZVPP level of theory.

starting from the optimized cation geometry with a C–C–N–O dihedral angle of 52.7° we performed a relaxed scan of this torsional mode using the ModRedundant keyword in Gaussian 16. This procedure generated a collection of geometries that span all the torsional mode, which were used to perform single-point TDDFT calculations. The resulting potential energy surfaces (PESs) can be seen in Figure 5.4A. In line with previous findings on the closely related nitrobenzene cation<sup>51</sup>, we found that the PESs can be classified into two groups: the first one comprising from D<sub>1</sub> to D<sub>4</sub> with all the surfaces showing a marked dependence on the dihedral angle, and a second group comprising from D<sub>5</sub> to D<sub>7</sub> with a less marked dependence on the dihedral angle. The influence of the dihedral angle on the excitation probability, quantified by means of a harmonic estimate of the oscillator strength, can be observed in Figure 5.4B. It is noteworthy that the oscillator strength for the D<sub>0</sub> → D<sub>4</sub> transition ( $f_{04}$ ) is particularly high and dependent on the geometry, reaching its maximum value at 90°. Moreover, this transition is the only one that has a substantial oscillator strength at 90°. Also notable is the parabolic shape of  $f_{06}$  centered at 90° dihedral angle. As a consequence, there is higher probability for the D<sub>0</sub> → D<sub>6</sub> transition at geometries where PNT<sup>+</sup> is nearly planar,

i.e., near the neutral PNT geometry. Figure 5.4A also shows the energies corresponding to 400, 650, and 800 nm photons for comparison (3.1, 1.91, and 1.55 eV respectively). A careful evaluation of all the information contained in Figure 5.4 as a whole reveals that the 400 nm probe can selectively access an allowed transition from  $D_0$  to  $D_6$  at dihedral angles close to  $0^\circ$ , whereas the 650 nm probe can selectively access a strongly allowed transition from  $D_0$  to  $D_4$  at a dihedral angle of  $90^\circ$ . This ability to access different electronic excited states at different locations along the potential energy surface accounts for the selective fragmentation observed with different probe wavelengths at different time delays. Additionally, the 800 nm probe should be capable of promoting the  $D_0 \rightarrow D_n$ ,  $n = 1, 2$  transitions at any dihedral angle.

In order to support our TDDFT calculations we also performed single-point computations at three selected geometries calculated at the B3LYP/def2-TZVPP level using the EOM-EE-CCSD method. The geometries considered were the optimized neutral and cationic species (Figure 5.3a; Appendix B Tables B4 and B5) and the geometry with a dihedral angle of  $87.4^\circ$  obtained by means of the relaxed scan previously described (Table B7 within Appendix B). Table 5.2 shows the excitation energies and harmonic estimates of oscillator strengths calculated at both levels of theory for PNT cation with a C–C–N–O dihedral angle of  $87.4^\circ$ . These methodologies produced qualitatively similar results but there are some differences that are worth noting: EOM calculations introduce larger energetic gap between  $D_1$  and  $D_2$  states of  $\sim 1.2$  eV. Consequently, states  $D_2$ ,  $D_3$ , and  $D_4$  from EOM computations are shifted upwards when compared with TDDFT results. Also, according to the oscillator strength values, EOM method points towards  $D_3$  as the bright state while TDDFT locates the  $D_4$  state as the bright one. Despite this disagreement in the ordering of states, the relevant fact is that both methodologies confirm the presence of an excited state with substantial oscillator strength at  $90^\circ$  dihedral angle and with excitation energy around 2 eV. Possible sources for the disagreement between both levels of theory will be briefly discussed on Section 5.4. Tables B8 and B9 of Appendix B show analogous comparisons between the two methodologies for  $\text{PNT}^+$  at the optimized neutral and cation geometries respectively.

### 5.3.3 Assignment of $650\text{ cm}^{-1}$ wave packet

In Section 5.3.1 we showed experimental evidence of the superposition of two vibrational wave packets and identified the associated frequencies as 80 and  $650\text{ cm}^{-1}$ . The  $80\text{ cm}^{-1}$  has

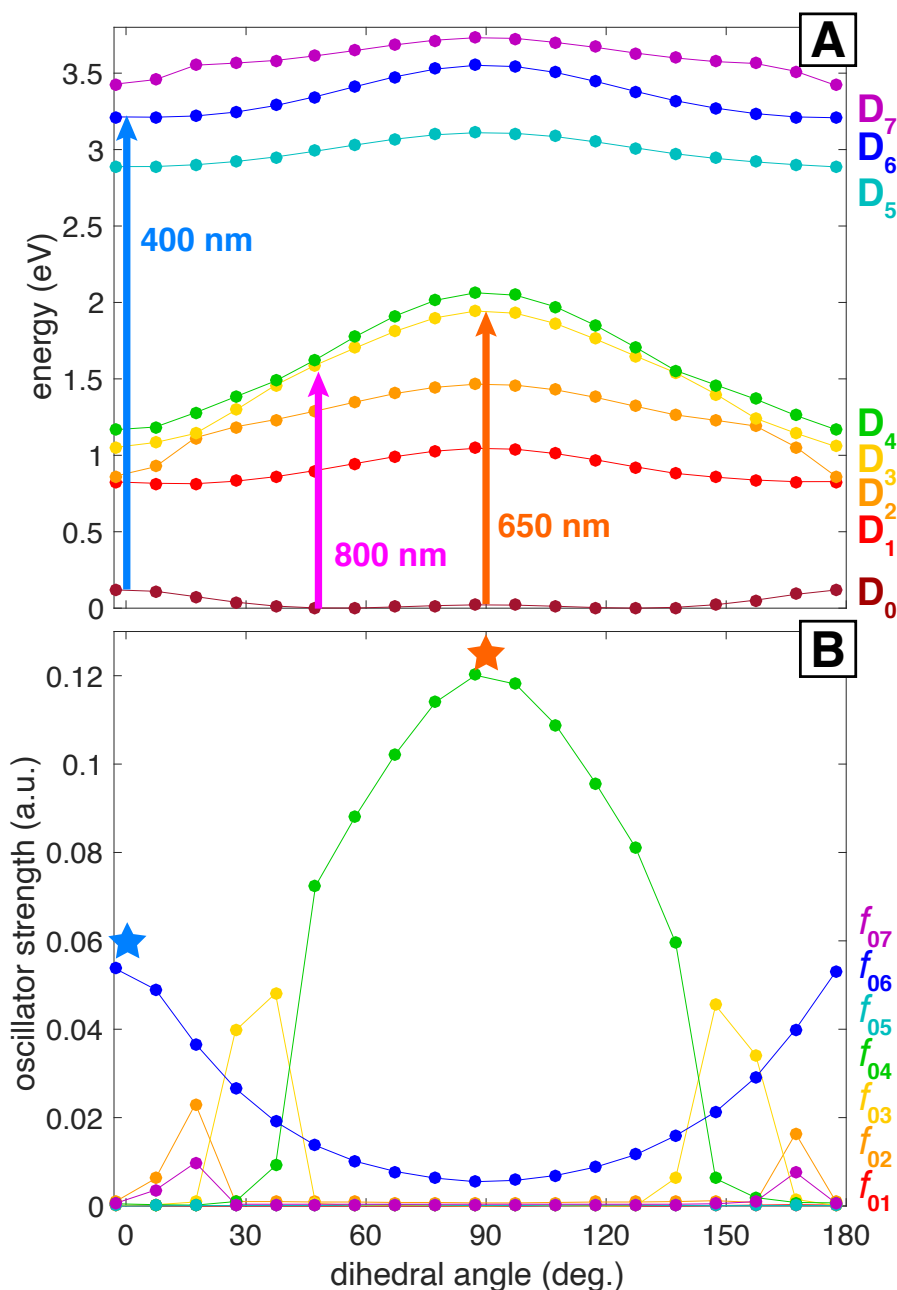


Figure 5.4: Computed potential energy surfaces (A) and oscillator strengths (B) for PNT<sup>+</sup> along the C-C-N-O dihedral angle.

previously been assigned to the C-C-N-O torsional mode but the identity of the vibrational mode associated with the 650 cm<sup>-1</sup> frequency remains to be fully elucidated. The match between the experimental frequency of 650 cm<sup>-1</sup> (Figure 5.2B) and the computationally calculated frequency of 604.32 cm<sup>-1</sup> (Figure 5.3B and Table B6) lays the foundation for the hypothesis that this ring-stretching mode is the one supporting the additional nuclear wave packet found in this work.

transition	B3LYP/ def2-TZVPP		EOM-EE-CCSD/ 6-311+G*	
	EE (eV)	$f$ (a.u.)	EE (eV)	$f$ (a.u.)
$D_0 \rightarrow D_1$	1.02	0.0000	1.12	0.000049
$D_0 \rightarrow D_2$	1.44	0.0007	2.35	0.000654
$D_0 \rightarrow D_3$	1.92	0.0000	2.59	0.132253
$D_0 \rightarrow D_4$	2.04	0.1201	2.87	0.000112
$D_0 \rightarrow D_5$	3.09	0.0001	3.49	0.000003
$D_0 \rightarrow D_6$	3.53	0.0055	3.56	0.000051
$D_0 \rightarrow D_7$	3.71	0.0004	3.84	0.001330

Table 5.2: Excitation energies (EE) and oscillator strengths ( $f$ ) for PNT<sup>+</sup> with a C–C–N–O dihedral angle of 87.4° at the B3LYP/def2-TZVPP and EOM-EE-CCSD/6-311+G\* levels of theory.

In order to test this hypothesis we simulated the superposition of the two vibrational modes by considering three geometries within the torsional mode with 0.1, 52.7, and 87.4 C–C–N–O dihedral angles. Then, from these three geometries we performed frequency calculations to identify the ring-stretching mode in each case. The geometry with 0.1° torsional angle corresponds to the vertical cation, i.e., the cation under the optimized neutral geometry, while the structure with 52.7° dihedral angle corresponds to the optimized cation with a ring-stretching mode at 604.32 cm<sup>-1</sup> (Table B6, Appendix B). Having identified the ring-stretching modes for each of the three geometries we made the additional hypothesis that the  $D_0 \rightarrow D_2$  transition is the one allowing the observation of the ring-stretching wave packet. This hypothesis is supported by our TDDFT calculations showing that 800 nm is nearly resonant with the  $D_0 \rightarrow D_2$  transition at any dihedral angle (Figure 5.4A) and by the experimental fact that the superposition of vibrational wave packets is only observable with 800 nm excitation. With these ideas in mind we took five “snapshots” within each of the three ring-stretching modes and retrieve the corresponding geometries. Those 15 geometries, 5 per each ring-stretching mode, served as the basis for single-point TDDFT calculations to obtain the  $D_0 \rightarrow D_2$  excitation energies and the corresponding harmonic estimates for the oscillator strengths.

The results of these calculations are shown in Figure 5.5. It is important to offer some clarification regarding the abscissa axis of this figure: since the ring-stretching mode involves the collective motion of many atoms as can be seen in Figure 5.3B, the description of the mode in terms of a single parameter is not an easy task. Due to this complication we show the C–N bond distance as a signature of the mode, but it should be kept in mind that

the abscissa axis represents the whole ring-stretching mode, as highlighted in the structures shown in Figure 5.5. This being said, Figure 5.5A shows the excitation energy for the  $D_0 \rightarrow D_2$  transition as a function of the C–N bond distance for three different torsional geometries with 0.1, 52.7, and 87.4 dihedral angles. The figure also shows that 800 nm (1.55 eV) provides enough energy to promote the  $D_0 \rightarrow D_2$  transition for all the C–N bond lengths under all torsional geometries. Additionally, 800 nm is nearly resonant with the excitation energy corresponding to the torsional geometry of 87.4° at all C–N bond distances. This last observation might explain why the superposition of vibrational modes is more evident around the first minimum of  $PNT^+$  and the first maximum of  $C_7H_7^+$  oscillatory ion signals (bottom panel of Figure 5.2A). The reasons behind the association of the minimum in the oscillatory ion signal of  $PNT^+$  with a dihedral angle  $\sim 90^\circ$  are two-fold: first, our TDDFT calculations shows that there is a strong probability of a  $D_0 \rightarrow D_4$  transition as the dihedral angle approaches  $90^\circ$  (Figure 5.4). While it is true that 800 nm excitation is not capable of promoting the  $D_0 \rightarrow D_4$  at all dihedral angles it is also true that it can promote such transition at different torsional angles. The second reason is motivated by a previous work from our group regarding an analogous torsional wave packet within nitrobenzene cation, a cation closely related to  $PNT^+$ . In that work we estimated the time taken for the wave packet to reach a  $90^\circ$  dihedral angle as approximately 200 fs by means of classical wave packet trajectory calculations and pump-probe measurements. This finding is consistent with the maximum depletion of  $PNT^+$  at 160 fs pump-probe delay with 800 nm excitation (the maximum depletion with 650 nm excitation occurs at a delay of 200 fs). Figure 5.5B shows the oscillator strength for the  $D_0 \rightarrow D_2$  transition ( $f_{02}$ ) as a function of the C–N bond under the same torsional geometries as panel A. Here we can observe a sharp increase in  $f_{02}$  at an elongated C–N bond length of 1.54 Å (the equilibrium bond length is 1.46 Å for the optimized cation, Figure 5.3A). This increase is very large for the geometry with 87.4° dihedral angle but it is also visible, although to a lesser extent, for the geometry with dihedral angle of 52.7°. All this facts as a whole strengthen the assignment of the additional wave packet found in this work to the ring-stretching vibrational mode.

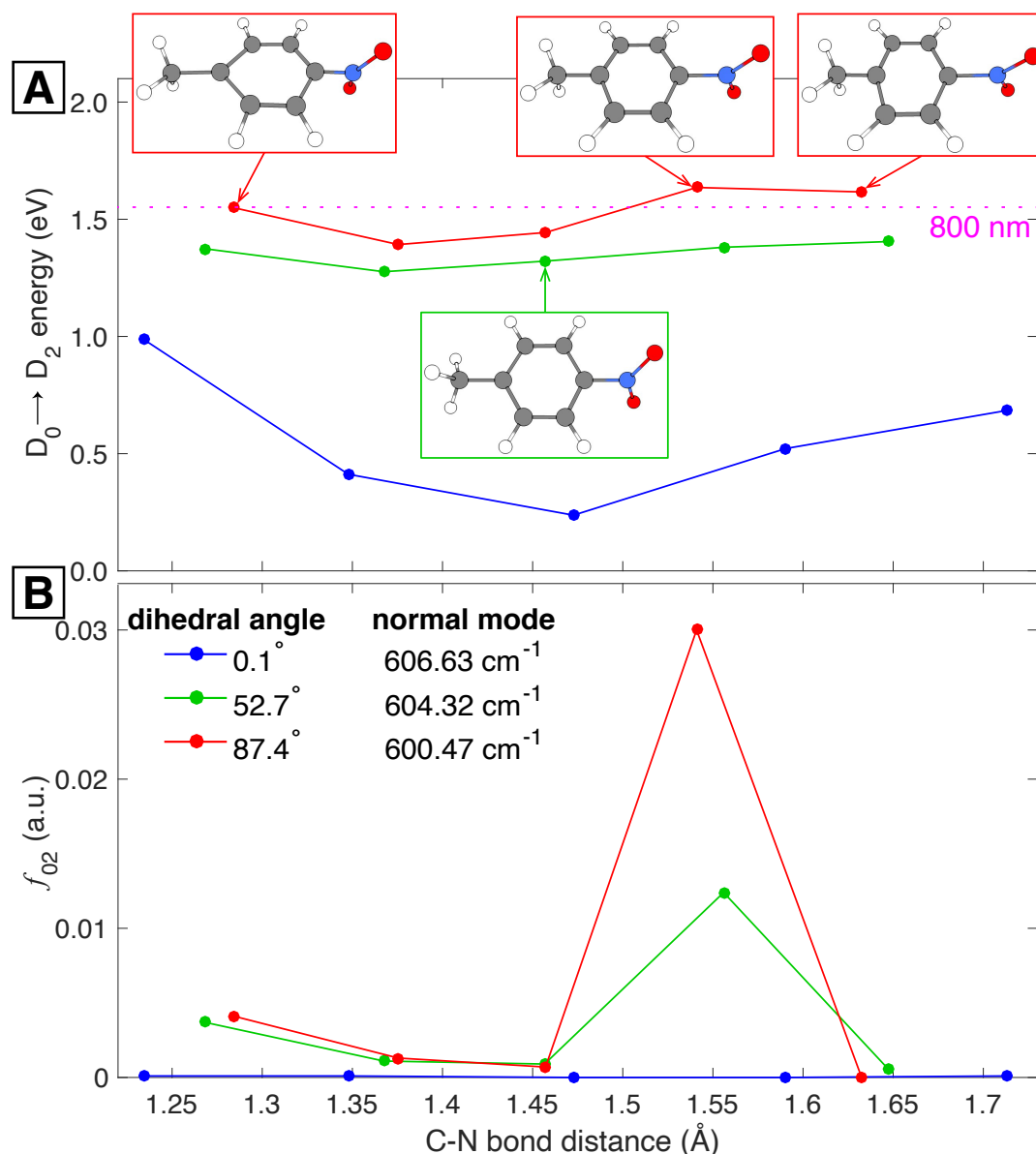


Figure 5.5: Computed potential energy surfaces (A) and oscillator strengths (B) for PNT<sup>+</sup> along C-N bond distance under different C-C-N-O dihedral angles.

## 5.4 Discussion

This study represents the first demonstration of selective excitation to different electronic excited states upon coherent vibrational motion in a large organic cation. The motion of the two nuclear wave packets in PNT<sup>+</sup> produces three distinct transient electronic transitions amenable to optical excitation: (1)  $D_0 \rightarrow D_6$  transition with energy 3.1 eV at C-C-N-O dihedral angle of 0°, (2)  $D_0 \rightarrow D_4$  (or  $D_3$ ) transition with energy 2.0 eV at a 90° dihedral angle, and (3)  $D_0 \rightarrow D_2$  transition with energy 1.6 eV at 90° dihedral angle with elongated

C–N bond length of 1.54 Å. The electronic structure of  $\text{PNT}^+$  along both the torsional and ring-stretching coordinates enables selective excitation to different excited states at specific geometries. The electronic structure was mainly explored by means of TDDFT calculations and further supported at the EOM-CCSD level. The upwards energetic shift observed for the  $D_2$ ,  $D_3$ , and  $D_4$  states at the EOM level when compared with TDDFT results can be rationalized by the small 6-311+G\* basis set being used for EOM computations (in contrast with the def2-TZVPP basis set for TDDFT calculations). Different groups had found that, as the basis set is expanded by adding diffuse and polarization functions, the excitation energies computed at the EOM-CCSD level decrease<sup>134,135</sup>. Therefore, a closer match between the excitation energies predicted by both levels of theory would be expected if a bigger basis set is employed for EOM calculations. Additionally, the discrepancy in which EOM identifies  $D_3$  as the bright state while TDDFT points to  $D_4$  has been previously observed for various systems<sup>51,111–115</sup>. Nevertheless, both levels of theory confirm the presence of an excited state with substantial oscillator strength at 90° dihedral angle and with excitation energy around 2 eV. Overall, we conclude that the computationally inexpensive TDDFT level of theory is adequate enough for aiding and rationalizing the design of pump-probe control schemes.

The finding that 400 nm excitation of  $\text{PNT}^+$  selectively produces  $\text{C}_5\text{H}_5^+$  and  $\text{C}_3\text{H}_3^+$ , whereas 650 nm or 800 nm excitation produces  $\text{C}_7\text{H}_7^+$  (Figure 5.1) indicates that population of the higher-energy  $D_6$  state causes more extensive fragmentation than population of the lower  $D_2 - D_4$  states. This finding is consistent with the reported higher dissociation energy of  $\text{C}_5\text{H}_5^+$  and its formation by further dissociation of  $\text{C}_7\text{H}_7^+$ <sup>136</sup>. We can quantify the selectivity to  $\text{C}_7\text{H}_7^+$ ,  $\text{C}_5\text{H}_5^+$ , or  $\text{C}_3\text{H}_3^+$  formation by examining the fractional yield of a specific target ion relative to the sum of the ion yields,

$$Y = \frac{\text{target ion}}{\text{PNT}^+ + \text{C}_7\text{H}_7^+ + \text{C}_5\text{H}_5^+ + \text{C}_3\text{H}_3^+} \quad (5.2)$$

for each probe wavelength at the pump-probe delay producing the greatest  $\text{PNT}^+$  signal depletion identified in Figure 5.1. The fractional yields for each ion at a series of probe intensities from 2 to 15  $\text{TW cm}^{-2}$  are shown in Figure 5.6. Although greater enhancement of fragment ion yields is observed at higher probe intensities, 15  $\text{TW cm}^{-2}$  represents a practical upper limit because at higher intensity the probe pulse creates ions even in the absence of the pump pulse. Examination of Figure 5.6 shows that  $\text{C}_7\text{H}_7^+$  is selectively enhanced

using 650 nm and 800 nm, whereas  $C_3H_3^+$  is selectively enhanced using 400 nm. Hence, we can conclude that population of  $D_2 - D_4$  selectively produces  $C_7H_7^+$  whereas population of  $D_6$  selectively produces  $C_3H_3^+$ . Although the  $C_5H_5^+$  yield is most enhanced by 400 nm excitation, its weaker dependence on the probe wavelength suggests that it can be formed by excitation to any of the excited states and is therefore less amenable to selective enhancement with pump-probe control. Overall, pump-probe excitation is found to enable a similar degree of control over the  $C_7H_7^+/C_3H_3^+$  ion ratios as attained using shaped 800 nm pulses<sup>126</sup>: the maximum  $C_7H_7^+/C_3H_3^+$  ratio of 5.6 attained with 800 nm, 5 TW cm<sup>-2</sup> probe pulses is 40% higher than the maximum ratio of  $\sim 4$  obtained with transform-limited 800 nm pulses, although the minimum ratio of 0.8 attained with 400 nm, 15 TW cm<sup>-2</sup> is somewhat higher than the minimum ratio of  $\sim 0.2$  reported with pulse shaping.

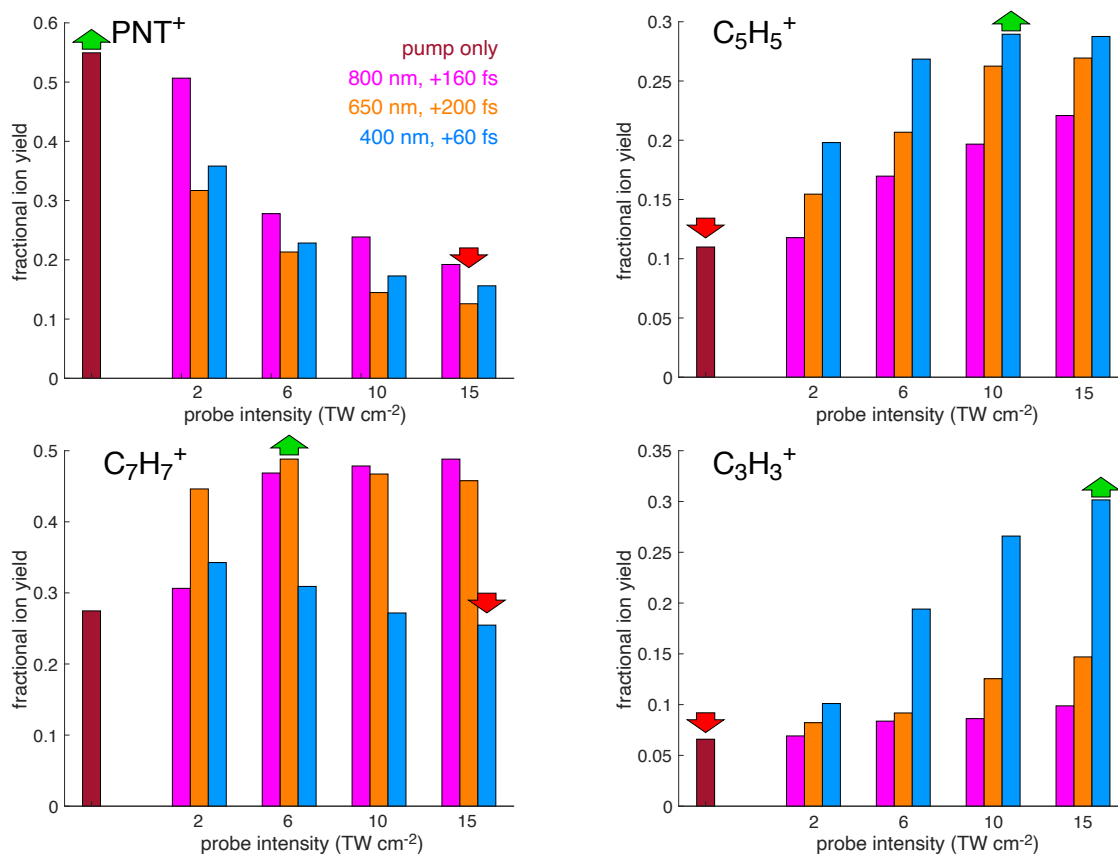


Figure 5.6: Fractional yields of  $PNT^+$ ,  $C_7H_7^+$ ,  $C_5H_5^+$ , and  $C_3H_3^+$  from eq 5.2 obtained using 800 nm, 650 nm, and 400 nm probe wavelengths at intensities from 2 – 15 TW cm<sup>-2</sup>.

Finally, the observation that strong field ionization of PNT launches nuclear wave packets along two distinct vibrational modes is of particular interest. Numerous previous pump-probe

studies of other substituted benzenes including nitrobenzene<sup>51</sup>, *o*-nitrotoluene<sup>77</sup>, azobenzene<sup>75</sup> and alkyl phenyl ketones<sup>70–72</sup> have observed only torsional wave packet motion upon strong-field ionization. To the best of our knowledge, the only previous study to definitively observe multimode coherent vibrational motion in a cation prepared by strong field ionization found a superposition of the C–I stretch and I–CH<sub>3</sub> umbrella modes in CH<sub>3</sub>I<sup>+</sup><sup>137</sup>. Although in a previous work we had proposed multimode coherent excitation in diisopropyl methylphosphonate ion to explain observed ion yield oscillations at two different frequencies<sup>74</sup>, no PES calculations were performed to confirm distinct excitation pathways. Hence, we recommend the combined strategy of pump-probe measurements with multiple probe wavelength and PES computations along possible coherently excited coordinates as performed in this work to identify possible multimode coherent excitation in other organic cations prepared by strong-field ionization.

## Chapter 6

# Photodissociation dynamics of the unusually stable ONA Cation

This chapter shows work in progress.

### 6.1 Introduction

The high explosive 1,3,5-triamino-2,4,6-trinitrobenzene (TATB) is exceptionally insensitive to accidental thermal and shock initiation, making TATB widely applicable for both defense and civilian purposes.<sup>138</sup> The unexpected insensitivity of TATB has been attributed to strong hydrogen bonding<sup>139,140</sup>,  $\pi$ -stacking interactions<sup>141</sup>, and cooperativity between these phenomena<sup>142</sup>. In particular, the intramolecular hydrogen bonding between the *ortho* nitro and amino groups in the TATB molecule contributes to its stability to thermal bond dissociation.<sup>143</sup> Excitation with UV light, in contrast, has long been known to induce photochemical reactions in TATB<sup>144–147</sup>.

*Ortho*-nitroaniline (ONA) can model the photochemistry of TATB because it possesses strong intramolecular hydrogen bonding interactions and undergoes the same three initial reaction pathways as TATB upon UV excitation (Figure 6.1). First, intramolecular hydrogen transfer from the amino to nitro group in ONA is observed in photoionization mass spectrometry with 266 nm excitation<sup>148</sup> and matrix-isolation with 185 nm excitation.<sup>149</sup> In TATB, this pathway produces benzofurazan derivatives by elimination of water from the *aci*-nitro tautomer.<sup>150,151</sup> Second, nitro-nitrite rearrangement (NNR) and subsequent NO loss is observed in photoionization mass spectrometry of ONA<sup>148</sup> and produces the stable TATB radical photoproduct observed with ESR and optical spectroscopy<sup>146,147</sup>. Finally, direct NO<sub>2</sub> loss is

observed in photoionization mass spectrometry of ONA<sup>148</sup> and by X-ray photoelectron spectroscopy of TATB.<sup>144</sup>

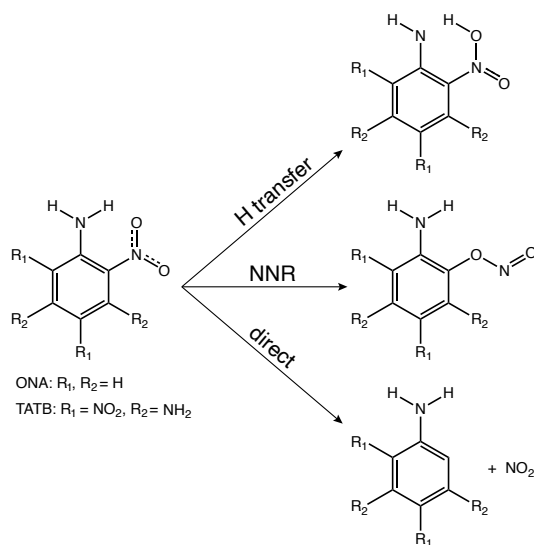


Figure 6.1: Initial photochemical reaction pathways of ONA and TATB.

In addition to electronic excitation, shock initiation of energetic materials induces ionization,<sup>52,152,153</sup> making the reactions of ionized energetic molecules important to understanding their initial decomposition pathways. However, despite extensive computational investigations of the reaction pathways in Figure 6.1 for neutral TATB,<sup>147,150,154,155</sup> analogous reactions in the cations of TATB or ONA have not been explored to the best of our knowledge. The parent cations of both ONA and TATB are relatively stable to dissociation upon electron impact ionization, unlike the related molecules *ortho*-nitrotoluene and trinitrotoluene (TNT), which exhibit extensive dissociation.<sup>1</sup> Hence, it stands to reason that the strong intramolecular hydrogen bonding between nitro and amino groups that stabilizes neutral TATB<sup>143</sup> also contributes to the stability of TATB and ONA cations.

To gain insight into how adjacent nitro and amino groups stabilize molecular cations, this work presents a combined computational and femtosecond time-resolved mass spectrometry (FTRMS) study of ONA. FTRMS, also called “ultrafast disruptive probing”,<sup>156</sup> is a pump-probe method wherein the dynamics of multiple dissociation reactions of molecular cations can be tracked simultaneously on femtosecond – picosecond timescales. Our group has recently reported on the dissociation dynamics of nitrobenzene and nitrotoluene cations with FTRMS, which undergo coherent vibrational excitation upon ionization and readily dissociate upon excitation with low-energy (<2 eV) photons.<sup>4,51,77,116</sup> In the present work we find

that ONA cation requires a higher photon energy (3.1 eV) for dissociation and exhibits no coherent vibrational dynamics. The observed dissociation dynamics in ONA cation are rationalized with detailed calculations of the electronic potential energy surfaces and reaction pathways.

## 6.2 Methods

### 6.2.1 Experiment

The full experimental set up has been described in detail previously.<sup>116</sup> Briefly, a commercial Ti:sapphire regenerative amplifier (Astrella, Coherent, Inc.) producing 30 fs, 800 nm, 2.2 mJ pulses is used to pump an optical parametric amplifier (TOPAS Prime) to produce 20 fs, 1300 nm pulses. Ultrafast disruptive probing was conducted using three different wavelengths at 400 nm, 650 nm, and 800 nm whose experimental details have also been described previously.<sup>4,77,116</sup> In order to electronically excite the ionized species without creating ions on its own, the probe pulses were kept at an intensity of  $8 \times 10^{12} \text{ W cm}^{-2}$  across all three wavelengths. Both the pump and probe pulses were focused with an  $f = 20 \text{ cm}$  fused silica lens into the extraction region of our linear time-of-flight (TOF) mass spectrometer with linear polarization of the laser electric field parallel to the TOF axis. ONA was introduced via an effusive inlet into the vacuum chamber and mass spectra were averaged with a 1 GHz digital oscilloscope (LeCroy Waverunner 610Zi).

### 6.2.2 Theory

Our density functional theory (DFT) calculations of neutral and cationic ONA were conducted using Q-Chem 5.3 software<sup>132,157</sup> employing the restricted Kohn-Sham formalism for neutral species and the unrestricted formalism for cationic species. After performing an initial optimization using the BPW91/6-311G\* level of theory,<sup>95,96</sup> further optimizations under different levels were done along with the corresponding frequency calculations to verify the presence of true minima. Then, adiabatic and vertical ionization energies were calculated. Table 6.1 shows the results of these calculations for the levels of theory considered as well as experimental values from literature. A comparison between the computed and the experimental quantities shows that the values calculated using the Def2TZVPP basis set<sup>100</sup> seem

to be underestimating ionization energy. Therefore, calculations using this basis set were not further considered.

method	IE <sub>ad</sub> (eV)	IE <sub>vert</sub> (eV)
B3LYP/6-311+G*	8.26	8.39
B3LYP/Def2TZVPP	8.20	8.33
CAM-B3LYP/6-311+G*	8.30	8.45
CAM-B3LYP/Def2TZVPP	8.23	8.39
$\omega$ B97XD/6-311+G*	8.25	8.41
$\omega$ B97XD/Def2TZVPP	8.19	8.34
Expt.	8.27 <sup>a</sup>	8.43 <sup>b</sup>

Table 6.1: Calculated adiabatic and vertical ionization energies for ONA and comparison to experimental values in literature. <sup>a</sup> Ref. <sup>1</sup> <sup>b</sup> Ref. <sup>2</sup>

Considering only the results obtained using the 6-311+G\* basis set,<sup>96</sup> we can see that the three functionals (B3LYP,<sup>40,42</sup> CAM-B3LYP,<sup>45</sup> and  $\omega$ B97XD<sup>46</sup>) estimate the experimental ionization energy within 0.03 and 0.04 eV for IE<sub>ad</sub> and IE<sub>vert</sub> respectively, which can be considered as reasonable. The reason for picking the long-range corrected CAM-B3LYP functional over the other two is that it was the only one capable of preserving the structural integrity of the ONA NNR cation that should be formed at some point as demonstrated by the presence of the C<sub>6</sub>H<sub>6</sub>NO<sup>+</sup> fragment in our FTRMS experiments (see Section 6.3.2).

Figure 6.2 shows the optimized structures of ONA neutral and cation species (the corresponding cartesian coordinates can be found in the Appendix C, Tables C1 and C2). Previous studies by our group showed that 2-nitrotoluene, a closely related molecule to ONA, went from a C–NO<sub>2</sub> torsional angle of 26.0 to 35.5° when going from neutral to cation.<sup>77</sup> Other previous results also show changes in the C–NO<sub>2</sub> torsional angle from zero to 57.9° in nitrobenzene<sup>51</sup> and from zero to 52.5° in 4-nitrotoluene<sup>4</sup> when going from neutral to cation. Therefore, an analogous departure from planarity after ionization was expected for ONA. Contrary to the expected, the nitro group in ONA cation remained planar. A hypothetical explanation for this behavior is the presence of an intramolecular hydrogen bond between the nitro and amino groups making the rotation energetically unfavorable (the hypothetical hydrogen bond is shown in Figure 6.2).

The possibility of having low-energy conformers for the rearranged species, intermediates, and fragments involved in this work was carefully evaluated. In this regard, ground-state conformational ensembles were generated using the conformer-rotamer ensemble sampling tool (CREST) version 2.11.1 developed by the Grimme group.<sup>158,159</sup> CREST was developed

as a utility and driver program for the semiempirical quantum chemistry package xtb also developed by the Grimme group. The xtb version employed in this work is 6.4.1. CREST uses an iterative meta-dynamics genetic structure crossing (iMTD-GC) workflow with geometry optimization at the GFN2 level, this later method falls into the semiempirical extended tight-binding (xTB) family of methods.<sup>160</sup> The energetic threshold considered for the generation of the conformational ensembles was 1 kcal/mol for most of the species except for the conformers of the *aci*-rearranged ONA<sup>+</sup>, for which a threshold of 20 kcal/mol was considered (see further discussion of this in Section 6.3.4). Then, the obtained conformers were reoptimized at the CAM-B3LYP/6-311+G\* level and in all cases the lowest energy conformer was considered in further calculations.

The search for transition states started with the use of the freezing string method<sup>161</sup> or the relaxed scan of a carefully selected degree of freedom. This produced a guess for the transition state (TS) that then was optimized. A frequency calculation of the optimized structure was performed to verify that it only possessed a single imaginary frequency. This guaranteed the finding of a first-order saddle point on the potential energy surface (PES) but, in order to confirm that this TS is the one actually joining the species of interest, an intrinsic reaction coordinate (IRC) calculation was performed.<sup>162,163</sup>

The energies and oscillator strengths for transitions to electronic excited states in neutral and cationic ONA were performed by equation-of-motion coupled-cluster with single and double excitations (EOM-CCSD)<sup>103,164</sup> in Q-Chem 5.3 and using time-dependent DFT (TDDFT)<sup>106,165</sup> as implemented in Gaussian 16.<sup>166</sup> The TDDFT calculations used the CAM-B3LYP functional with the 6-311+G\* basis, that same basis set was used for EOM-CCSD calculations.

Ab initio molecular dynamics (AIMD), more specifically Born-Oppenheimer molecular dynamics (BOMD), were used in this work at the CAM-B3LYP/6-31G(d) level as implemented in Q-Chem 5.3. The smaller basis set was employed because of computational efficiency reasons. AIMD simulations in the microcanonical (NVE) ensemble with 0.1 fs time steps and 500 fs duration were performed to determine the time required for the relaxation of the ONA cation from the vertical to the optimized geometry. In BOMD calculations, the energies and gradients were calculated at each time step via DFT, where the initial nuclear velocities were propagated from frequency calculations to put zero-point vibrational energy into each normal mode. No excess energy was provided to begin these trajectories.

## 6.3 Results and Discussion

### 6.3.1 Electronic structure of ONA and $\text{ONA}^+$

Both ONA ( $S_0$  geometry) and  $\text{ONA}^+$  ( $D_0$  geometry) are planar, with the nitro and amino groups in the plane of the benzene ring. As seen in the optimized  $S_0$  and  $D_0$  structures in Figure 6.2a and in agreement with literature,<sup>167</sup> ionization induces only minor changes in the C–N and C–C bond lengths. As a result, the difference between vertical and adiabatic ionization energies is only 0.159 eV and small shifts in the excited state energies are observed in Figure 6.2b. The coupling from the ground  $D_0$  to excited states in ONA cation (Figure 6.2c) shows a strong  $D_0 \rightarrow D_5$  transition and weaker  $D_0 \rightarrow D_1$  transition at both  $S_0$  and  $D_0$  geometries. For reference, the approximate spectra of the 800 nm, 650 nm, and 400 nm probe pulses are shown. 800 nm and 650 nm can access the  $D_1$  state, whereas 400 nm has nearly enough energy to access the  $D_5$  state. We note that the excited state energies of ONA and  $\text{ONA}^+$  calculated at the TD/CAM-B3LYP level generally agree with the EOM-CCSD energies to within 0.4 eV for each level and identify the same strongly coupled states (Appendix C, Tables C3–C5). Although no calculations of ONA cation excited states have been reported to the best of our knowledge, our calculated energy for the neutral ONA  $S_1$  state of 3.79 eV at the TD/CAM-B3LYP level is reasonably close to literature values for the  $S_1$  energy of TATB (3.63 eV at the TD-B3LYP/6-311++G(d,p) level)<sup>147</sup> and ONA (3.06 eV at the same level in water).<sup>168</sup>

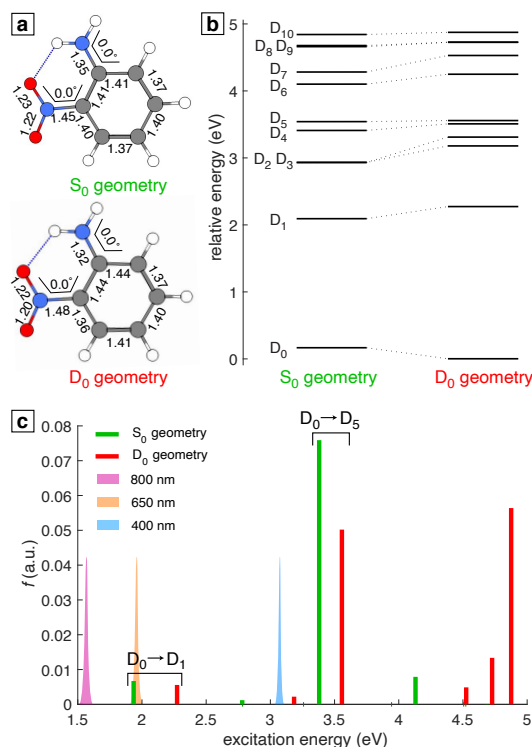


Figure 6.2: (a) Geometric structures of ONA at the  $S_0$  and  $D_0$  geometries calculated at the CAM-B3LYP/6-311+G\* level. (b) Electronic excited states of  $ONA^+$  at the  $S_0$  and  $D_0$  geometries calculated at the EOM-CCSD/6-311+G\* level. (c) Oscillator strengths of transitions out of  $D_0$  for  $ONA^+$  at the  $S_0$  and  $D_0$  geometries, with approximate spectra of the probe wavelengths in FTRMS.

The results in Figure 6.2 show that ONA behaves quite differently from related nitroaromatic molecules. Whereas in nitrobenzene, *ortho*-nitrotoluene, and *para*-nitrotoluene the nitro group rotates out of plane upon ionization,<sup>4,51,77,116</sup> the ONA cation remains planar due to the strong hydrogen bond between the nitro and amino groups. Moreover, nitrobenzene<sup>51</sup> and *para*-nitrotoluene<sup>116</sup> have strong coupling to an excited state  $\sim 2$  eV above  $D_0$ , but the strongly coupled  $D_5$  state in ONA is approximately 3.5 eV above  $D_0$ . These differences suggest that ONA will exhibit different dissociation dynamics from other nitroaromatic cations, prompting the FTRMS investigations presented below.

### 6.3.2 FTRMS measurements

Figure 6.3 shows the mass spectrum of ONA taken with only the 1300 nm pump (top) and difference spectrum obtained with addition of the 400 nm probe at 100 fs delay (bottom). The most intense signals in the pump-only spectrum were the parent  $ONA^+$  and dication  $ONA^{2+}$ , indicating that ONA undergoes significantly less fragmentation than the related

nitrobenzene<sup>51</sup> and nitrotoluenes.<sup>4,77,116</sup> Moreover, the stability of intact  $\text{ONA}^{2+}$  contrasts with 4-nitrotoluene dication, which undergoes Coulomb explosion to form  $\text{NO}_2^+$  and  $\text{C}_7\text{H}_7^+$  within 200 fs.<sup>169</sup> ONA, however, is less stable than aniline, which is observed as an intact trication under similar ionization conditions.<sup>92,170</sup> Hence, the addition of the nitro group to ONA destabilizes the molecule when compared to aniline, but the amino group imparts more stability to the nitro-substituted molecule than the methyl group of the nitrotoluenes due to stronger hydrogen bonding.

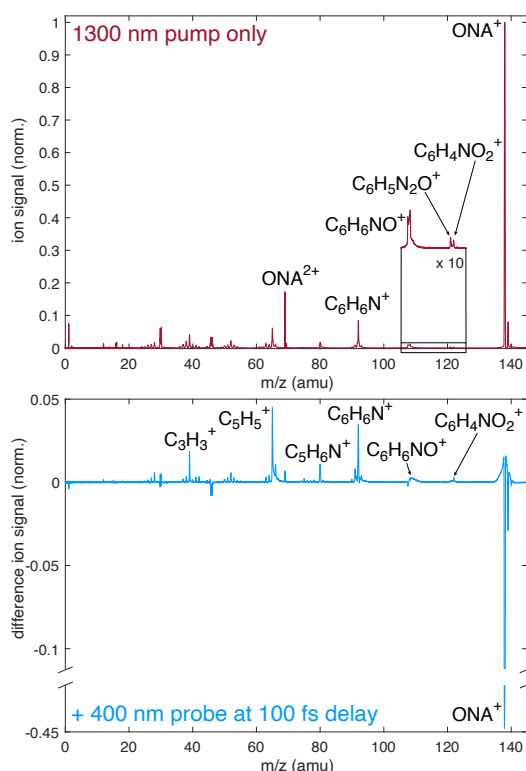


Figure 6.3: Mass spectrum of ONA taken with 1300 nm pump only (top) and difference spectra relative to the pump only spectrum taken with a 400 nm probe pulse at 100 fs delay (bottom).

Of the known fragmentation pathways from Figure 6.1, only the direct pathway to form  $\text{C}_6\text{H}_6\text{N}^+$  contributes significantly under pump-only conditions. The NNR and H transfer pathways have a very low probability of occurring because the  $\text{C}_6\text{H}_6\text{NO}^+$  and  $\text{C}_6\text{H}_5\text{N}_2\text{O}^+$  signals must be magnified to be seen at all (Figure 6.3, top). When the 400 nm probe is added at 100 fs delay, depletion of  $\text{ONA}^+$  and enhancement of fragment ions are observed (Figure 6.3, bottom). The greatest enhancement occurs for the direct fragmentation product  $\text{C}_6\text{H}_6\text{N}^+$  and its sequential fragmentation products and  $\text{C}_3\text{H}_3^+$ . Enhancement of the NNR products  $\text{C}_6\text{H}_6\text{NO}^+$  and  $\text{C}_5\text{H}_6\text{N}^+$ , as well as the H transfer products  $\text{C}_6\text{H}_5\text{N}_2\text{O}^+$  and  $\text{C}_6\text{H}_5\text{N}^+$

(the small peak next to  $\text{C}_6\text{H}_6\text{N}^+$ ) is observed to a smaller degree. The enhancement of these fragmentation pathways is consistent with the 400 nm probe pulse inducing excitation from the  $\text{D}_0$  to  $\text{D}_5$  state, as predicted in Figure 6.2.

Figure 6.4 depicts the FTRMS transient ion signals obtained with 400 nm probing for the species highlighted in Figure 6.3. Signals are normalized to the  $\text{ONA}^+$  yield and then shifted to a value of unity on the ordinate axis at -500 fs delay in each panel. At negative delays (400 nm excitation followed by 1300 nm ionization), the  $\text{ONA}^+$  signal is enhanced relative to the cross-correlation signal from  $\text{H}_2\text{O}^+$  (inset, bottom panel of Figure 6.4). This enhancement is attributed to excitation from  $\text{S}_0$  to  $\text{S}_1$ , which was observed in earlier literature on TATB<sup>171</sup> and is consistent with a predicted allowed transition in ONA according to our computations (Appendix C, Table C3). At positive delays,  $\text{ONA}^+$  undergoes transient depletion for the first 200 fs, followed by partial recovery of the signal over the next 200 fs to reach a constant depleted yield. This transient depletion is mirrored in transient enhancement of the fragment ion signals from each pathway, with the exception that the product of OH loss from H transfer,  $\text{C}_6\text{H}_5\text{N}_2\text{O}^+$  exhibits a sudden enhancement and no further dynamics (Figure 6.4, top). We note that the transient dynamics in Figure 6.4 were only observed using 400 nm as the probe wavelength; excitation with 650 nm or 800 nm resulted in negligible  $\text{ONA}^+$  depletion and fragment ion enhancement (Appendix C, Figure C1). These results indicate that excitation to  $\text{D}_5$  is necessary to induce dissociation of  $\text{ONA}^+$  because 650 nm and 800 nm photons can only access the  $\text{D}_1$  state (Figure 6.2c).

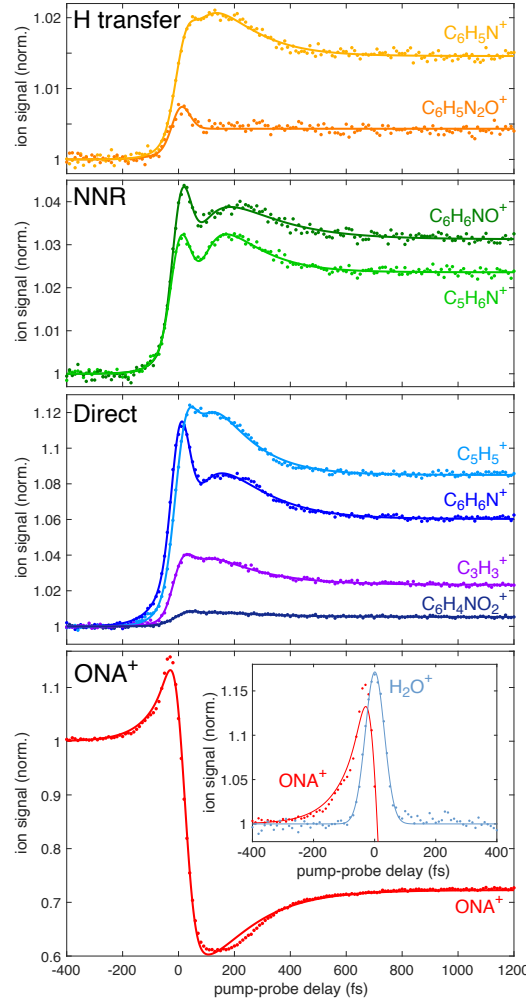


Figure 6.4: Transient ion dynamics of  $ONA^+$  with inset water cross correlation signal, and fragments from the direct pathway (blue/magenta), NNR pathway (green), and H transfer pathway (yellow/orange). The black dots are data points and solid lines are fits to eq (C6)

To quantify the transient dynamics in Figure 6.4, the ion signals were fit using the method introduced by Jochim et al<sup>156</sup>

$$S(\tau) = ae^{-\tau^2/s^2} + bP(\tau, T_1) + cP(\tau, T_2) + d(1 + \operatorname{erf}\left(\frac{\tau}{s}\right)) + 1 + nP(\tau, T_{\text{neg}}) \quad (6.1)$$

where  $\tau$  is the pump-probe delay and  $s = 42.5$  fs is obtained from the width of the cross-correlation function for  $H_2O^+$  seen in the inset of Figure 6.4. The first term in eq (C6) represents the instrument response function from the cross-correlation signal. The terms  $P(\tau, T_i)$ ,  $i = 1, 2$  are given by

$$P(\tau, T_i) = \left[ 1 + \operatorname{erf}\left(\frac{\tau}{s} - \frac{s}{2T_i}\right) \right] e^{-\tau/T_i} \quad (6.2)$$

$T_1$  and  $T_2$  are associated with dynamics at positive delay (i.e., dynamics corresponding to excitation of the ONA cation for  $\tau > 0$ ). The fourth term in eq (C6) accounts for constant depletion or enhancement of the ion signal as  $\tau \rightarrow \infty$  relative to its yield at negative delay. The term  $P(\tau, T_{\text{neg}})$  is given by

$$P(\tau, T_{\text{neg}}) = \left[ 1 - \text{erf} \left( \frac{\tau}{s} - \frac{s}{2T_{\text{neg}}} \right) \right] e^{\tau/T_{\text{neg}}} \quad (6.3)$$

and represents dynamics at negative delay (i.e., dynamics of ONA in the neutral  $S_1$  state at  $\tau < 0$ ). All coefficients and time constants in eq (C6) are determined by least squares curve fitting for each transient ion signal shown in Figure 6.4 and given in the Appendix C, Tables C6 and C7.

All ion signals have similar extracted time constants in the ranges  $T_{\text{neg}} \sim 40 - 75$  fs,  $T_1 \sim 30 - 75$  fs, and  $T_2 \sim 120 - 200$  fs. The observation of similar  $T_{\text{neg}}$  values for each ion is consistent with the slight enhancement of all signals at negative delay arising from ionization out of the short-lived  $S_1$  state. The short  $T_1$  and  $T_2$  values suggest that the dynamics at positive delay may be associated with the relaxation of  $\text{ONA}^+$  from the  $S_0$  to  $D_0$  geometry. This claim is further supported by the computational results in Figure 6.2c indicating that excitation from  $D_0$  to  $D_5$  is more efficient at the  $S_0$  geometry than the  $D_0$  geometry, consistent with the transient depletion of  $\text{ONA}^+$  and enhancement of the fragment ions in the first several hundred femtoseconds after ionization. Finally, the poor fit quality of the  $\text{ONA}^+$  signal (red curve) may arise from the slight variation of  $T_1$  values across the direct pathway fragments: 75 fs for  $\text{C}_6\text{H}_6\text{N}^+$ , 49 fs for  $\text{C}_5\text{H}_5^+$ , and 41 fs for  $\text{C}_3\text{H}_3^+$ . Potential reasons for this  $T_1$  variation and other features seen in Figure 6.4 will be discussed with the aid of pathway calculations presented below.

### 6.3.3 Molecular dynamics simulations

As mentioned in Section 6.3.2,  $\text{ONA}^+$  undergoes transient depletion for the first 200 fs, followed by partial recovery of the signal to reach a constant depleted yield. This experimental fact along with the computational result of an appreciable change in the oscillator strength for the  $D_0$  to  $D_5$  transition depending on  $\text{ONA}^+$  having the vertical ( $S_0$ ) or relaxed ( $D_0$ ) geometry (Figure 6.2c), lead to the hypothesis that this transient behavior observed during the first 200 fs could be related with the time it takes to  $\text{ONA}^+$  for going from the  $S_0$  to the  $D_0$  geometry.

In order to test this hypothesis, we performed AIMD simulations of this process. To facilitate the following discussion, we present Figure 6.5 showing the indices for the different atoms within ONA<sup>+</sup>.

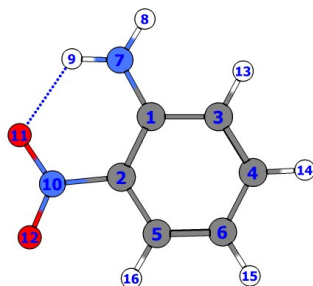


Figure 6.5: ONA<sup>+</sup> under the S<sub>0</sub> geometry. The atoms show the corresponding labeling.

Figure 6.6 shows the evolution of the C2-C5 bond length (see Figure 6.5 for the atom numbering) along one sample AIMD trajectory out of the 18 trajectories that have been run so far (solid black line). The red and blue solid lines represent the upper and lower envelopes of the trajectory as the magnitude of its analytic signal. The analytic signal of the trajectory is found using the discrete Fourier transform as implemented in the *hilbert* function of MATLAB. The trajectory shows an oscillatory behaviour that is strongly damped in regions around the "equilibrium value", the C2-C5 equilibrium bond length in this particular case. We use the slightly vague term equilibrium value because this kind of behaviour is present in all the degrees of freedom no matter if they were bond lengths, angles, or dihedrals. In view of this, we defined a metric based on what can be called the root-square error (RSE) of the upper envelope (upper) with respect to the equilibrium value (EV) ( $\text{RSE} = \sqrt{(\text{upper} - \text{EV})^2}$ ). This produced an array of values and by taking the minimum within this array we could determine the corresponding time. This time was taken as the time necessary to reach the equilibrium value within each trajectory.

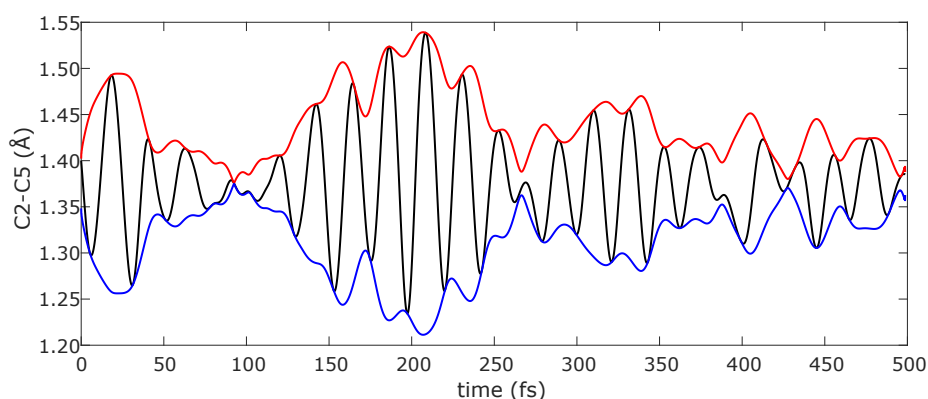


Figure 6.6: Sample trajectory.

By performing this procedure for the C2-C5 bond length along the 18 trajectories, we obtained an average of 265 fs with a standard deviation of 140 fs ( $265 \pm 140$  fs) to reach the equilibrium bond length. Similarly, when we performed the same analysis considering the C1-N7 bond length and the C1-N7-H8 angle (see Figure 6.5), we obtained timescales of  $238 \pm 171$  and  $249 \pm 183$  fs respectively. The resemblance of the timescales obtained using different degrees of freedom supports the validity of the proposed metric but more trajectories should be run in order to improve our analysis. So far, the fact that the relaxation times determined from our AIMD simulations are around 200 fs follows in line with the hypothesis that the transient depletion of  $\text{ONA}^+$  during the first 200 fs of the FTRMS measurements is related with the time it takes to get from the  $S_0$  to the  $D_0$  geometry.

### 6.3.4 Dissociation pathways

As discussed before, ONA is good model for TATB because it undergoes the same fragmentation pathways but despite the numerous computational investigations of the reaction pathways for neutral TATB,<sup>147,150,154,155</sup> there is, to the best of our knowledge, a lack of studies on the reactions of the TATB and ONA cations. This section attempts to fill this gap by showing a detailed study of the three main fragmentation pathways of ONA cation.

Figure 6.7 shows the so-called direct pathway for  $\text{ONA}^+$  decomposition which starts with a barrierless loss of  $\text{NO}_2$  producing the 92 m/z fragment experimentally detected. The energy difference between the dissociation products and the reagent of this process is 2.53 eV. Then the produced  $\text{C}_6\text{H}_6\text{N}^+$  fragment undergoes a 1,3-hydrogen shift that needs 2.56 eV to reach the corresponding transition state (TS1a) generating the intermediate INT1a afterwards. The

symmetry of INT1a makes it possible to break the C-C bond in the vicinity of nitrogen in two different ways, leading to two different transition states (TS2a and TS3a) that produce the ring-contraction intermediate INT2a. Then, by means of a barrierless process, INT2a originates the  $C_5H_5^+$  and HNC fragments. The fragment  $C_5H_5^+$  with 65 m/z is also recorded in our experiments. There is a long-standing controversy about which of the isomers of  $C_5H_5^+$  is the most stable between the vinylcyclopropenyl singlet cation and the cyclopentadienyl triplet cation with the answer depending on the level of theory used for the computation.<sup>172–174</sup> In any case, these studies agree in showing that the energies of the isomers are close to each other within 3 kcal/mol (0.13 eV). Due to the nature of the methods employed in this work, the most directly comparable report is the one by Kharnaier and collaborators<sup>174</sup> which used the B3LYP/6-311++G(d,p) level of theory among other methods. The zero point corrected energies obtained by them showed the cyclopentadienyl triplet cation being more stable by 1.15 kcal/mol while our calculations at the CAM-B3LYP/6-311+G\* level showed it to be more stable by 2.05 kcal/mol. Figure 6.7 shows the generation of the cyclopentadienyl triplet and singlet cations from INT2a but it should be kept in mind the possibility of also having the vinylcyclopropenyl cation. It is relevant to mention that this pathway proceeds to the generation of  $C_3H_3^+$ , detected as a fragment with 39 m/z, but that portion of the pathway has not been explored yet.

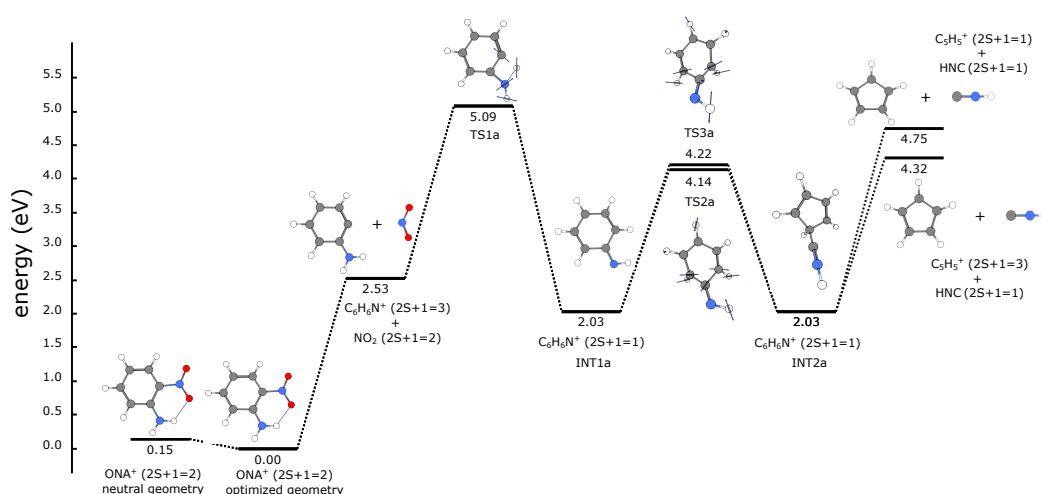


Figure 6.7: Direct pathway for ONA<sup>+</sup> fragmentation calculated at the CAM-B3LYP/6-311+G\* level of theory.

Figure 6.8 shows the fragmentation pathway that starts with the nitro-nitrate rearrangement with a barrier of 2.21 eV associated with the transition state TS1b. This is followed

by the generation of the  $\text{C}_6\text{H}_6\text{NO}^+$  and NO fragments preceded by the formation of the transition state TS2b. The  $\text{C}_6\text{H}_6\text{NO}^+$  fragment with 108 m/z is detected in our FTRMS measurements and it can be deemed as a proof that  $\text{ONA}^+$  undergoes NNR rearrangement. Then, this fragment experiences a ring contraction to generate intermediate INT1b after surpassing a barrier of 1.95 eV associated with the transition state TS3b. Finally, INT1b gives origin to the  $\text{C}_5\text{H}_6\text{N}^+$  and CO fragments, with the former being detected as the 80 m/z fragment in our experiments.

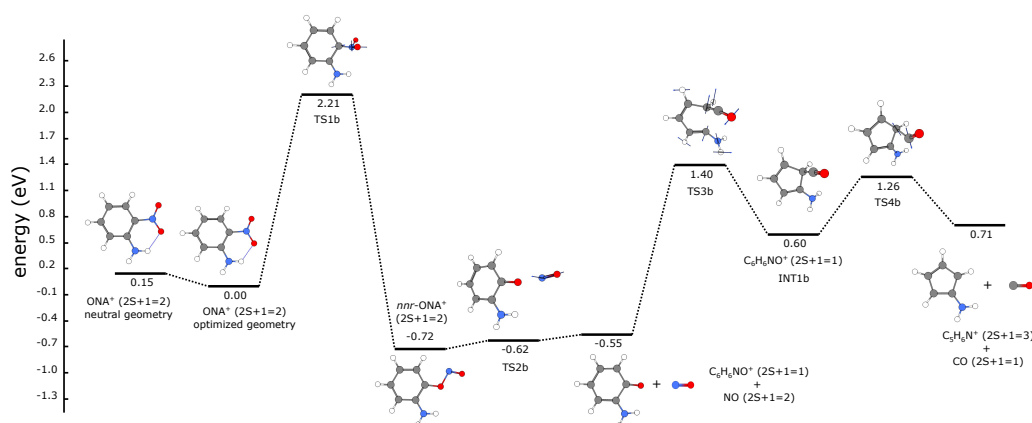


Figure 6.8: NNR pathway for  $\text{ONA}^+$  fragmentation calculated at the CAM-B3LYP/6-311+G\* level of theory.

Figure 6.9 shows the first part of the *aci*-rearrangement pathway of  $\text{ONA}^+$ . At this moment, it is worth discussing the methodology employed for obtaining the intermediates INT1c and INT4c to INT7c shown in this pathway. A previous work from our group explored the *aci*-rearrangement pathway of *o*-nitrotoluene cation ( $\text{ONT}^+$ )<sup>77</sup> and found three different conformers of the *aci*-rearranged  $\text{ONT}^+$  within a window of approximately 12 kcal/mol. As mentioned in Subsection 6.2.2, CREST/xtb was used to explore the conformational landscape of the different species considered in this work and in view of the previous results for  $\text{ONT}^+$  we decide to use a wide threshold of 20 kcal/mol for the exploration of the conformers of the *aci*-rearranged  $\text{ONA}^+$ . As a result of this methodology, we obtained seven different conformers within an energetic window of 12.5 kcal/mol (0.54 eV), four of which participate into the pathway shown in Figure 6.9. Cartesian coordinates for the seven conformers obtained, from INT1c to INT7c, can be found in the Appendix C, Tables C8–C11. The pathway starts with the hydrogen transfer between the amino and the nitro group of  $\text{ONA}^+$  to form the transition state TS1c which has an energy of 2.04 eV above the one for the relaxed cation. This leads to the intermediate INT1c which then, through the transition state TS2c, converts

to INT4c. At this point, the pathway can proceed in two different ways towards INT7c: it can go in a stepwise fashion through intermediates INT5c and INT6c with energetic barriers around 0.4 eV or it can proceed directly with a barrier of 0.8 eV. The existence of all these intermediates and rearrangements between them seem to be enabled by the H-bonds that can be formed in multiple ways.

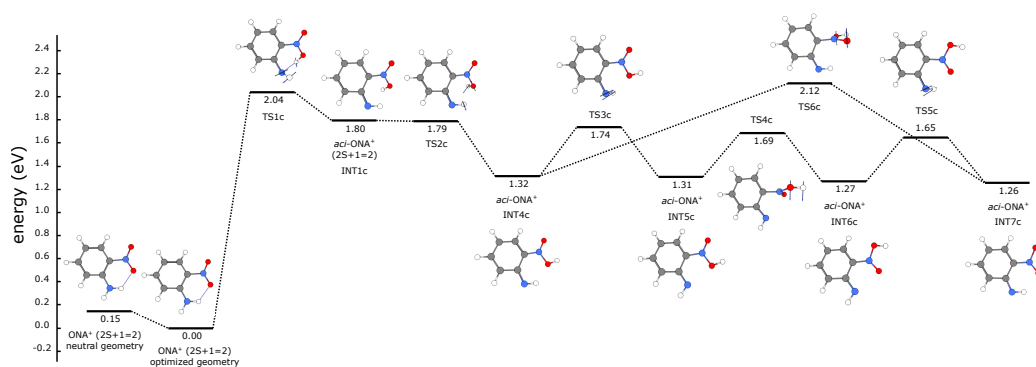


Figure 6.9: First part of the H transfer pathway for ONA<sup>+</sup> fragmentation calculated at the CAM-B3LYP/6-311+G\* level of theory.

It is worth to mention that, as far as the *aci*-rearrangement pathway goes, there has been no generation of any fragment from ONA<sup>+</sup>. Figure 6.10 shows the first fragmentations of this pathway starting from intermediates INT5c and INT6c previously shown in Figure 6.9. Both INT5c and INT6c can undergo the direct loss of nitrous acid (HONO) to form C<sub>6</sub>H<sub>5</sub>N<sup>+</sup> experimentally detected as the 91 m/z fragment. In both cases, the energy difference between products and reagents is around 3 eV. As shown in Figures 6.9 and 6.10, there is the possibility of interconversion between INT5c and INT6c but OH loss pathways only proceed from the latter. In this regard, there are two possibilities: it can proceed directly with the generation of C<sub>6</sub>H<sub>5</sub>N<sub>2</sub>O<sup>+</sup> in the triplet state and with an energy difference of 2.01 eV or it can go through the generation of a cyclic intermediate (INT8c) up to the formation of C<sub>6</sub>H<sub>5</sub>N<sub>2</sub>O<sup>+</sup> in the singlet state.

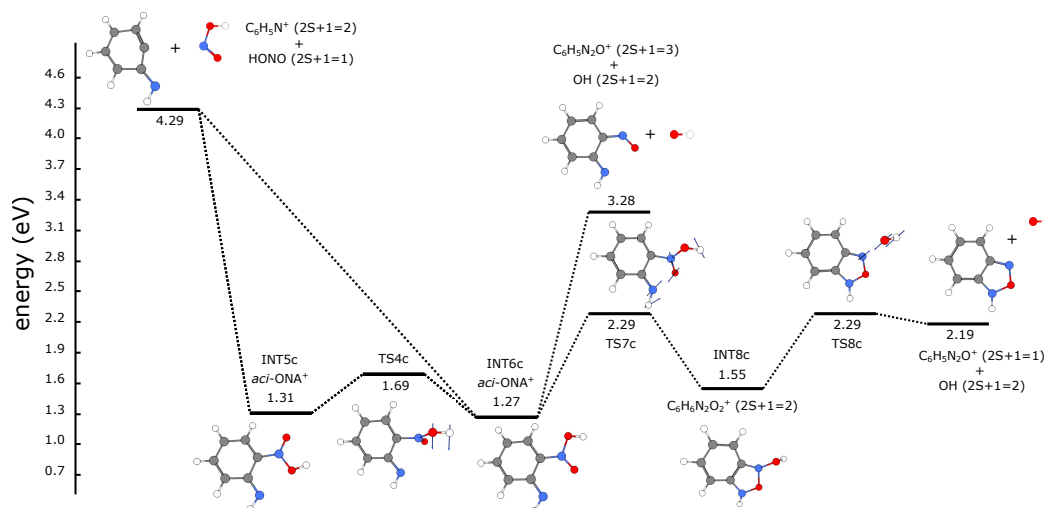


Figure 6.10: Second part of the H transfer pathway for ONA<sup>+</sup> fragmentation calculated at the CAM-B3LYP/6-311+G\* level of theory.

The calculated energies including the zero point energy (ZPE) for all the species included in Figures 6.7 to 6.10 as well as the frequencies for all the transition states can be found in the Appendix C (Tables C12–C14 for the energies and C15–C18 for the frequencies).

## 6.4 Conclusions

This work offers some insights on the dynamics, stability, and fragmentation pathways of ONA radical cation as a model for the military explosive TATB. Electronic structures calculations showed a strong  $D_0$  to  $D_5$  transition  $\sim 3.5$  eV capable of producing fragmentation as confirmed by FTRMS measurements. This transition requires a higher energy than the bright transition  $\sim 2$  eV inducing fragmentation in other nitroaromatic radical cations previously studied, giving evidence of the greater stability of ONA<sup>+</sup> relative to those other radical cations. The oscillator strength and therefore the intensity of the  $D_0$  to  $D_5$  transition changes as the ONA cation transitions from the vertical  $S_0$  geometry to the relaxed  $D_0$  geometry. This change in the coupling between the  $D_0$  and  $D_5$  states as ONA cation relaxes seems to be related with the transient depletion of the ONA<sup>+</sup> ion yield observed during the first 200 fs of our dynamic measurements. Complementarily, we performed AIMD simulations intended to estimate the relaxation time of ONA cation. Our preliminary results also point towards a timescale around 200 fs, in line with our hypothesis. Finally, we present detailed mechanisms

for the direct, NNR, and H transfer pathways with initial energetic barriers of 2.53, 2.21, and 2.04 eV respectively.

## Chapter 7

# Conclusions and future work

This work focused on the combined use of femtosecond time-resolved mass spectrometry (FTRMS) and computational chemistry to elucidate the dynamic behavior of nitroaromatic radical cations and their corresponding fragmentation products.

Chapter 4 includes the calculation of electronic potential energy surfaces of the nitrobenzene cation by time-dependent density functional theory and coupled-cluster calculations. Both levels of theory identified a strongly-coupled transition from the ground state of the nitrobenzene cation with a geometry-dependent oscillator strength, reaching a maximum at 90° C–C–N–O dihedral angle with a corresponding energy gap of  $\sim 2$  eV. These computational results follow in line with the experimental observation of a vibrational wave packet. We used this information to predict the most efficient probe wavelength for femtosecond time-resolved mass spectrometry measurements. The validity of our prediction was experimentally confirmed by using two different probe wavelengths. The use of a probe wavelength of 650 nm, nearly resonant with the strong transition found in our calculations, resulted in an enhanced ion yield oscillation amplitudes as compared to excitation with the nonresonant 800 nm probe.

Chapter 5 reports pump-probe control schemes to manipulate fragmentation product yields in *p*-nitrotoluene cation (PNT). Strong field ionization of PNT prepares the parent cation in the ground electronic state, with coherent vibrational excitation along two normal modes: the C–C–N–O torsional mode at  $80\text{ cm}^{-1}$  and the in-plane ring-stretching mode at  $650\text{ cm}^{-1}$ . Both vibrational wave packets are observed as oscillations in parent and fragment ion yields in the mass spectrum upon optical excitation. Excitation with 650 nm selectively fragments the PNT cation into  $\text{C}_7\text{H}_7^+$ , whereas excitation with 400 nm selectively produces

$C_5H_5^+$  and  $C_3H_3^+$ . *Ab initio* calculations of the ground and excited electronic potential energy surfaces of PNT cation along the C-C-N-O dihedral angle reveal that 400 nm excitation accesses an allowed transition from  $D_0$  to  $D_6$  at  $0^\circ$  dihedral angle, whereas 650 nm excitation accesses a strongly allowed transition from  $D_0$  to  $D_4$  at a dihedral angle of  $90^\circ$ . This ability to access different electronic excited states at different locations along the potential energy surface accounts for the selective fragmentation observed with different probe wavelengths. The ring-stretching mode, only observed using 800 nm excitation, is attributed to a  $D_0$  to  $D_2$  transition at a geometry with  $90^\circ$  dihedral angle and elongated C-N bond length. Collectively, these results demonstrate that strong field ionization induces multimode coherent excitation and that the vibrational wave packets can be excited with specific photon energies at different points on their potential energy surfaces to induce selective fragmentation.

Chapter 6 shows work in progress offering some insights on the stability and fragmentation pathways of *o*-nitroaniline radical cation as a model for the military explosive 2,4,6-triamino-1,3,5-trinitrobenzene (TATB). We offered evidence of a strong  $D_0$  to  $D_5$  transition  $\sim 3.5$  eV inducing fragmentation. This transition requires a higher energy than the bright transition  $\sim 2$  eV inducing fragmentation in other nitroaromatic radical cations previously studied. The oscillator strength of the  $D_0$  to  $D_5$  transition changes as  $ONA^+$  relaxes from the  $S_0$  to the  $D_0$  geometry and this seems to be related with the transient depletion of the  $ONA^+$  ion yield observed during the first 200 fs of our dynamic measurements. This hypothesis finds support in the results obtained from AIMD simulations showing a relaxation time for  $ONA^+$  also around 200 fs. Finally, we present detailed mechanisms for the direct, NNR, and H transfer pathways with initial energetic barriers of 2.53, 2.21, and 2.04 eV respectively.

Future work is related with the study of the  $ONA$  radical cation. The AIMD simulations that we have so far seem to support the hypothesis that the transient depletion suffered by  $ONA^+$ , and mirrored by an enhancement of most of the fragmentation products during the first 200 fs, is related with the timescale for the relaxation of  $ONA^+$ . Further support of this hypothesis requires the calculation of more AIMD trajectories in order to improve the statistical analysis. Additionally, and in close relationship with the last point, the fragment  $C_6H_5N_2O^+$  does not show the previously discussed enhancement during the first 200 fs in sharp contrast with the rest of the products, as can be seen in top panel of Figure 6.4. The current hypothesis is that, since it is well known that this fragment can only be produced after the *aci*-rearrangement pathway, it is possible that it might be subtracted from the fate of

the rest of fragments by a fast hydrogen transfer process. This hypothesis has some support on previous computations from our group showing that this hydrogen transfer can occur in a timescale of approximately 20 fs for *o*-nitrotoluene radical cation.<sup>77</sup> In order to have more elements to test this hypothesis, it would be valuable to have AIMD simulations of the H transfer process in ONA<sup>+</sup>.

In a broader sense, future work in the lab will be related with performing gas phase FTRMS experiments and computations on radical cations of actual energetic molecules such as TNT and TATB in order to compare how their dynamics, electronic structures, and fragmentations pathways compare to the models studied so far (NB<sup>+</sup>, PNT<sup>+</sup>, and ONA<sup>+</sup> among others). Up to this point, the execution of FTRMS experiments of actual energetic molecules has been hindered by the fact that these molecules have a low vapor pressure and therefore cannot be studied in our current experimental setup, since this relies on the volatility of the samples to perform gas phase measurements. This obstacle will be circumvented by the laser desorption post-ionization setup that is currently being optimized by members of our lab and is expected to be fully operational in the near future. In this regard, the experimental capability of having laser desorption of molecules from thin layers might also open the possibility of studying this processes by means of solid-state DFT and molecular dynamics methods. The theoretical knowledge gained by this means could aid in the design of experimental conditions.

Other avenue of future work is related with the extension of the time-resolved experimental capabilities of the lab to the liquid phase. In this sense, we have performed the initial steps to build a transient absorption spectroscopy (TAS) setup in collaboration with the Electrical Engineering Department of VCU. The initial work already performed consists on the implementation of a supercontinuum femtosecond laser source to be used as a probe for the TAS setup. This setup will enable the study of a multitude of systems in solution but, just to mention a couple of examples, our lab is interested in studying the dynamics and mechanisms of the visible light-induced photochemical reactions of 2,2,6,6-tetramethylpiperidine-N-oxyl (TEMPO)<sup>175</sup> and the laser synthesis of nanoparticles from nickelocene solutions.

## Appendix A

[Link back to chapter 4.](#)

### Supplemental Figures

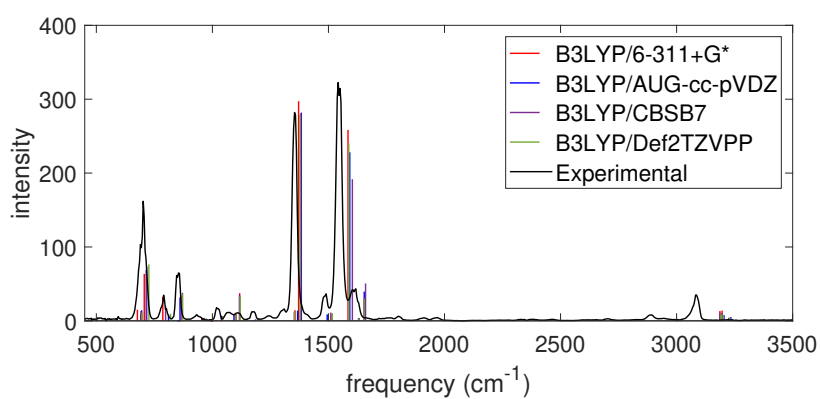


Figure A1: Experimental (black) and computed infrared spectra using the B3LYP functional with different basis sets for NB.

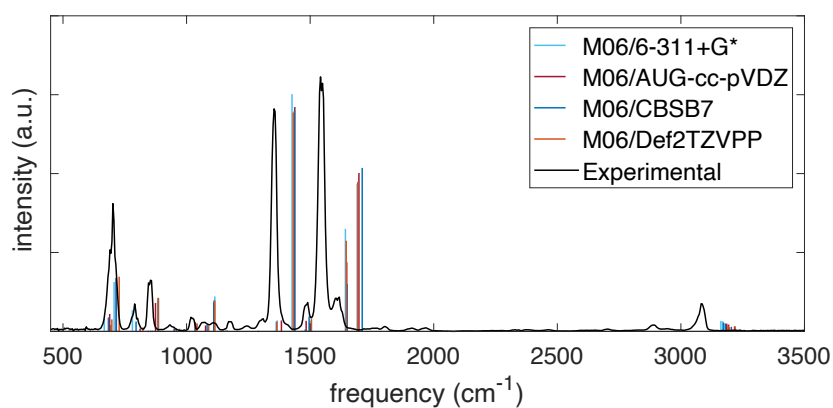


Figure A2: Experimental (black) and computed infrared spectra using the M06 functional with different basis sets for NB.

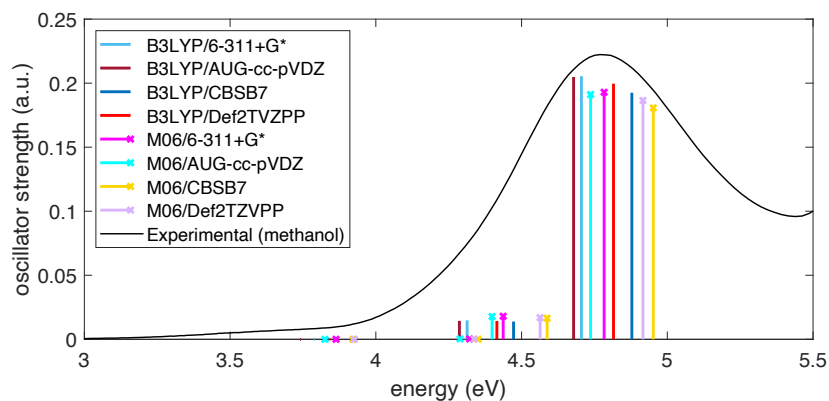


Figure A3: Experimental (black) and computed UV-Vis spectra using the B3LYP and M06 functionals with different basis sets for NB.

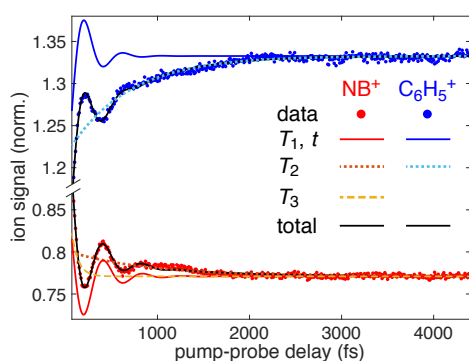


Figure A4: Ion signals (dots) of  $\text{NB}^+$  (red) and  $\text{C}_6\text{H}_5^+$  (blue) obtained with 650 nm probe pulses at  $10^{12} \text{ W cm}^{-2}$ , with fits to eq 1 in Chapter 4 (black lines) and components  $T_1$ ,  $T_2$ , and  $T_3$  (solid, dotted, and dashed lines).  $\text{C}_6\text{H}_5^+$  did not require a  $T_3$  component.

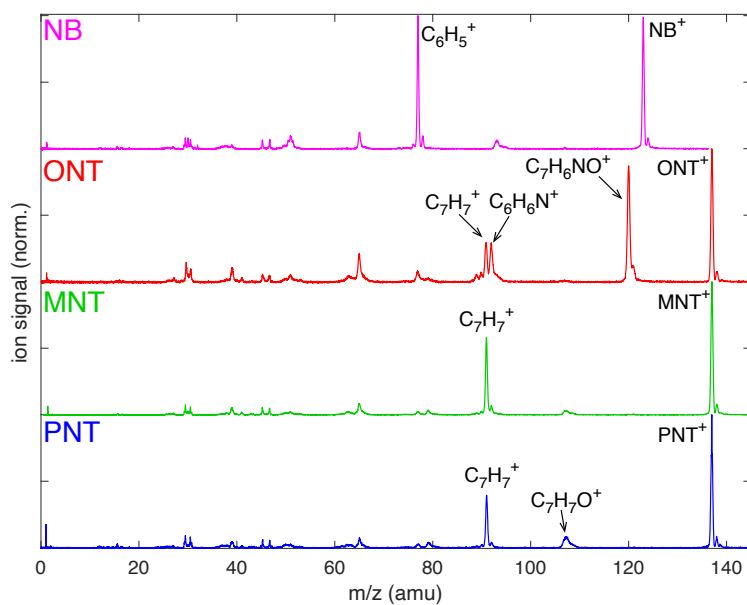


Figure A5: Mass spectra of NB (magenta), ONT (red), MNT (green), and PNT (blue) taken with 1300 nm pump only.

## Tabulated theoretical results

	Neutral			Cation		
C	0.241731	0.000000	0.000037	0.239436	-0.005728	0.015543
C	-0.429303	-1.215050	0.000072	-0.423645	-1.231631	0.232515
C	-1.817324	-1.207038	0.000044	-1.792522	-1.216632	0.223226
C	-0.429303	1.215050	-0.000037	-0.427462	1.224794	-0.226463
C	-1.817323	1.207038	-0.000062	-1.796491	1.218089	-0.229544
C	-2.509993	0.000000	-0.000022	-2.485236	0.004167	-0.009561
N	1.718763	0.000000	0.000096	1.691325	0.001143	0.022143
O	2.286043	1.081198	0.000085	2.271968	-0.390600	1.004127
O	2.286045	-1.081198	-0.000190	2.192149	0.402257	-1.015975
H	0.133992	-2.135132	0.000127	0.145562	-2.133022	0.411568
H	-2.357594	-2.143644	0.000073	-2.354042	-2.124272	0.394744
H	-3.591754	0.000000	-0.000046	-3.567685	-0.000543	-0.020030
H	-2.357593	2.143644	-0.000112	-2.351615	2.129048	-0.402238
H	0.133993	2.135132	-0.000069	0.148641	2.122930	-0.400057

Table A1: Geometric coordinates for neutral and cationic NB optimized at the B3LYP/Def2TZVPP level.

Atom	RMSD	MRMSD
C1	0.01385	0.01385
C2	0.11181	0.11181
C3	0.10986	0.10986
C4	0.10562	0.10562
C5	0.10675	0.10675
C6	0.02507	0.02507
N7	0.03129	0.03129
O8	1.83292	1.83292
O9	1.86775	1.86775
H10	0.19432	0.19432
H11	0.18418	0.18418
H12	0.02649	0.02649
H13	0.18032	0.18032
H14	0.18726	0.18726
All H atoms	0.16731	0.37412
All C atoms	0.08939	0.21896
All N atoms	0.03129	0.03129
All O atoms	1.85042	2.61689
All atoms	0.70897	2.65272

Table A2: Root-mean-square distance (RMSD) and modified RMSD (MRMSD, see definition on Chapter 4) between neutral and cationic NB optimized at the B3LYP/Def2TZVPP level. Values are given in Å.

6-311+G*		CBSB7		AUGCCPVDZ		DEF2TZVPP	
Frequency	Intensity	Frequency	Intensity	Frequency	Intensity	Frequency	Intensity
49.44	0.00	52.63	0.00	55.51	0.00	51.42	0.00
168.56	0.86	169.83	0.83	170.36	0.93	169.46	0.93
255.75	0.98	257.25	1.11	253.88	0.82	256.82	0.88
394.76	0.85	395.76	1.07	394.44	1.12	395.89	1.04
416.89	0.00	417.99	0.00	418.36	0.00	420.13	0.00
439.68	1.03	444.99	0.51	447.72	0.69	450.06	0.54
526.65	1.15	527.30	1.20	523.20	1.32	526.38	1.26
627.63	0.05	627.16	0.03	621.10	0.05	628.61	0.04
676.89	15.08	692.17	13.43	691.00	9.15	697.20	11.04
696.86	8.33	697.23	8.92	695.43	14.28	698.22	8.82
706.48	63.58	714.63	68.73	716.81	73.18	726.31	76.34
786.44	32.61	798.37	19.71	810.90	7.79	819.72	9.54
853.33	0.00	859.61	0.00	849.94	0.00	862.79	0.00
868.79	34.18	871.06	37.85	860.57	31.69	871.10	35.96
954.12	4.39	964.63	4.01	957.47	3.06	973.11	3.60
990.30	0.00	999.15	0.00	995.34	0.00	1006.92	0.00
1010.57	0.16	1018.75	0.21	1012.90	0.23	1024.48	0.25
1020.07	0.31	1018.86	0.23	1016.79	0.04	1024.93	0.14
1043.67	6.03	1042.37	5.56	1038.91	6.91	1045.18	6.45
1102.75	8.85	1098.36	10.03	1093.02	8.62	1101.35	8.38
1117.63	37.52	1117.06	33.63	1117.07	34.21	1119.54	33.52
1188.41	0.70	1184.07	0.40	1174.37	0.53	1186.51	0.60
1199.93	3.45	1194.74	1.69	1186.23	1.95	1197.64	2.81
1344.03	0.06	1335.44	0.78	1319.05	0.04	1342.77	0.28
1355.90	14.48	1353.16	11.92	1367.20	13.82	1353.23	12.89
1371.42	297.31	1381.04	280.44	1383.20	281.80	1377.21	278.89
1491.98	0.25	1488.84	0.55	1473.43	0.07	1493.28	0.07
1515.56	8.90	1510.04	11.18	1494.63	8.75	1516.48	10.56
1584.35	258.52	1603.07	191.73	1591.84	228.16	1587.68	240.15
1632.54	3.80	1631.18	3.19	1629.41	3.61	1631.14	3.10
1654.50	30.41	1659.87	50.54	1654.22	39.58	1653.79	30.48
3173.63	0.92	3173.35	0.75	3182.97	0.63	3178.95	0.68
3186.59	13.39	3186.11	11.16	3195.16	8.85	3191.85	9.02
3195.87	13.90	3195.11	10.49	3204.07	7.75	3200.42	8.14
3226.52	0.02	3224.43	0.42	3233.07	0.57	3229.56	0.47
3226.75	3.72	3224.71	4.17	3233.44	5.11	3229.69	4.76

Table A3: Calculated harmonic frequencies ( $\text{cm}^{-1}$ ) and intensities for NB using the B3LYP functional with different basis sets.

6-311+G*		CBSB7		AUGCCPVDZ		DEF2TZVPP	
Frequency	Intensity	Frequency	Intensity	Frequency	Intensity	Frequency	Intensity
50.72	0.00	53.21	0.00	58.70	0.00	55.11	0.00
167.49	0.91	168.40	0.87	168.98	0.93	169.02	0.99
257.90	0.88	258.41	1.02	255.89	0.77	256.14	0.83
397.78	0.96	397.95	1.14	396.18	1.24	396.57	1.19
411.71	0.00	412.22	0.00	412.35	0.00	417.06	0.00
430.11	0.95	437.21	0.52	441.38	0.70	446.39	0.42
529.65	0.79	530.24	0.86	525.60	0.97	528.68	0.86
617.95	0.07	617.26	0.03	609.87	0.05	619.14	0.05
666.86	16.50	683.78	17.57	687.02	8.37	694.28	8.04
693.74	7.39	693.90	7.65	688.85	22.07	697.63	15.20
706.85	62.62	714.98	67.52	715.83	67.97	727.42	69.28
780.89	26.93	795.68	12.47	811.88	3.42	823.58	4.99
849.43	0.00	853.54	0.00	842.65	0.00	860.39	0.00
884.06	38.83	886.20	42.27	874.29	35.89	884.54	42.60
948.79	4.01	957.95	3.71	950.40	2.68	971.21	3.28
987.72	0.00	994.72	0.00	987.56	0.00	1008.69	0.00
1008.33	0.09	1011.02	0.14	1002.52	0.15	1018.89	0.31
1012.53	0.19	1012.61	0.13	1011.10	0.02	1028.45	0.08
1040.45	8.63	1038.00	9.24	1034.35	11.89	1042.33	10.27
1090.14	6.61	1083.13	8.36	1076.86	7.44	1087.94	7.26
1114.28	44.29	1111.12	39.20	1110.01	36.45	1114.24	38.98
1163.48	1.18	1158.78	0.83	1147.82	1.03	1164.55	1.05
1180.24	0.20	1175.24	0.03	1167.64	0.08	1180.12	0.08
1312.09	0.03	1304.66	0.32	1288.28	0.00	1314.35	0.08
1366.71	13.91	1363.38	12.27	1383.75	13.80	1364.89	12.30
1426.68	300.74	1436.38	279.62	1437.92	284.35	1431.54	277.47
1482.28	0.99	1479.88	2.37	1468.81	0.75	1487.30	1.04
1499.92	13.83	1495.72	18.75	1483.78	13.37	1505.29	16.33
1642.64	129.90	1643.76	2.62	1643.96	3.21	1645.70	2.27
1644.91	3.13	1649.48	60.11	1648.03	87.73	1646.02	114.83
1690.06	187.10	1710.63	207.20	1697.32	200.75	1692.71	189.55
3147.31	1.81	3158.56	1.57	3173.23	1.02	3175.52	1.35
3161.88	13.33	3172.51	11.11	3185.44	9.72	3190.55	7.22
3169.30	12.73	3179.82	10.03	3193.23	8.69	3196.86	5.24
3194.88	0.01	3204.25	0.32	3217.20	6.28	3219.36	6.34
3194.91	5.34	3204.34	5.76	3217.43	0.30	3219.41	0.65

Table A4: Calculated harmonic frequencies ( $\text{cm}^{-1}$ ) and intensities for NB using the M06 functional with different basis sets.

6-311+G*		CBSB7		AUGCCPVDZ		DEF2TZVPP	
Frequency	Intensity	Frequency	Intensity	Frequency	Intensity	Frequency	Intensity
37.48	0.05	67.63	0.06	31.82	0.05	53.87	0.03
63.13	0.32	96.41	4.46	51.54	0.26	74.35	5.78
159	0.61	189.65	7.2	157.41	0.75	169.1	6.16
247.06	6.61	273.52	16.91	240.18	6.54	248.4	11.43
363.34	1.25	363.84	3.04	361.37	0.39	362.93	1.97
365.06	1.19	368.22	0.33	362.46	1.76	366.48	0.67
394.98	0.65	408.62	6.52	395.2	0.76	401.63	4.02
496.05	0.77	513.14	6.01	496.56	0.59	504.76	2.22
622.38	35.02	622.78	35.06	620.3	32.14	628.64	33.46
669.75	0.02	666.41	0.12	660.45	0	668.15	0.34
724.81	17.12	719.52	26.2	719.29	12.96	729.37	15.28
792.2	53.13	786.07	47.06	786.53	44.11	793.56	42.42
802.73	39.28	800.39	50.69	796.98	3.82	808.64	30.08
804.94	3.14	815.32	2.85	800.42	33.78	816.63	11.3
965.23	5.2	967.31	5.81	959.35	4.93	976.14	7.03
980.51	58.9	982.32	62.17	980.75	55.58	983.67	58.1
1003.5	0.01	1001.54	0.05	995.37	0.03	1007.61	0.02
1008.27	0.16	1012.9	0.1	999.61	0.46	1023.49	0.06
1020.1	0.73	1017.8	1.04	1012.91	0.65	1034.91	0.64
1068.92	3.23	1079.5	5.09	1070.26	3.92	1077.45	4.2
1142.2	7.62	1136.09	0.75	1142.44	5.1	1142.34	2.03
1162.93	3.9	1156.73	5.16	1152.22	2.63	1162.3	3.54
1219.69	10.09	1211.72	7.24	1206.51	9.29	1216.86	9.67
1297.21	14.78	1303.47	10.68	1290.38	8.62	1301.35	11.61
1385.46	20.14	1335.19	186.52	1368.12	7.64	1370.44	107.73
1392.31	19.14	1388.05	21.68	1397.29	19.97	1392.74	22.04
1404	15.47	1400.97	10.48	1417.67	13.33	1404.14	7.65
1444.64	79.87	1462.56	116.99	1442.53	122.95	1468.36	128.06
1466	114.59	1485.11	167.63	1460.07	79.33	1471.78	111.72
1521.39	37.17	1514.05	31.52	1506.64	44.49	1522.2	34.53
1645.31	106.9	1626.34	99.84	1642.33	100.3	1638.84	98.4
3201.78	0.01	3195.9	0.39	3201.93	0.56	3197.64	0.52
3211.06	1.1	3206.67	3.25	3212.13	1.01	3209.04	2.59
3213.08	6.75	3209.74	8.74	3213.98	12.13	3211.01	9.57
3221.08	25.62	3216.81	29.74	3222.62	36.94	3218.85	32.12
3223.3	0.09	3219.75	6.92	3224.78	0.61	3221.33	3.79

Table A5: Calculated harmonic frequencies ( $\text{cm}^{-1}$ ) and intensities for NB cation using the B3LYP functional with different basis sets.

6-311+G*		CBSB7		AUGCCPVDZ		DEF2TZVPP	
Frequency	Intensity	Frequency	Intensity	Frequency	Intensity	Frequency	Intensity
71.29	0.90	58.64	0.48	62.64	0.89	47.60	0.32
82.05	0.61	75.02	1.13	73.87	0.39	69.90	0.85
173.26	1.36	164.96	0.62	168.93	1.05	158.38	0.46
259.10	5.37	259.69	5.96	256.29	5.48	252.15	6.22
355.27	2.17	355.53	2.75	350.75	1.63	359.30	2.55
366.40	4.47	368.41	3.51	365.10	5.00	366.69	3.57
377.68	0.48	374.39	0.56	375.27	0.44	379.46	0.55
474.65	1.11	481.88	0.83	465.38	1.14	486.73	0.70
612.54	31.67	609.46	29.52	608.73	28.25	620.05	27.10
672.81	4.00	673.05	2.42	664.71	4.26	671.99	3.63
730.15	25.19	725.70	30.72	721.98	20.02	734.51	20.80
795.27	1.03	795.73	25.63	784.65	0.69	805.03	2.84
799.95	28.89	796.71	3.15	799.38	23.96	813.13	23.53
820.11	13.17	813.99	19.49	812.24	7.98	816.14	13.01
951.82	6.61	951.75	6.97	946.76	6.18	966.49	7.25
980.05	63.07	980.19	60.90	977.16	54.50	983.83	62.11
995.93	0.05	992.09	0.68	985.64	2.61	1001.62	0.45
1001.53	0.09	993.51	0.59	989.62	1.48	1019.64	0.05
1005.20	0.57	1002.67	0.27	996.17	0.53	1024.51	0.41
1052.56	1.88	1054.71	3.18	1046.55	2.21	1061.38	2.88
1142.41	7.74	1139.32	5.14	1131.58	3.40	1144.20	6.58
1145.76	3.33	1140.70	3.31	1139.23	4.55	1147.20	2.99
1202.19	9.28	1197.89	9.60	1190.57	10.18	1203.16	10.08
1286.87	11.71	1284.72	8.88	1272.97	8.09	1291.15	9.63
1363.61	6.43	1358.77	5.71	1343.82	4.93	1370.14	6.00
1417.55	27.34	1413.44	26.18	1420.98	21.75	1413.69	25.46
1439.35	127.28	1434.20	130.26	1421.74	147.79	1441.33	66.65
1447.31	21.88	1444.46	13.81	1455.01	0.04	1449.45	76.62
1515.78	53.48	1510.73	53.67	1508.73	58.52	1519.75	50.43
1582.22	160.42	1568.31	120.02	1602.43	148.24	1564.21	142.38
1664.33	68.61	1660.02	80.47	1662.97	60.80	1664.35	74.73
3158.00	0.65	3165.05	1.46	3177.65	1.57	3178.63	2.64
3175.78	4.88	3184.61	5.54	3195.73	4.74	3199.96	8.41
3176.08	7.81	3184.66	11.28	3196.09	9.74	3200.03	9.57
3186.10	25.65	3194.70	33.70	3206.28	30.19	3210.04	40.28
3187.84	0.23	3196.32	0.57	3207.65	0.44	3211.69	1.33

Table A6: Calculated harmonic frequencies ( $\text{cm}^{-1}$ ) and intensities for NB cation using the M06 functional with different basis sets.

	6-311+G*		CBSB7		AUGCCPVDZ		DEF2TZVPP	
State	EE	f	EE	f	EE	f	EE	f
S1	3.7867	0	3.835	0	3.74	0	3.8413	0
S2	4.3037	0.0003	4.3277	0.0001	4.2676	0.0003	4.3423	0.0002
S3	4.3132	0.0148	4.4725	0.0139	4.2867	0.0144	4.4153	0.0143
S4	4.7053	0.2054	4.8783	0.1925	4.6785	0.2048	4.8154	0.1996
S5	5.9144	0.001	6.0127	0.0001	5.8483	0.0026	5.9682	0
S6	6.0367	0.0621	6.1241	0.055	5.9704	0.0594	6.0931	0.0604
S7	6.3457	0	6.2888	0	6.237	0.0001	6.305	0
S8	6.4389	0.177	6.5457	0.1777	6.3824	0.1899	6.4839	0.1916
S9	6.5271	0	6.6172	0	6.4134	0	6.5238	0
S10	6.7257	0	6.6559	0	6.6026	0	6.6699	0

Table A7: Calculated excitation energies (eV) and oscillator strengths (a.u.) for NB using the B3LYP functional with different basis sets under the TDDFT formalism.

	6-311+G*		CBSB7		AUGCCPVDZ		DEF2TZVPP	
State	EE	f	EE	f	EE	f	EE	f
S1	3.8634	0.0000	3.9214	0.0000	3.8254	0.0000	3.9259	0.0000
S2	4.3217	0.0003	4.3510	0.0001	4.2889	0.0003	4.3373	0.0002
S3	4.4369	0.0180	4.5877	0.0165	4.3988	0.0178	4.5637	0.0169
S4	4.7832	0.1929	4.9518	0.1807	4.7368	0.1911	4.9164	0.1865
S5	5.9566	0.0092	6.0762	0.0172	5.9064	0.0098	6.0378	0.0133
S6	6.1733	0.0000	6.4048	0.0499	5.9839	0.0000	6.3253	0.0642
S7	6.2717	0.0613	6.4430	0.1995	6.1272	0.0065	6.3828	0.2188
S8	6.3098	0.1967	6.5820	0.0000	6.1928	0.0615	6.5503	0.0000
S9	6.3259	0.0055	6.6217	0.0000	6.2307	0.2100	6.5568	0.0000
S10	6.5348	0.0000	6.8241	0.0000	6.3944	0.0000	6.7779	0.0000

Table A8: Calculated excitation energies (eV) and oscillator strengths (a.u.) for NB using the M06 functional with different basis sets under the TDDFT formalism.

	6-311+G*		CBSB7		AUGCCPVDZ		DEF2TZVPP	
State	EE	f	EE	f	EE	f	EE	f
D1	0.6386	0	0.6424	0	0.6448	0	0.6657	0
D2	1.1537	0.001	1.149	0.003	1.1669	0.001	1.1853	0.0025
D3	1.4923	0	1.4226	0.0034	1.5243	0	1.5346	0.0012
D4	1.7183	0.0799	1.6651	0.0694	1.7276	0.0779	1.7529	0.0777
D5	3.0281	0.0007	3.0017	0.0006	2.9696	0.0007	2.9779	0.0007
D6	3.0411	0	3.0679	0	3.059	0	3.153	0
D7	3.4059	0.0022	3.3944	0.0019	3.3869	0.002	3.4435	0.0017
D8	3.6041	0.0003	3.5643	0.0006	3.5396	0.0003	3.5556	0.0004
D9	3.7937	0.0074	3.6724	0.0088	3.7663	0.0039	3.7625	0.0077
D10	3.7989	0.0171	3.9523	0.0141	3.7838	0.0201	3.9489	0.0167

Table A9: Calculated excitation energies (eV) and oscillator strengths (a.u.) for NB cation using the B3LYP functional with different basis sets under the TDDFT formalism.

	6-311+G*		CBSB7		AUGCCPVDZ		DEF2TZVPP	
State	EE	f	EE	f	EE	f	EE	f
D1	0.6416	0.0000	0.6354	0.0000	0.6319	0.0000	0.6669	0.0000
D2	1.2956	0.0008	1.2138	0.0007	1.3078	0.0007	1.2172	0.0007
D3	1.6794	0.0001	1.5694	0.0001	1.7022	0.0001	1.6340	0.0001
D4	1.7905	0.0706	1.7225	0.0669	1.7842	0.0650	1.7620	0.0681
D5	3.0271	0.0007	2.9810	0.0007	2.9583	0.0007	2.9656	0.0007
D6	3.3725	0.0040	3.3697	0.0047	3.3405	0.0044	3.3778	0.0043
D7	3.4568	0.0001	3.4360	0.0002	3.4066	0.0001	3.4573	0.0002
D8	3.6111	0.0002	3.5802	0.0001	3.5515	0.0002	3.6056	0.0001
D9	3.9137	0.0283	3.9402	0.0290	3.8823	0.0299	3.9888	0.0303
D10	4.0236	0.0012	4.0303	0.0013	3.9935	0.0014	4.0484	0.0011

Table A10: Calculated excitation energies (eV) and oscillator strengths (a.u.) for NB cation using the M06 functional with different basis sets under the TDDFT formalism.

transition	neutral geometry		cation geometry	
	EE (eV)	$f$ (a.u.)	EE (eV)	$f$ (a.u.)
$D_0 \rightarrow D_1$	0.0929	0.000004	0.1385	0.000007
$D_0 \rightarrow D_2$	1.1993	0.000000	1.3287	0.000000
$D_0 \rightarrow D_3$	1.3146	0.000634	1.5099	0.000877
$D_0 \rightarrow D_4$	1.3755	0.000001	1.6319	0.000003
$D_0 \rightarrow D_5$	3.1485	0.040960	3.1052	0.040215

Table A11: Excitation energies (EE) and oscillator strengths ( $f$ ) for NB cation at the optimized neutral and cation geometries at the EOM-EE-CCSD/6-311+G\* level of theory.

## Tabulated curve fitting results

Tables A12 through A15 give the coefficients extracted from fitting transient ion signals obtained at conditions indicated to eq 1 in Chapter 4.

eq (1)	NB <sup>+</sup>	C <sub>6</sub> H <sub>5</sub> <sup>+</sup>	C <sub>4</sub> H <sub>3</sub> <sup>+</sup>
<i>a</i>	0.11 ± 0.02	0.13 ± 0.02	—
<i>T</i> <sub>1</sub> (fs)	242 ± 15	176 ± 15	—
<i>t</i> (fs)	426 ± 10	421 ± 14	—
<i>φ</i> (rad)	−0.04 ± 0.08	3.07 ± 0.09	—
<i>b</i>	0.031 ± 0.003	−0.116 ± 0.004	−0.024 ± 0.003
<i>T</i> <sub>2</sub> (fs)	870 ± 100	654 ± 28	230 ± 60
<i>c</i>	0.14 ± 0.06	—	0.016 ± 0.003
<i>T</i> <sub>3</sub> (fs)	72 ± 27	—	1660 ± 460
<i>d</i>	0.771 ± 0.001	1.333 ± 0.001	0.339 ± 0.001

Table A12: Coefficients extracted from transients at 650 nm, 10<sup>12</sup> W cm<sup>−2</sup> fitted to eq (1).

eq (1)	NB <sup>+</sup>	C <sub>6</sub> H <sub>5</sub> <sup>+</sup>	C <sub>4</sub> H <sub>3</sub> <sup>+</sup>
<i>a</i>	0.14 ± 0.02	0.28 ± 0.04	0.045 ± 0.008
<i>T</i> <sub>1</sub> (fs)	239 ± 15	153 ± 13	365 ± 64
<i>t</i> (fs)	430 ± 9	516 ± 22	464 ± 20
<i>φ</i> (rad)	−0.08 ± 0.09	3.37 ± 0.08	3.42 ± 0.25
<i>b</i>	0.076 ± 0.005	−0.144 ± 0.002	−0.32 ± 0.01
<i>T</i> <sub>2</sub> (fs)	736 ± 44	1770 ± 90	193 ± 13
<i>c</i>	0.27 ± 0.06	—	0.094 ± 0.004
<i>T</i> <sub>3</sub> (fs)	79 ± 16	—	3100 ± 500
<i>d</i>	0.771 ± 0.001	1.608 ± 0.001	0.538 ± 0.001

Table A13: Coefficients extracted from transients at 650 nm, 10<sup>13</sup> W cm<sup>−2</sup> fitted to eq (1).

eq (1)	NB <sup>+</sup>	C <sub>6</sub> H <sub>5</sub> <sup>+</sup>	C <sub>4</sub> H <sub>3</sub> <sup>+</sup>
<i>a</i>	0.05 ± 0.01	0.053 ± 0.014	—
<i>T</i> <sub>1</sub> (fs)	225 ± 41	139 ± 26	—
<i>t</i> (fs)	426 ± 10	362 ± 36	—
<i>φ</i> (rad)	−0.05 ± 0.21	2.47 ± 0.31	—
<i>b</i>	0.033 ± 0.002	−0.043 ± 0.002	−0.013 ± 0.006
<i>T</i> <sub>2</sub> (fs)	841 ± 75	808 ± 46	260 ± 160
<i>c</i>	0.12 ± 0.11	—	0.012 ± 0.006
<i>T</i> <sub>3</sub> (fs)	38 ± 37	—	960 ± 390
<i>d</i>	0.826 ± 0.001	1.212 ± 0.001	0.264 ± 0.001

Table A14: Coefficients extracted from transients at 800 nm, 10<sup>12</sup> W cm<sup>−2</sup> fitted to eq (1).

eq (1)	NB <sup>+</sup>	C <sub>6</sub> H <sub>5</sub> <sup>+</sup>	C <sub>4</sub> H <sub>3</sub> <sup>+</sup>
<i>a</i>	0.08 ± 0.01	0.20 ± 0.02	—
<i>T</i> <sub>1</sub> (fs)	244 ± 24	147 ± 12	—
<i>t</i> (fs)	439 ± 15	417 ± 19	—
<i>φ</i> (rad)	−0.13 ± 0.19	2.64 ± 0.13	—
<i>b</i>	0.085 ± 0.003	−0.126 ± 0.002	−0.157 ± 0.005
<i>T</i> <sub>2</sub> (fs)	842 ± 31	1560 ± 70	191 ± 11
<i>c</i>	0.36 ± 0.09	—	0.088 ± 0.003
<i>T</i> <sub>3</sub> (fs)	51 ± 11	—	1680 ± 110
<i>d</i>	0.364 ± 0.001	1.409 ± 0.001	0.338 ± 0.001

Table A15: Coefficients extracted from transients at 800 nm, 10<sup>13</sup> W cm<sup>−2</sup> fitted to eq (1).

## Appendix B

Link back to chapter [5](#).

### Figures

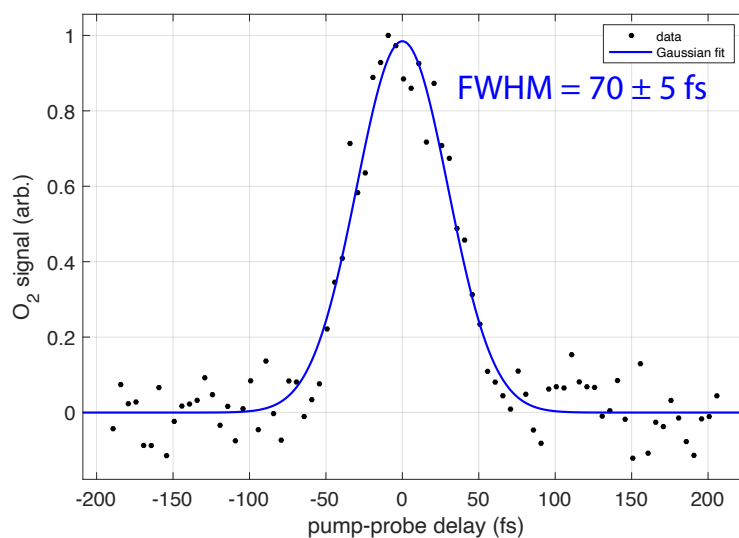


Figure B1: Ion signal of O<sub>2</sub> versus pump-probe delay with Gaussian fit. The 70 fs FWHM for the cross-correlation is taken as the width of the 400 nm probe pulse because the 1300 nm pump pulse has width of  $\sim 20$  fs.

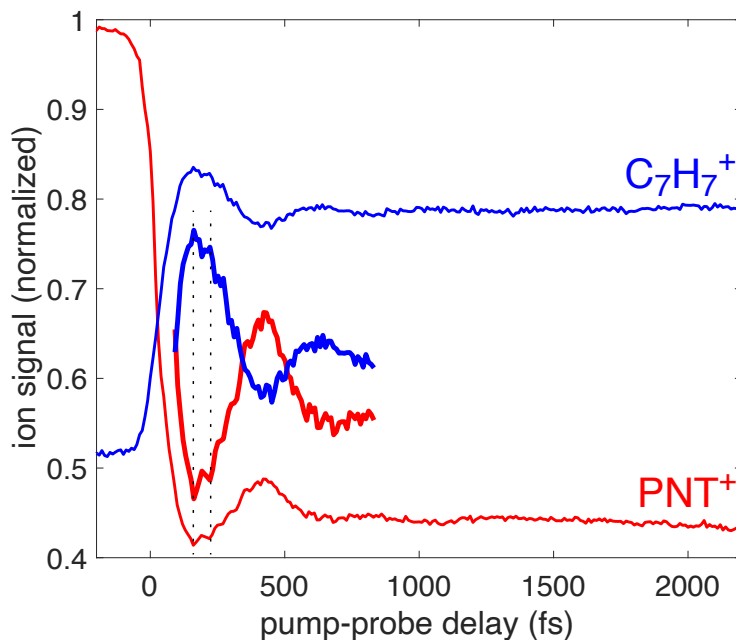


Figure B2: Transient ion signals from 1300 nm pump and 800 nm probe. The low-amplitude fast oscillations (highlighted by the magnification of ion signals and dotted lines) are less visible than using 1500 nm pump (Figures 1A and 2A).

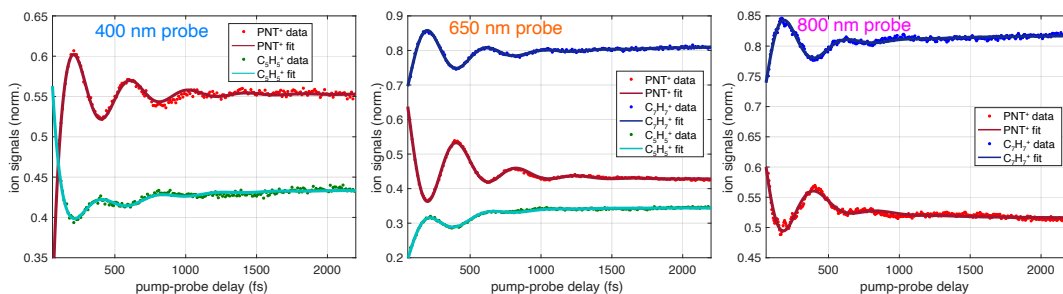


Figure B3: Transient ion signals and curve fitting to eq C.1 or B.2. Fit coefficients given in Tables S1–S3.

## Tables

All transient signals were fit to the equation

$$S(\tau) = ae^{-\tau/T_1} \cos\left(\frac{2\pi}{t}\tau + \phi\right) + be^{-\tau/T_2} + c \quad (\text{B.1})$$

with the exception of the  $\text{C}_5\text{H}_5^+$  signal for the 400 nm probe, which required one additional exponential decay term:

$$S(\tau) = ae^{-\tau/T_1} \cos\left(\frac{2\pi}{t}\tau + \phi\right) + be^{-\tau/T_2} + c + de^{-\tau/T_3} \quad (\text{B.2})$$

ion	$a$	$T_1$ (fs)	$t$ (fs)	$\phi$ (rad)	$b$	$T_2$ (fs)	$c$	$d$	$T_3$ (fs)
PNT <sup>+</sup>	$0.10 \pm 0.01$	$345 \pm 33$	$410 \pm 7$	$3.1 \pm 0.1$	$-0.8 \pm 0.6$	$32 \pm 21$	$0.553 \pm 0.001$	-	-
$\text{C}_5\text{H}_5^+$	$0.03 \pm 0.01$	$370 \pm 120$	$421 \pm 20$	$0.3 \pm 0.3$	$0.5 \pm 0.3$	$56 \pm 18$	$0.434 \pm 0.001$	$-0.05 \pm 0.01$	$470 \pm 100$

Table B1: Fit coefficients for 400 nm probe.

ion	$a$	$T_1$ (fs)	$t$ (fs)	$\phi$ (rad)	$b$	$T_2$ (fs)	$c$
PNT <sup>+</sup>	$0.25 \pm 0.01$	$308 \pm 15$	$425 \pm 4$	$0.05 \pm 0.04$	$0.1 \pm 0.01$	$445 \pm 49$	$0.427 \pm 0.002$
$\text{C}_7\text{H}_7^+$	$0.15 \pm 0.01$	$290 \pm 12$	$417 \pm 3$	$3.1 \pm 0.03$	$-0.05 \pm 0.01$	$2000 \pm 700$	$0.83 \pm 0.01$
$\text{C}_5\text{H}_5^+$	$0.09 \pm 0.01$	$252 \pm 17$	$438 \pm 9$	$3.3 \pm 0.1$	$-0.13 \pm 0.01$	$316 \pm 14$	$0.344 \pm 0.001$

Table B2: Fit coefficients for 650 nm probe.

ion	$a$	$T_1$ (fs)	$t$ (fs)	$\phi$ (rad)	$b$	$T_2$ (fs)	$c$
PNT <sup>+</sup>	$0.15 \pm 0.02$	$210 \pm 16$	$464 \pm 11$	$0.45 \pm 0.07$	$0.06 \pm 0.01$	$476 \pm 62$	$0.516 \pm 0.001$
$\text{C}_7\text{H}_7^+$	$0.13 \pm 0.01$	$212 \pm 12$	$438 \pm 7$	$3.3 \pm 0.1$	$0.035 \pm 0.002$	$682 \pm 106$	$0.818 \pm 0.001$

Table B3: Fit coefficients for 800 nm probe.

Element	X	Y	Z
C	0.041925	1.211232	-0.001089
C	-1.344135	1.200265	-0.005698
C	-2.060051	0.000000	-0.005278
C	-1.344135	-1.200265	-0.005698
C	0.041925	-1.211232	-0.001089
C	0.718977	0.000000	0.002393
H	-1.879673	2.140928	-0.012507
H	-1.879673	-2.140928	-0.012507
H	0.600068	2.134645	-0.003114
H	0.600068	-2.134645	-0.003114
N	2.191627	0.000000	0.004756
O	2.759942	1.081637	0.005917
O	2.759942	-1.081637	0.005917
C	-3.563730	0.000000	0.020795
H	-3.970858	0.883612	-0.469934
H	-3.931363	0.000000	1.050184
H	-3.970858	-0.883612	-0.469934

Table B4: Optimized geometric coordinates for neutral PNT

Element	X	Y	Z
C	0.035062	1.241740	-0.004135
C	-1.330460	1.233297	-0.014589
C	-2.055285	-0.000726	-0.017636
C	-1.331528	-1.235088	-0.007690
C	0.033997	-1.244191	-0.003338
C	0.703808	-0.001413	0.000405
H	-1.880933	2.164132	-0.020364
H	-1.882507	-2.165602	-0.011619
H	0.605342	2.159890	0.006811
H	0.603890	-2.162623	-0.010817
N	2.160385	-0.001909	0.009007
O	2.695131	0.657553	0.876098
O	2.702740	-0.662142	-0.853123
C	-3.528637	0.000282	-0.000898
H	-3.948916	0.896203	-0.456197
H	-3.861391	0.005353	1.051140
H	-3.950700	-0.897936	-0.449569

Table B5: Optimized geometric coordinates for PNT cation

Frequency (cm <sup>-1</sup> )	Intensity (a.u.)
11.06	1.98
58.96	1.31
79.68	0.58
164.31	1.22
215.71	4.76
302.93	1.40
336.83	3.45
367.52	2.13
372.00	1.73
514.15	14.06
565.45	0.28
604.32	5.20
689.17	2.88
741.16	13.70
775.10	1.18
809.57	1.56
822.64	18.64
852.58	31.74
984.91	76.45
992.00	3.15
1003.05	7.71
1021.56	0.36
1026.44	6.54
1139.26	14.17
1161.68	7.30
1218.77	52.84
1256.46	57.76
1283.82	3.40
1350.17	31.39
1360.23	128.69
1394.99	0.12
1411.79	13.61
1429.38	16.71
1478.83	146.47
1486.23	47.00
1494.06	43.95
1507.98	110.37
1657.12	89.10
2946.55	185.21
3075.05	2.47
3133.96	0.12
3201.83	0.93
3202.17	1.42
3217.16	27.27
3217.88	3.07

Table B6: Harmonic vibrational frequencies and intensities for optimized PNT cation

Element	X	Y	Z
C	-0.897345	0.686883	-1.770068
C	-1.533103	0.039917	-0.688463
C	-0.831542	-0.643580	0.327883
C	0.466437	0.645740	-1.828129
C	1.222476	-0.036716	-0.823855
C	0.531668	-0.676157	0.253261
C	2.695519	-0.055492	-0.881588
H	-1.486571	1.193360	-2.522060
H	-1.371594	-1.121723	1.133432
H	0.990699	1.128309	-2.641643
H	1.105340	-1.191331	1.011591
H	3.072678	0.036596	-1.899217
H	3.075095	0.821578	-0.330791
H	3.119074	-0.930298	-0.389807
N	-2.987829	0.082385	-0.615819
O	-3.574140	-0.793136	-1.213625
O	-3.464397	0.985419	0.035006

Table B7: Geometric coordinates for PNT cation with C–C–N–O dihedral angle of 87.4°

	B3LYP/Def2TZVPP		EOMCCSD/6-311+G*	
Transition	EE (eV)	$f$ (a.u.)	EE (eV)	$f$ (a.u.)
D <sub>0</sub> → D <sub>1</sub>	0.2223	0.0000	0.4563	0.000084
D <sub>0</sub> → D <sub>2</sub>	0.2375	0.0000	1.6238	0.000000
D <sub>0</sub> → D <sub>3</sub>	0.5579	0.0003	1.7845	0.001115
D <sub>0</sub> → D <sub>4</sub>	0.7020	0.0000	1.9550	0.000007
D <sub>0</sub> → D <sub>5</sub>	2.5512	0.0000	3.1075	0.000031
D <sub>0</sub> → D <sub>6</sub>	2.9536	0.0385	3.2137	0.064960
D <sub>0</sub> → D <sub>7</sub>	2.9625	0.0384	3.4620	0.000355

Table B8: Excitation energies (EE) and oscillator strengths ( $f$ ) for PNT cation at the neutral optimized geometry (C–C–N–O dihedral angle of 0.1°) at the B3LYP/Def2TZVPP and EOMEE-CCSD/6-311+G\* levels of theory

	B3LYP/Def2TZVPP		EOMCCSD/6-311+G*	
Transition	EE (eV)	$f$ (a.u.)	EE (eV)	$f$ (a.u.)
D <sub>0</sub> → D <sub>1</sub>	0.9244	0.0000	1.0542	0.000072
D <sub>0</sub> → D <sub>2</sub>	1.3207	0.0009	2.2312	0.001051
D <sub>0</sub> → D <sub>3</sub>	1.6492	0.0000	2.3223	0.083023
D <sub>0</sub> → D <sub>4</sub>	1.7062	0.0811	2.4925	0.000173
D <sub>0</sub> → D <sub>5</sub>	3.0109	0.0002	3.4981	0.000631
D <sub>0</sub> → D <sub>6</sub>	3.3806	0.0116	3.6250	0.006788
D <sub>0</sub> → D <sub>7</sub>	3.6314	0.0004	3.6558	0.000170

Table B9: Excitation energies (EE) and oscillator strengths ( $f$ ) for optimized PNT cation (C–C–N–O dihedral angle of 52.7°) at the B3LYP/Def2TZVPP and EOMEE-CCSD/6-311+G\* levels of theory

## Appendix C

[Link back to chapter 6.](#)

### Geometries and Excited States of ONA Neutral and Cation

Element	X	Y	Z
C	0.4319819470	-0.9926778540	0.0000002497
C	-0.2254560770	0.2571687080	-0.0000011288
C	1.8441320740	-0.9525065940	0.0000016860
C	2.5358322520	0.2321727150	0.0000004262
C	0.4906608880	1.4584852240	-0.0000027345
C	1.8628811540	1.4594119350	-0.0000013873
N	-0.1903660160	-2.1948085170	0.0000003827
H	0.3553894100	-3.0377550110	0.0000074911
H	-1.1944469480	-2.2453795690	-0.0000025625
N	-1.6725795900	0.3582043580	0.0000001972
O	-2.3327492930	-0.6789305760	-0.0000046052
O	-2.1798416000	1.4637265840	0.0000057649
H	2.3814637960	-1.8951253170	0.0000036078
H	3.6200760000	0.2100407220	0.0000018873
H	2.4111488630	2.3926613210	-0.0000032067
H	-0.0724781690	2.3810941010	-0.0000032211

Table C1: Cartesian coordinates for neutral ONA optimized at the CAM-B3LYP/6-311+G\* level.

Element	X	Y	Z
C	0.4694221212	-0.9778555500	0.0000000000
C	-0.2450409797	0.2737410798	0.0000000000
C	1.9042624592	-0.9254495831	0.0000000000
C	2.5668361022	0.2712078023	0.0000000000
C	0.4317530036	1.4546813938	0.0000000000
C	1.8425962568	1.4691716441	0.0000000000
N	-0.1246052099	-2.1545361318	0.0000000000
H	0.4154651499	-3.0115025229	0.0000000000
H	-1.1430444257	-2.2043045977	0.0000000000
N	-1.7250829616	0.3281269338	0.0000000000
O	-2.3213302049	-0.7389482214	0.0000000000
O	-2.2381721704	1.4130744390	0.0000000000
H	2.4507701463	-1.8621450423	0.0000000000
H	3.6494803843	0.2912748471	0.0000000000
H	2.3602020593	2.4206237412	0.0000000000
H	-0.1303183871	2.3801893688	0.0000000000

Table C2: Cartesian coordinates for ONA cation optimized at the CAM-B3LYP/6-311+G\* level.

	TDDFT/CAM-B3LYP/6-311+G*		EOM-CCSD/6-311+G*	
State	Energy	f	Energy	f
S1	3.7898	0.1328	3.9996	0.1487
S2	4.0879	0.0000	4.1609	0.0000
S3	4.6583	0.0005	4.7875	0.0006
S4	5.0847	0.0772	5.3369	0.0394
S5	5.6075	0.1676	5.4933	0.0049
S6	5.6486	0.0035	5.9502	0.2905
S7	5.9712	0.1385	6.1491	0.0168
S8	6.2864	0.0002	6.1870	0.0003
S9	6.4233	0.1744	6.3620	0.0061
S10	6.4990	0.0090	6.3792	0.3810

Table C3: Excited state energies and oscillator strengths for neutral ONA.

	TDDFT/CAM-B3LYP/6-311+G*		EOM-CCSD/6-311+G*	
State	Energy	f	Energy	f
D1	1.5962	0.0068	1.9351	0.0067
D2	1.9895	0.0000	2.7798	0.0000
D3	2.3554	0.0000	2.7808	0.0012
D4	2.8138	0.0000	3.2547	0.0000
D5	3.1402	0.0681	3.3802	0.0759
D6	3.5115	0.0221	3.9402	0.0000
D7	3.5602	0.0000	4.1305	0.0079
D8	4.0004	0.0010	4.5019	0.0000
D9	4.1461	0.0000	4.5185	0.0000
D10	4.2111	0.0000	4.6862	0.0001

Table C4: Excited state energies and oscillator strengths for ONA cation at the  $S_0$  geometry.

	TDDFT/CAM-B3LYP/6-311+G*		EOM-CCSD/6-311+G*	
State	Energy	f	Energy	f
D1	1.9870	0.0063	2.2734	0.0056
D2	2.4132	0.0001	3.1848	0.0022
D3	2.8956	0.0000	3.3049	0.0000
D4	3.0860	0.0000	3.5143	0.0000
D5	3.3556	0.0597	3.5572	0.0502
D6	3.8975	0.0000	4.2545	0.0000
D7	3.9256	0.0081	4.5254	0.0049
D8	4.2290	0.0087	4.7264	0.0001
D9	4.2544	0.0000	4.7271	0.0134
D10	4.5261	0.0000	4.8754	0.0564

Table C5: Excited state energies and oscillator strengths for ONA cation at the  $D_0$  geometry.

## Fit Coefficients

$$S(\tau) = ae^{-\tau^2/s^2} + bP(\tau, T_1) + cP(\tau, T_2) + d(1 + \operatorname{erf}\left(\frac{\tau}{s}\right)) + 1 + nP(\tau, T_{\text{neg}}) \quad (\text{C.1})$$

Coeff.	ONA <sup>+</sup>	C <sub>6</sub> H <sub>6</sub> N <sup>+</sup>	C <sub>5</sub> H <sub>5</sub> <sup>+</sup>	C <sub>3</sub> H <sub>3</sub> <sup>+</sup>	C <sub>6</sub> H <sub>4</sub> NO <sub>2</sub> <sup>+</sup>
<i>a</i>	0.09±0.03	0.042±0.004	0.021±0.009	0.014±0.006	0.003±0.003
<i>b</i>	0.19±0.11	-0.11±0.06	-0.15±0.04	-0.04±0.03	-0.02±0.02
<i>T</i> <sub>1</sub>	67±40	75±29	49±11	41±16	32±12
<i>c</i>	-0.19±0.15	0.08±0.07	0.08±0.02	0.018±0.004	0.003±0.001
<i>T</i> <sub>2</sub>	159±45	144±39	130±15	184±25	208±75
<i>d</i>	-0.139±0.001	0.0301±0.0002	0.0425±0.0001	0.0116±0.0001	0.0026±0.0001
<i>n</i>	0.11±0.02	0.034±0.005	0.029±0.005	0.008±0.003	0.004±0.001
<i>T</i> <sub>neg</sub>	75±10	55±5	42±4	43±10	37±7

Table C6: Coefficients extracted from curve fitting for direct dissociation pathways.

Coeff.	C <sub>6</sub> H <sub>6</sub> NO <sup>+</sup>	C <sub>5</sub> H <sub>6</sub> N <sup>+</sup>	C <sub>6</sub> H <sub>5</sub> N <sub>2</sub> O <sup>+</sup>	C <sub>6</sub> H <sub>5</sub> N <sup>+</sup>
<i>a</i>	0.016±0.002	0.016±0.002	0.003±0.002	0.002±0.002
<i>b</i>	-0.03±0.01	-0.07±0.02		-0.02±0.01
<i>T</i> <sub>1</sub>	72±52	59±23		62±50
<i>c</i>	0.02±0.02	0.03±0.03		0.02±0.02
<i>T</i> <sub>2</sub>	184±90	124±37		133±58
<i>d</i>	0.0156±0.0002	0.0118±0.0001	0.0021±0.0001	0.0072±0.0001
<i>n</i>	0.010±0.003	0.013±0.003	0.0014±0.0009	0.004±0.002
<i>T</i> <sub>neg</sub>	46±9	42±5	57±12	45±14

Table C7: Coefficients extracted from curve fitting for NNR and H transfer pathways.

## Geometries of *aci*-Rearranged ONA<sup>+</sup> Conformers

	INT1			INT2		
	X	Y	Z	X	Y	Z
C	0.449526355	-1.064457099	-0.106129515	0.489853217	-1.075049429	-0.063877767
C	-0.217371430	0.247128077	-0.028209220	-0.233241464	0.206305985	0.062682229
C	1.887008976	-1.025524606	0.031323576	1.930371111	-0.968510360	-0.129272445
C	2.580185685	0.152705856	0.103758358	2.580742000	0.231358556	-0.043786714
C	0.515392238	1.431186349	0.004608000	0.461551556	1.411038672	0.167034751
C	1.898409011	1.383052701	0.068869006	1.845956747	1.418445665	0.122194023
N	-0.064000765	-2.222006677	-0.383216473	0.007867238	-2.271766994	-0.131240543
H	-1.916692625	-1.131455864	1.140988478	-1.843950678	1.908852697	-0.795880843
H	-1.059982013	-2.212145024	-0.604025209	-1.008204462	-2.324893488	-0.075047630
N	-1.597514246	0.375616426	-0.005774473	-1.611090488	0.210771364	0.070897739
O	-2.353816744	-0.685755531	0.391908496	-2.281719110	1.383840288	-0.103835451
O	-2.200586839	1.344353762	-0.335276875	-2.301046535	-0.743921060	0.280883363
H	2.385672073	-1.986866489	0.015916746	2.461694406	-1.906343994	-0.236626150
H	3.660691242	0.142167392	0.180143196	3.662431460	0.271252158	-0.081929918
H	2.454769184	2.311181961	0.120252251	2.366930667	2.362017580	0.234444951
H	-0.005904408	2.380387418	0.028715710	-0.063988007	2.339722547	0.352347930

Table C8: Cartesian coordinates for INT1c and INT2c optimized at the CAM-B3LYP/6-311+G\* level.

	INT3			INT4		
	X	Y	Z	X	Y	Z
C	0.426543171	-1.055497790	0.037242535	0.460720643	-1.075100653	0.019408929
C	-0.228721671	0.238509438	-0.088118611	-0.220802038	0.236883209	-0.013948157
C	1.860496649	-1.014952423	0.065691061	1.908216792	-1.013039198	0.024345840
C	2.549253800	0.169585439	0.002089053	2.598680448	0.166276371	0.000503612
C	0.481260208	1.429770951	-0.146186360	0.517158361	1.422672751	-0.037470144
C	1.866960824	1.392527286	-0.106781707	1.900308943	1.386535769	-0.030381574
N	-0.302424772	-2.124278129	0.198909539	-0.035247018	-2.266397098	0.045258386
H	-1.742088302	1.797547952	0.966887628	-3.251776904	-0.471100931	-0.014519291
H	0.263355533	-2.969928290	0.280656838	-1.050926797	-2.303575823	0.041997362
N	-1.631008864	0.271169827	-0.183192069	-1.588159525	0.392623817	-0.024311099
O	-2.282496671	1.363438788	0.283606308	-2.314409096	-0.747305371	-0.004914850
O	-2.302007964	-0.563100199	-0.665413626	-2.177408669	1.440447522	-0.048771466
H	2.389603068	-1.957373800	0.153210445	2.408809637	-1.973061089	0.048821130
H	3.632396729	0.165383247	0.023885197	3.681789509	0.165626482	0.005280509
H	2.423918972	2.317633334	-0.189023697	2.447490880	2.321511027	-0.049549334
H	-0.023471161	2.376095155	-0.304449913	-0.004291532	2.370664896	-0.061845746

Table C9: Cartesian coordinates for INT3c and INT4c optimized at the CAM-B3LYP/6-311+G\* level.

	INT5			INT6		
	X	Y	Z	X	Y	Z
C	0.440932614	-1.075204253	-0.003579602	0.493221018	-1.077002573	-0.016327737
C	-0.223776125	0.232875767	0.015727799	-0.245780798	0.188879146	0.001161301
C	1.884251275	-1.030949592	-0.009620021	1.930399960	-0.954832820	0.012573528
C	2.581890478	0.144700119	0.003080894	2.556037366	0.261463217	0.025829069
C	0.513739876	1.415392894	0.028832880	0.415371433	1.414766777	0.005232376
C	1.896463003	1.373010581	0.022759125	1.800057646	1.447275861	0.018712160
N	-0.236640978	-2.179975058	-0.013755833	-0.134952252	-2.208053790	-0.089755256
H	-3.275628636	-0.404027430	0.015966088	-3.159703118	1.262994478	-0.057624631
H	0.382279970	-2.992523750	-0.026966153	0.514685624	-2.996317878	-0.097471040
N	-1.605914472	0.397129256	0.021881597	-1.633243634	0.175508712	0.010070952
O	-2.344935315	-0.707193468	0.009830040	-2.194735388	1.404868910	-0.105991002
O	-2.157057965	1.463816605	0.036890151	-2.345157135	-0.771112099	0.107316782
H	2.406442408	-1.981264603	-0.024550621	2.507143481	-1.873181571	0.012708498
H	3.665145925	0.134687767	-0.001897893	3.637808193	0.316582462	0.042678809
H	2.452126310	2.302643432	0.033289933	2.302214683	2.406892956	0.030940300
H	-0.002898346	2.365804430	0.043634875	-0.146483167	2.337676818	0.012861320

Table C10: Cartesian coordinates for INT5c and INT6c optimized at the CAM-B3LYP/6-311+G\* level.

	INT7		
	X	Y	Z
C	0.520874713	-1.075606470	0.040223201
C	-0.236186662	0.192533577	0.009260969
C	1.961109094	-0.935313278	0.029593040
C	2.578849779	0.284796346	-0.006890387
C	0.424471626	1.421809391	-0.027596426
C	1.809516143	1.460896281	-0.035434153
N	0.075539543	-2.286291499	0.075092840
H	-3.164777121	1.201473565	-0.005679151
H	-0.940092459	-2.359664445	0.081816455
N	-1.605136902	0.167866166	0.015522866
O	-2.204389503	1.378037908	-0.014361365
O	-2.302312120	-0.816507221	0.044525287
H	2.518022742	-1.863983540	0.052579411
H	3.659981663	0.350106373	-0.013973152
H	2.302632418	2.425314355	-0.064556776
H	-0.142761983	2.341777477	-0.050601066

Table C11: Cartesian coordinates for INT7c optimized at the CAM-B3LYP/6-311+G\* level.

## Pathway Energies

Species	Calc. E (Hartree)	E within pathway (Hartree)	Rel. E (eV)
ONA+ (S0)	-491.5832235	-491.5832235	0.15
ONA+ (D0)	-491.5886553	-491.5886553	0
C6H6N+	-286.4344729	-	-
NO2	-205.0612241	-	-
C6H6N+ + NO2	-491.495697	-491.495697	2.53
TS1a	-286.3405118	-491.4017359	5.09
INT1a	-286.4529953	-491.5142194	2.03
TS2a	-286.3752523	-491.4364764	4.14
TS3a	-286.3721775	-491.4334015	4.22
INT2a	-286.453014	-491.5142381	2.03
C5H5+ (triplet)	-193.0030022	-	-
HNC	-93.36579443	-	-
C5H5+ (triplet) + HNC	-286.3687966	-491.4300207	4.32
C5H5+ (singlet)	-192.9871507	-	-
C5H5+ (singlet) + HNC	-286.3529451	-491.4141692	4.75

Table C12: Direct pathway energies (E) calculated at the CAM-B3LYP/6-311+G\* level. Energies include ZPE.

Species	Calc. E (Hartree)	E within pathway (Hartree)	Rel. E (eV)
ONA+ (S0)	-491.5832235	-491.5832235	0.15
ONA+ (D0)	-491.5886553	-491.5886553	0
TS1b	-491.5075266	-491.5075266	2.21
nnr-ONA+	-491.6151207	-491.6151207	-0.72
TS2b	-491.6113184	-491.6113184	-0.62
C6H6NO+	-361.7263474	-	-
NO	-129.8825705	-	-
C6H6NO+ + NO	-491.6089179	-491.6089179	-0.55
TS3b	-361.6544785	-491.537049	1.4
INT1b	-361.6841108	-491.5666813	0.6
TS4b	-361.6599329	-491.5425034	1.26
C5H6N+	-248.3794051	-	-
CO	-113.3004769	-	-
C5H6N+ + CO	-361.679882	-491.5624525	0.71

Table C13: NNR pathway energies (E) calculated at the CAM-B3LYP/6-311+G\* level. Energies include ZPE.

Species	Calc. E (Hartree)	E within pathway (Hartree)	Rel. E (eV)
ONA+ (S0)	-491.5832235318	-491.5832235318	0.15
ONA+ (D0)	-491.5886553450	-491.5886553450	0.00
TS1c	-491.5137557821	-491.5137557821	2.04
INT1c	-491.5224392374	-491.5224392374	1.80
TS2c	-491.5229063428	-491.5229063428	1.79
INT4c	-491.5399743033	-491.5399743033	1.32
TS3c	-491.5246173211	-491.5246173211	1.74
INT5c	-491.5405814143	-491.5405814143	1.31
TS4c	-491.5265602425	-491.5265602425	1.69
INT6c	-491.5421659724	-491.5421659724	1.27
TS5c	-491.5280257237	-491.5280257237	1.65
INT7c	-491.5424793381	-491.5424793381	1.26
TS6c	-491.5108858807	-491.5108858807	2.12
C6H5N+	-285.7580626320	-	-
HONO	-205.6729629576	-	-
C6H5N+ + HONO	-491.4310255896	-491.4310255896	4.29
TS7c	-491.5044261129	-491.5044261129	2.29
INT8c	-491.5315175234	-491.5315175234	1.55
TS8c	-491.5045906773	-491.5045906773	2.29
C6H5N2O+ (singlet)	-415.7880930450	-	-
OH	-75.7202580406	-	-
C6H5N2O+ (singlet) + OH	-491.5083510857	-491.5083510857	2.19
C6H5N2O+ (triplet)	-415.7479171581	-	-
C6H5N2O+ (triplet) + OH	-491.4681751987	-491.4681751987	3.28

Table C14: H transfer pathway energies (E) calculated at the CAM-B3LYP/6-311+G\* level. Energies include ZPE.

## Vibrational Frequencies of Transition States

TS1a		TS2a		TS3a	
Frequency	Intensity	Frequency	Intensity	Frequency	Intensity
-2319.05	138.305	-699.13	112.391	-740.41	132.225
203.81	4.186	166.08	0.53	168.01	0.323
287.73	156.851	276.46	6.989	264.98	61.365
383.46	9.997	432.84	0.855	428.45	1.882
445.1	4.59	460.67	8.661	469.79	24.063
468.81	8.267	521.97	51.283	492.28	88.414
553.28	1.673	593.91	12.098	581.8	18.498
627.2	5.531	631.78	9.847	605.06	15.011
662.02	17.206	706.25	74.244	707.27	149.336
780.79	61.686	745.33	9.527	730.52	14.581
868.79	6.609	858.22	32.275	828.08	22.08
879.27	0.296	909.01	68.356	885.65	20.648
922.78	21.444	950.17	33.128	950.44	4.601
947.73	35.388	979.75	13.297	970.35	9.902
984.96	0.465	990.24	14.617	986.55	2.74
989.23	6.427	1000.01	2.131	1002.22	2.066
1035.13	0.253	1009.8	6.058	1011.96	6.683
1041.73	39.083	1074.98	224.177	1060.27	35.59
1135.92	6.702	1090.17	116.525	1102.4	103.414
1191.03	4.484	1155.82	5.165	1154.54	4.201
1270.32	12.405	1188.56	53.203	1174.71	2.904
1334.17	9.866	1304.2	11.405	1297.63	21.221
1407.76	10.906	1379.3	8.905	1366.05	8.782
1457.88	20.629	1399.7	34.093	1399.63	37.128
1524.92	10.593	1642.19	5.81	1645.88	9.241
1574.49	17.75	1671.84	5.599	1677.58	3.178
1654.65	91.473	1875.68	59.428	1858.82	117.159
1897.12	31.73	3149.98	25.788	3143.42	24.269
3221.74	0.794	3200.69	50.231	3201.06	49.556
3233.8	2.098	3210.43	12.942	3213.52	24.064
3247.88	6.111	3227.25	20.876	3229.14	35.367
3258.92	10.933	3255.56	6.714	3254.98	6.184
3542.69	310.027	3521.84	73.916	3521.36	106.138

Table C15: Harmonic frequencies ( $\text{cm}^{-1}$ ) and intensities ( $\text{km mol}^{-1}$ ) for transition states within direct pathway, calculated at the CAM-B3LYP/6-311+G\* level.

TS1b		TS2b		TS3b		TS4b	
Frequency	Intensity	Frequency	Intensity	Frequency	Intensity	Frequency	Intensity
-935.28	405.825	-92.13	279.277	-208.87	83.347	-573.53	213.36
103.09	2.521	53.97	1.593	96.44	20.719	101.92	1.689
137.92	3.948	59.83	5.571	100.68	4.718	136.36	3.365
191.33	6.047	78.62	6.876	194.8	9.699	212.42	14.97
237.93	9.663	143.07	15.412	278.88	22.662	274.39	11.034
270.14	9.073	232.08	20.01	325.45	4.249	373.56	3.553
394.67	25.129	303.32	170.409	401.8	15.098	410.02	21.531
445.82	56.883	343.28	9.331	486.2	11.502	540.62	31.225
468.94	1.045	444.5	3.57	559.71	1.159	603.42	66.162
491.51	18.413	458.22	8.469	597.45	34.004	638.96	79.998
540.92	56.444	489.18	54.046	636.96	38.822	657.2	23.663
574.88	10.264	537.42	33.136	695.83	36.289	698.24	9.09
615.61	106.966	574.94	58.266	709.98	210.757	784.68	92.779
640.51	75.073	644.25	15.352	792.96	62.685	816.88	0.956
718	9.484	717.56	144.373	847.37	48.53	851.07	15.901
739.27	2.152	748.13	37.817	922.52	21.445	921.06	18.789
778.21	87.088	767.97	51.225	959.54	18.257	1023.75	4.458
859.9	1.878	810.37	40.622	993.25	6.619	1046.13	12.879
864.21	10.461	883.48	2.835	1022.22	1.735	1060.38	4.032
990.21	31.023	890.95	1.209	1115.94	59.504	1088.57	3.587
995.88	16.016	996.32	15.67	1151.45	6.42	1104.96	39.463
1019.63	3.897	1015.4	0.958	1173.9	15.596	1119.47	40.544
1031.85	0.853	1041.92	0.328	1202.64	2.811	1292.78	36.308
1060.12	3.944	1050.01	24.093	1378.16	4.932	1344.75	85.261
1158.2	180.589	1175.72	122.785	1401	16.453	1415.77	29.198
1195.13	20.059	1211.34	135.602	1439.19	12.089	1480.79	65.505
1216.74	6.837	1251.25	35.743	1676.19	20.987	1518.72	63.402
1286.76	3.393	1386.65	1135.649	1687.44	48.955	1611.26	152.312
1396.29	14.317	1415.46	925.909	1948.7	107.352	1734.6	370.656
1434.93	23.589	1429.93	546.716	2273.66	749.246	2190.44	442.294
1471.19	40.858	1480.73	236.204	3165.67	35.214	3207.76	8.223
1549.93	168.048	1564.61	21.755	3169.22	20.345	3245.8	0.108
1581.83	115.491	1590.38	12.324	3219.66	3.276	3267.77	7.148
1646.88	495.098	1670.94	1.707	3250.62	1.414	3280.79	9.167
1652.01	21.062	1717.61	256.315	3510.21	164.943	3581.45	234.362
1731.66	255.926	2045.75	5605.121	3609.96	110.294	3690.1	88.555
3220.88	0.351	3215.32	0.436				
3231.74	0.556	3225.34	0.763				
3238.31	8.825	3233.41	1.793				
3246.69	7.209	3242.73	1.674				
3576.94	264.261	3545.32	212.973				
3685.74	70.785	3672.93	112.291				

Table C16: Harmonic frequencies ( $\text{cm}^{-1}$ ) and intensities ( $\text{km mol}^{-1}$ ) for transition states within NNR pathway, calculated at the CAM-B3LYP/6-311+G\* level.

TS1c		TS2c		TS3c		TS4c	
Frequency	Intensity	Frequency	Intensity	Frequency	Intensity	Frequency	Intensity
-561.21	430.831	-153.16	44.565	-234.54	98.744	-99.68	2.362
112.47	3.51	104.64	8.25	101.9	1.661	122.36	5.53
132.88	2.739	158.66	29.978	130.53	3.543	184.51	6.273
241.29	3.975	214.35	0.499	236.22	8.782	200.33	0.872
256.27	9.211	256.87	8.676	252.69	3.033	333.52	1.91
365.54	4.903	370.09	5.49	372.66	0.554	356.65	4.84
396.29	5.736	380.64	1.366	406.47	1.234	426.19	2.25
416.22	1.953	430.65	3.71	410.05	12.417	470.64	5.4
494.95	26.239	468.97	7.903	488.74	35.862	543.62	6.922
552.46	15.761	547.78	18.62	519.65	126.83	559.27	11.165
564.01	4.48	569.92	12.518	553.47	12.917	617.46	99.438
622.18	53.464	625.28	11.094	564.54	15.223	658.14	19.043
671.5	3.016	652.84	14.802	657.53	36.707	700.68	6.323
690.54	26.576	703.59	9.217	684.3	23.426	723.44	44.906
731.43	22.678	749.76	42.9	727.92	41.219	758.98	14.461
797.18	26.997	794.63	63.193	769.08	7.249	776.57	85.363
800.69	48.336	874.49	15.373	793.92	42.28	783.33	64.14
866.84	2.657	890.8	29.284	861.3	72.346	875.62	9.073
899.45	8.729	912.3	14.305	881.51	31.626	889.14	1.067
1012.39	3.843	1019.28	0.777	952.85	301.895	978.3	3.985
1049.23	89.845	1031.71	38.304	1016.11	1.667	1028.83	0.131
1052.1	2.472	1045.81	2.238	1051.31	0.654	1041.18	5.936
1079.59	87.401	1074.32	28.834	1054.98	9.63	1066.39	7.438
1097.51	46.112	1096.56	34.668	1101.62	184.614	1115.64	24.163
1150.82	78.909	1181.69	41.953	1157.96	84.301	1179.8	30.335
1193.99	226.717	1205.53	33.275	1206.26	185.742	1192.28	20.43
1228.55	158.014	1259.86	332.893	1243.67	335.558	1210.42	290.22
1273.79	23.379	1330.74	72.877	1277.02	131.205	1322.19	5.57
1319.29	7.193	1340.25	161.016	1320.4	72.423	1338.21	57.79
1372.2	32.432	1405.36	14.734	1401.61	13.623	1360.88	0.569
1414.94	249.974	1437.58	55.467	1444.91	24.819	1455.53	1.696
1468.94	55.693	1476.81	89.968	1488.24	37.677	1474.44	0.454
1503.91	35.691	1506.32	13.517	1517.47	91.054	1497.31	4.885
1607.17	64.997	1560.38	1.798	1598.06	112.285	1577.3	20.736
1630.76	155.17	1605.39	511.616	1661.48	299.05	1621.75	27.764
1754.89	338.416	1633.94	256.015	1720.23	341.874	1815.53	192.704
3226.64	0.526	3227.88	5.169	3223.99	0.578	3217.99	1.232
3238.05	3.61	3235.46	3.905	3239.31	0.325	3227.05	0.939
3243.25	12.766	3242.46	15.628	3242.44	8.16	3232.68	2.029
3249.55	4.747	3247.69	4.273	3253.18	7.129	3244.04	1.848
3424.96	39.493	3509.87	24.603	3473.39	68.723	3519.7	25.258
3462.88	126.599	3670.32	139.393	3639.29	336.768	3576.38	238.195

Table C17: Harmonic frequencies ( $\text{cm}^{-1}$ ) and intensities ( $\text{km mol}^{-1}$ ) for transition states within H transfer pathway, calculated at the CAM-B3LYP/6-311+G\* level (TS1c to TS4c).

TS5c		TS6c		TS7c		TS8c	
Frequency	Intensity	Frequency	Intensity	Frequency	Intensity	Frequency	Intensity
-209.11	74.444	-157.77	2.142	-591.44	99.827	-495.19	37.39
114.57	1.445	106.47	1.262	106.44	5.975	104.67	3.259
155.8	7.078	173.96	2.636	154.58	5.238	137.03	4.448
230.3	4.343	194.29	1.035	244.02	12.115	241.9	2.351
243.95	6.321	332.67	1.242	327.63	11.864	263.75	2.366
360.2	1.671	347.45	0.815	344.2	45.099	317.27	116.32
406.05	22.682	454.83	20.191	367.46	113.772	406.26	75.07
439.74	3.431	470.52	1.671	452.2	58.383	430.06	19.642
484.99	142.506	542.8	10.836	488.95	20.542	459.14	16.036
507.18	9.772	557.42	4.533	515.4	3.101	520.19	27.2
536.43	2.093	631.28	85.527	550.96	1.493	541.52	4.512
565.59	28.142	646.79	35.4	577.01	5.514	567.91	5.062
663.88	27.954	651.76	50.05	635.55	13.986	617.11	1.853
683.69	21.424	728.51	8.456	743.14	28.632	742.32	2.455
731.36	58.68	735.79	30.982	754.57	30.462	781.45	97.635
770.45	8.493	771.99	59.784	764.87	0.64	788.42	16.241
787.1	40.024	776.91	40.151	785.68	67.161	873.48	0.141
850.18	188.895	872.88	6.301	877.42	4.913	889.07	64.095
874.06	19.392	897.79	0.121	888.85	0.867	924.22	73.778
919.44	206.177	981.48	2.508	983.9	29.65	949.77	59.652
1011.51	0.796	1026.67	8.613	996.18	35.78	1011.35	2.945
1050.69	0.967	1034.73	0.197	1019.56	57.798	1015.41	9.465
1054.44	3.863	1066.42	3.464	1035.39	0.11	1032.03	38.727
1080.28	186.129	1113.17	51.295	1036.3	4.625	1049.18	12.697
1190.09	72.219	1156.94	39.591	1146.17	7.856	1049.39	4.737
1207.94	210.387	1183.92	278.965	1194.72	11.14	1171.48	3.274
1255.73	422.093	1199.95	56.206	1215.66	72.493	1198.72	17.81
1286.74	21.323	1310.9	3.548	1275.42	39.673	1291.42	13.295
1344.34	56.547	1332.31	37.76	1310.81	45.453	1327.52	29.81
1400.17	84.355	1352.59	7.703	1353.19	5.892	1362.47	1.66
1450.84	2.515	1442.36	3.54	1435.65	7.839	1429.64	33.574
1491.77	13.666	1450.08	10.217	1449.43	13.831	1453.2	16.911
1506.79	64.026	1483.04	3.283	1466.67	52.917	1479.35	24.822
1580.13	189.329	1583.15	19.458	1528.73	12.91	1577.34	16.906
1670.53	143.845	1607.08	38.501	1584.66	3.01	1641.28	34.688
1707.43	251.923	1793.21	209.539	1633.54	74.983	1666.26	27.63
3223.49	0.534	3220.22	2.51	3227.32	0.227	3227.51	0.545
3241.07	0.816	3228.52	0.229	3237.74	0.457	3239.02	1.252
3244.44	5.113	3239.53	5.056	3244.68	5.103	3248.18	5.387
3260.93	9.245	3245.19	2.885	3249.52	5.109	3257.55	7.167
3483.95	88.346	3480.23	2.765	3603.52	267.16	3615.22	344.887
3657.2	340.269	3562.34	242.508	3728.72	213.592	3727.04	125.664

Table C18: Harmonic frequencies ( $\text{cm}^{-1}$ ) and intensities ( $\text{km mol}^{-1}$ ) for transition states within H transfer pathway, calculated at the CAM-B3LYP/6-311+G\* level (TS5c to TS8c).

## Supplemental Figures

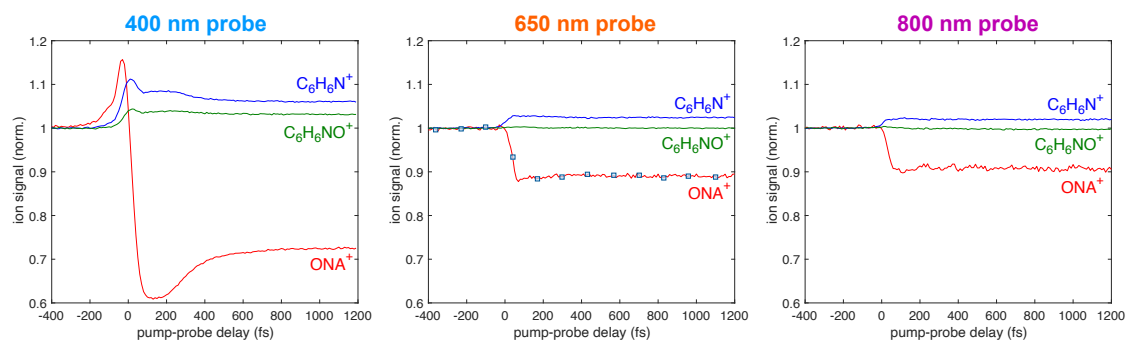


Figure C1: Transients for each probe wavelength.

# Bibliography

- [1] NIST Standard Reference Database 1A. <https://chemdata.nist.gov>, DOI: 10.18434/T4H594. Last checked 02/14/2023.
- [2] Khalil, O. S.; Meeks, J. L.; McGlynn, S. P. Electronic spectroscopy of highly polar aromatics. VII. Photoelectron spectra of nitroanilines. *Journal of the American Chemical Society* **1973**, *95*, 5876–5880.
- [3] Tibbetts, K. M. Coherent Vibrational and Dissociation Dynamics of Polyatomic Radical Cations. *Chem. Eur. J.* **2019**, *25*, 8431–8439.
- [4] Ampadu Boateng, D.; Gutsev, G. L.; Jena, P.; Tibbetts, K. M. Dissociation Dynamics of 3- and 4-Nitrotoluene Radical Cations: Coherently Driven C–NO<sub>2</sub> Bond Homolysis. *J. Chem. Phys.* **2018**, *148*, 134305.
- [5] Snow, T. P.; Bierbaum, V. M. Ion Chemistry in the Interstellar Medium. *Annu. Rev. Anal. Chem.* **2008**, *1*, 229–259.
- [6] Brédas, J.-L.; Beljonne, D.; Coropceanu, V.; Cornil, J. Charge-Transfer and Energy-Transfer Processes in  $\pi$ -Conjugated Oligomers and Polymers: A Molecular Picture. *Chem. Rev.* **2004**, *104*, 4971–5004.
- [7] Prier, C. K.; Rankic, D. A.; MacMillan, D. W. C. Visible Light Photoredox Catalysis with Transition Metal Complexes: Applications in Organic Synthesis. *Chemical reviews* **2013**, *113*, 5322–5363.
- [8] Sevilla, M. D.; Becker, D.; Kumar, A.; Adhikary, A. Gamma and Ion-Beam Irradiation of DNA: Free Radical Mechanisms, Electron Effects, and Radiation Chemical Track Structure. *Radiat. Phys. Chem.* **2016**, *128*, 60 – 74.
- [9] Han, R.-M.; Zhang, J.-P.; Skibsted, L. H. Reaction Dynamics of Flavonoids and Carotenoids as Antioxidants. *Molecules* **2012**, *17*, 2140–2160.

- [10] Kuklja, M. M.; Tsyshevsky, R. V.; Sharia, O. Effect of Polar Surfaces on Decomposition of Molecular Materials. *J. Am. Chem. Soc.* **2014**, *136*, 13289–13302.
- [11] Sikder, A.; Sikder, N. A Review of Advanced High Performance, Insensitive and Thermally Stable Energetic Materials Emerging for Military and Space Applications. *J. Hazard. Mater.* **2004**, *112*, 1 – 15.
- [12] Wharton, R.; Formby, S.; Merrifield, R. Airblast TNT equivalence for a range of commercial blasting explosives. *J. Hazard. Mater.* **2000**, *79*, 31 – 39.
- [13] Field, J. E.; Swallowe, G. M.; Heavens, S. N. Ignition Mechanisms of Explosives during Mechanical Deformation. *Proc. Royal Soc. A* **1982**, *382*, 231–244.
- [14] Tarver, C. M.; Kury, J. W.; Breithaupt, R. D. Detonation waves in triaminotrinitrobenzene. *J. Appl. Phys.* **1997**, *82*, 3771–3782.
- [15] Dremin, A. N. Discoveries in Detonation of Molecular Condensed Explosives in the 20th Century. *Combustion, Explosion and Shock Waves* **2000**, *36*, 704–715.
- [16] Ramaswamy, A. L. Microscopic initiation mechanisms in energetic material crystals. *Journal of Energetic Materials* **2001**, *19*, 195–217.
- [17] Cohen, R.; Zeiri, Y.; Wurzburg, E.; Kosloff, R. Mechanism of Thermal Unimolecular Decomposition of TNT (2,4,6-Trinitrotoluene): A DFT Study. *J. Phys. Chem. A* **2007**, *111*, 11074–11083.
- [18] Jeilani, Y. A.; Duncan, K. A.; Newallo, D. S.; Thompson, A. N.; Bose, N. K. Tandem mass spectrometry and density functional theory of RDX fragmentation pathways: Role of ion–molecule complexes in loss of NO<sub>3</sub> and lack of molecular ion peak. *Rapid Commun. Mass Spectrom.* **2015**, *29*, 802–810.
- [19] Zeng, Z.; Bernstein, E. R. Photoelectron spectroscopy and density functional theory studies of N-rich energetic materials. *J. Chem. Phys.* **2016**, *145*, 164302.
- [20] Yuan, B.; Yu, Z.; Bernstein, E. R. Initial Mechanisms for the Decomposition of Electronically Excited Energetic Salts: TKX-50 and MAD-X1. *J. Phys. Chem. A* **2015**, *119*, 2965–2981.

- [21] Yuan, B.; Bernstein, E. R. Initial mechanisms for the unimolecular decomposition of electronically excited nitrogen-rich energetic materials with tetrazole rings: 1-DTE, 5-DTE, BTA, and BTH. *J. Chem. Phys.* **2016**, *144*, 234302.
- [22] Yuan, B.; Bernstein, E. R. Initial mechanisms for the unimolecular decomposition of electronically excited bisfuroxan based energetic materials. *J. Chem. Phys.* **2017**, *146*, 014301.
- [23] Zink, J. I.; Kaska, W. C. Triboluminescence of hexaphenylcarbodiphosphorane. Emission from a molecular excited state populated by mechanical stress. *J. Am. Chem. Soc.* **1973**, *95*, 7510–7512.
- [24] Lin, S. H.; Wutz, D.; Ho, Z. Z.; Eyring, H. Mechanisms of triboluminescence. *Proc. Nat. Acad. Sci.* **1980**, *77*, 1245–1247.
- [25] Bowden, M. D.; Cheeseman, M.; Knowles, S. L.; Drake, R. C. Laser initiation of energetic materials: a historical overview. *Proc. SPIE*. 2007; pp 666208–666208–12.
- [26] Matsika, S.; Krause, P. Nonadiabatic Events and Conical Intersections. *Annu. Rev. Phys. Chem.* **2011**, *62*, 621–643.
- [27] Weinacht, T. *Time-resolved spectroscopy : an experimental perspective*; Textbook series in physical sciences; CRC Press, Taylor Francis Group: Boca Raton, 2019.
- [28] Ohmori, K. Wave-Packet and Coherent Control Dynamics. *Annual Review of Physical Chemistry* **2009**, *60*, 487–511, PMID: 19335221.
- [29] Tannor, D. J. *Introduction to quantum mechanics : a time-dependent perspective*; 2007.
- [30] Dantus, M.; Bowman, R. M.; Zewail, A. H. Femtosecond laser observations of molecular vibration and rotation. *Nature (London)* **1990**, *343*, 737–739.
- [31] Wu, X.; Su, P. In *Quantum Chemistry in the age of machine learning*; Dral, P. O., Ed.; Elsevier, 2022; p 3–25.
- [32] Jensen, F. *Introduction to computational chemistry*, 3rd ed.; John Wiley Sons: Chichester, UK, 2017.

- [33] Hohenberg, P.; Kohn, W. Inhomogeneous Electron Gas. *Phys. Rev.* **1964**, *136*, B864–B871.
- [34] Kohn, W.; Sham, L. J. Self-Consistent Equations Including Exchange and Correlation Effects. *Phys. Rev.* **1965**, *140*, A1133–A1138.
- [35] Dirac, P. A. M. Note on Exchange Phenomena in the Thomas Atom. *Mathematical Proceedings of the Cambridge Philosophical Society* **1930**, *26*, 376–385.
- [36] Perdew, J. P.; Schmidt, K. Jacob’s ladder of density functional approximations for the exchange-correlation energy. *AIP Conference Proceedings* **2001**, *577*, 1–20.
- [37] Tal, Y.; Bader, R. F. W. Studies of the energy density functional approach. I. Kinetic energy. *International Journal of Quantum Chemistry* **1978**, *14*, 153–168.
- [38] Perdew, J. P.; Yue, W. Accurate and simple density functional for the electronic exchange energy: Generalized gradient approximation. *Phys. Rev. B* **1986**, *33*, 8800–8802.
- [39] Becke, A. D. Density-functional exchange-energy approximation with correct asymptotic behavior. *Phys. Rev. A* **1988**, *38*, 3098–3100.
- [40] Lee, C.; Yang, W.; Parr, R. G. Development of the Colle-Salvetti correlation-energy formula into a functional of the electron density. *Phys. Rev. B* **1988**, *37*, 785–789.
- [41] Perdew, J. P.; Wang, Y. Accurate and simple analytic representation of the electron-gas correlation energy. *Phys. Rev. B* **1992**, *45*, 13244–13249.
- [42] Becke, A. D. Density-functional thermochemistry. III. The role of exact exchange. *The Journal of Chemical Physics* **1993**, *98*, 5648–5652.
- [43] Stephens, P. J.; Devlin, F. J.; Chabalowski, C. F.; Frisch, M. J. Ab Initio Calculation of Vibrational Absorption and Circular Dichroism Spectra Using Density Functional Force Fields. *The Journal of Physical Chemistry* **1994**, *98*, 11623–11627.
- [44] Tsuneda, T.; Hirao, K. Long-range correction for density functional theory. *WIREs Computational Molecular Science* **2014**, *4*, 375–390.

- [45] Yanai, T.; Tew, D. P.; Handy, N. C. A new hybrid exchange–correlation functional using the Coulomb-attenuating method (CAM-B3LYP). *Chemical Physics Letters* **2004**, *393*, 51–57.
- [46] Chai, J.-D.; Head-Gordon, M. Systematic optimization of long-range corrected hybrid density functionals. *The Journal of Chemical Physics* **2008**, *128*, 084106.
- [47] Klimeš, J.; Michaelides, A. Perspective: Advances and challenges in treating van der Waals dispersion forces in density functional theory. *The Journal of Chemical Physics* **2012**, *137*, 120901.
- [48] Grimme, S.; Antony, J.; Ehrlich, S.; Krieg, H. A consistent and accurate ab initio parametrization of density functional dispersion correction (DFT-D) for the 94 elements H-Pu. *The Journal of Chemical Physics* **2010**, *132*, 154104.
- [49] Ullrich, C. A. *Time-dependent density-functional theory : concepts and applications*; Oxford graduate texts; Oxford University Press: Oxford ;, 2012.
- [50] Runge, E.; Gross, E. K. U. Density-Functional Theory for Time-Dependent Systems. *Phys. Rev. Lett.* **1984**, *52*, 997–1000.
- [51] López Peña, H. A.; Ampadu Boateng, D.; McPherson, S. L.; Tibbetts, K. M. Using computational chemistry to design pump–probe schemes for measuring nitrobenzene radical cation dynamics. *Phys. Chem. Chem. Phys.* **2021**, *23*, 13338–13348.
- [52] Reed, E. J. Electron-Ion Coupling in Shocked Energetic Materials. *J. Phys. Chem. C* **2012**, *116*, 2205–2211.
- [53] Snow, T. P.; Le Page, V.; Keheyan, Y.; Bierbaum, V. M. The Interstellar Chemistry of PAH Cations. *Nature* **1998**, *391*, 259–260.
- [54] Ledingham, K.; Singhal, R. High Intensity Laser Mass Spectrometry — a Review. *Int. J. Mass Spectrom. Ion Process.* **1997**, *163*, 149 – 168.
- [55] Lezius, M.; Blanchet, V.; Rayner, D. M.; Villeneuve, D. M.; Stolow, A.; Ivanov, M. Y. Nonadiabatic Multielectron Dynamics in Strong Field Molecular Ionization. *Phys. Rev. Lett.* **2001**, *86*, 51–54.

- [56] Lezius, M.; Blanchet, V.; Ivanov, M. Y.; Stolow, A. Polyatomic Molecules in Strong Laser Fields: Nonadiabatic Multielectron Dynamics. *J. Chem. Phys.* **2002**, *117*, 1575–1588.
- [57] Yatsushashi, T.; Nakashima, N. Effects of Polarization of 1.4  $\mu\text{m}$  Femtosecond Laser Pulses on the Formation and Fragmentation of Naphthalene Molecular Ions Compared at the Same Effective Ionization Intensity. *J. Phys. Chem. A* **2005**, *109*, 9414–9418.
- [58] Bohinski, T.; Tibbetts, K. M.; Tarazkar, M.; Romanov, D.; Matsika, S.; Levis, R. J. Measurement of an Electronic Resonance in a Ground-State, Gas-Phase Acetophenone Cation via Strong-Field Mass Spectrometry. *J. Phys. Chem. Lett.* **2013**, *4*, 1587–1591.
- [59] Bohinski, T.; Tibbetts, K. M.; Tarazkar, M.; Romanov, D.; Matsika, S.; Levis, R. Measurement of Ionic Resonances in Alkyl Phenyl Ketone Cations via Infrared Strong Field Mass Spectrometry. *J. Phys. Chem. A* **2013**, *117*, 12374–12381.
- [60] Bohinski, T.; Tibbetts, K. M.; Munkerup, K.; Tarazkar, M.; Romanov, D. A.; Matsika, S.; Levis, R. J. Radical Cation Spectroscopy of Substituted Alkyl Phenyl Ketones via Tunnel Ionization. *Chem. Phys.* **2014**, *442*, 81 – 85.
- [61] Tibbetts, K. M.; Bohinski, T.; Munkerup, K.; Tarazkar, M.; Levis, R. Controlling Dissociation of Alkyl Phenyl Ketone Radical Cations in the Strong-Field Regime through Hydroxyl Substitution Position. *J. Phys. Chem. A* **2014**, *118*, 8170–8176.
- [62] Itakura, R.; Watanabe, J.; Hishikawa, A.; Yamanouchi, K. Ionization and Fragmentation Dynamics of Benzene in Intense Laser Fields by Tandem Mass Spectroscopy. *J. Chem. Phys.* **2001**, *114*, 5598–5606.
- [63] Harada, H.; Shimizu, S.; Yatsushashi, T.; Sakabe, S.; Izawa, Y.; Nakashima, N. A Key Factor in Parent and Fragment Ion Formation on Irradiation with an Intense Femtosecond Laser Pulse. *Chem. Phys. Lett.* **2001**, *342*, 563 – 570.
- [64] Trushin, S. A.; Fuß, W.; Schmid, W. E. Dissociative Ionization at High Laser Intensities: Importance of Resonances and Relaxation for Fragmentation. *J. Phys. B: At. Opt. Mol. Phys.* **2004**, *37*, 3987–4011.

- [65] Wu, D.; Wang, Q.; Cheng, X.; Jin, M.; Li, X.; Hu, Z.; Ding, D. Effect of Cation Absorption on Ionization/Dissociation of Cycloketone Molecules in a Femtosecond Laser Field. *J. Phys. Chem. A* **2007**, *111*, 9494–9498.
- [66] Pearson, B.; Nichols, S.; Weinacht, T. Molecular Fragmentation Driven by Ultrafast Dynamic Ionic Resonances. *J. Chem. Phys.* **2007**, *127*, 131101.
- [67] Nichols, S.; Weinacht, T.; Rozgonyi, T.; Pearson, B. Strong-Field Phase-Dependent Molecular Dissociation. *Phys. Rev. A* **2009**, *79*, 043407.
- [68] Gonzalez-Vazquez, J.; Gonzalez, L.; Nichols, S. R.; Weinacht, T. C.; Rozgonyi, T. Exploring Wavepacket Dynamics Behind Strong-Field Momentum-Dependent Photodissociation in CH<sub>2</sub>BrI<sup>+</sup>. *Phys. Chem. Chem. Phys.* **2010**, *12*, 14203–14216.
- [69] Zhu, X.; Lozovoy, V. V.; Shah, J. D.; Dantus, M. Photodissociation Dynamics of Acetophenone and Its Derivatives with Intense Nonresonant Femtosecond Pulses. *J. Phys. Chem. A* **2011**, *115*, 1305–1312.
- [70] Konar, A.; Shu, Y.; Lozovoy, V. V.; Jackson, J. E.; Levine, B. G.; Dantus, M. Polyatomic Molecules under Intense Femtosecond Laser Irradiation. *J. Phys. Chem. A* **2014**, *118*, 11433–11450.
- [71] Bohinski, T.; Tibbetts, K. M.; Tarazkar, M.; Romanov, D. A.; Matsika, S.; Levis, R. J. Strong Field Adiabatic Ionization Prepares a Launch State for Coherent Control. *J. Phys. Chem. Lett.* **2014**, *5*, 4305–4309.
- [72] Tibbetts, K. M.; Tarazkar, M.; Bohinski, T.; Romanov, D. A.; Matsika, S.; Levis, R. J. Controlling the Dissociation Dynamics of Acetophenone Radical Cation Through Excitation of Ground and Excited State Wavepackets. *J. Phys. B: At. Opt. Mol. Phys.* **2015**, *48*, 164002.
- [73] Ampadu Boateng, D.; Gutsev, G. L.; Jena, P.; Tibbetts, K. M. Ultrafast Coherent Vibrational Dynamics in Dimethyl Methylphosphonate Radical Cation. *Phys. Chem. Chem. Phys.* **2018**, *20*, 4636–4640.
- [74] Ampadu Boateng, D.; Word, M. D.; Tibbetts, K. M. Probing Coherent Vibrations of Organic Phosphonate Radical Cations with Femtosecond Time-Resolved Mass Spectrometry. *Molecules* **2019**, *24*, 509.

- [75] Munkerup, K.; Romanov, D.; Bohinski, T.; Stephansen, A. B.; Levis, R. J.; Sølling, T. I. Conserving Coherence and Storing Energy during Internal Conversion: Photoinduced Dynamics of cis- and trans-Azobenzene Radical Cations. *J. Phys. Chem. A* **2017**, *121*, 8642–8651.
- [76] Ho, J.-W.; Chen, W.-K.; Cheng, P.-Y. Femtosecond Pump-Probe Photoionization-Photofragmentation Spectroscopy: Photoionization-Induced Twisting and Coherent Vibrational Motion of Azobenzene Cation. *J. Chem. Phys.* **2009**, *131*, 134308.
- [77] Ampadu Boateng, D.; Word, M. D.; Gutsev, L. G.; Jena, P.; Tibbetts, K. M. Conserved Vibrational Coherence in the Ultrafast Rearrangement of 2-Nitrotoluene Radical Cation. *J. Phys. Chem. A* **2019**, *123*, 1140–1152.
- [78] Brogaard, R. Y.; Møller, K. B.; Sølling, T. I. Real-Time Probing of Structural Dynamics by Interaction between Chromophores. *J. Phys. Chem. A* **2011**, *115*, 12120–12125.
- [79] Zuo, W.; Yin, H.; Liu, X.; Lv, H.; Zhao, L.; Shi, Y.; Yan, B.; Jin, M.; Ding, D.; Xu, H. Identification of the Cationic Excited State of Cyclopentanone via Time-Resolved Ion Yield Measurements. *Chem. Phys. Lett.* **2016**, *654*, 18 – 22.
- [80] Zhou, L.; Liu, Y.; Sun, T.; Feng, S.; Lv, H.; Xu, H. Ultrafast Evolution of B2E2g - X2E1g Conical Intersection of Benzene Cations by Strong Field Ionization-Photo Fragmentation. *J. Phys. Chem. A* **2019**, *123*, 8365–8369.
- [81] Shen, C.-C.; Tsai, T.-T.; Ho, J.-W.; Chen, Y.-W.; Cheng, P.-Y. Communication: Ultrafast Time-Resolved Ion Photofragmentation Spectroscopy of Photoionization-Induced Proton Transfer in Phenol-Ammonia Complex. *J. Chem. Phys.* **2014**, *141*, 171103.
- [82] Shen, C.-C.; Tsai, T.-T.; Wu, J.-Y.; Ho, J.-W.; Chen, Y.-W.; Cheng, P.-Y. Watching Proton Transfer in Real Time: Ultrafast Photoionization-Induced Proton Transfer in Phenol-Ammonia Complex Cation. *J. Chem. Phys.* **2017**, *147*, 164302.
- [83] Wu, J.-Y.; Cheng, P.-Y. Ultrafast Protonation of an Amide: Photoionization-Induced Proton Transfer in Phenol-Dimethylformamide Complex Cation. *J. Phys. Chem. A* **2019**, *123*, 10700–10713.

- [84] Studzinski, H.; Zhang, S.; Wang, Y.; Temps, F. Ultrafast Nonradiative Dynamics in Electronically Excited Hexafluorobenzene by Femtosecond Time-Resolved Mass Spectrometry. *J. Chem. Phys.* **2008**, *128*, 164314.
- [85] Trushin, S.; Kosma, K.; Fuß, W.; Schmid, W. Wavelength-Independent Ultrafast Dynamics and Coherent Oscillation of a Metal–Carbon Stretch Vibration in Photodissociation of  $\text{Cr}(\text{CO})_6$  in the Region of 270–345 nm. *Chem. Phys.* **2008**, *347*, 309 – 323.
- [86] Kosma, K.; Trushin, S. A.; Fuß, W.; Schmid, W. E.; Schneider, B. M. R. Photodissociation of Group-6 Hexacarbonyls: Observation of Coherent Oscillations in an Antisymmetric (Pseudorotation) Vibration in  $\text{Mo}(\text{CO})_5$  and  $\text{W}(\text{CO})_5$ . *Phys. Chem. Chem. Phys.* **2010**, *12*, 13197–13214.
- [87] Montero, R.; Conde, Á. P.; Ovejas, V.; Fernández-Fernández, M.; Castaño, F.; Longarte, A. Ultrafast Evolution of Imidazole after Electronic Excitation. *J. Phys. Chem. A* **2012**, *116*, 10752–10758.
- [88] Montero, R.; Peralta Conde, Á.; Ovejas, V.; Fernández-Fernández, M.; Castaño, F.; Vázquez de Aldana, J. R.; Longarte, A. Femtosecond Evolution of the Pyrrole Molecule Excited in the Near Part of its UV Spectrum. *J. Chem. Phys.* **2012**, *137*, 064317.
- [89] Green, J. A.; Makhov, D. V.; Cole-Filipiak, N. C.; Symonds, C.; Stavros, V. G.; Shalashilin, D. V. Ultrafast Photodissociation Dynamics of 2-Ethylpyrrole: Adding Insight to Experiment with Ab Initio Multiple Cloning. *Phys. Chem. Chem. Phys.* **2019**, *21*, 3832–3841.
- [90] Tasker, A. D.; Robson, L.; Ledingham, K. W. D.; McCanny, T.; Hankin, S. M.; McKenna, P.; Kosmidis, C.; Jaroszynski, D. A.; Jones, D. R. A High Mass Resolution Study of the Interaction of Aromatic and Nitro-Aromatic Molecules with Intense Laser Fields. *J. Phys. Chem. A* **2002**, *106*, 4005–4013.
- [91] Mullen, C.; Coggiola, M. J.; Oser, H. Femtosecond Laser Photoionization Time-of-Flight Mass Spectrometry of Nitro-Aromatic Explosives and Explosives Related Compounds. *J. Am. Soc. Mass Spectrom.* **2009**, *20*, 419–429.

- [92] Scarborough, T. D.; McAcy, C. J.; Beck, J.; Uiterwaal, C. J. G. J. Comparison of Ultrafast Intense-Field Photodynamics in Aniline and Nitrobenzene: Stability Under Amino and Nitro Substitution. *Phys. Chem. Chem. Phys.* **2019**, *21*, 6553–6558.
- [93] Kosmidis, C.; Ledingham, K. W. D.; Kilic, H. S.; McCanny, T.; Singhal, R. P.; Langley, A. J.; Shaikh, W. On the Fragmentation of Nitrobenzene and Nitrotoluenes Induced by a Femtosecond Laser at 375 nm. *J. Phys. Chem. A* **1997**, *101*, 2264–2270.
- [94] Frisch, M. J. et al. Gaussian 16 Revision C.01. 2016; Gaussian Inc. Wallingford CT.
- [95] Burke, K.; Perdew, J. P.; Wang, Y. In *Electronic Density Functional Theory: Recent Progress and New Directions*; Dobson, J. F., Vignale, G., Das, M. P., Eds.; Springer US: New York, 1998; pp 81–111.
- [96] Krishnan, R.; Binkley, J. S.; Seeger, R.; Pople, J. A. Self-Consistent Molecular Orbital Methods. XX. A Basis Set for Correlated Wave Functions. *J. Chem. Phys.* **1980**, *72*, 650–654.
- [97] Zhao, Y.; Zhao, Y.; Truhlar, D. G.; Truhlar, D. G. The M06 suite of density functionals for main group thermochemistry, thermochemical kinetics, noncovalent interactions, excited states, and transition elements: two new functionals and systematic testing of four M06-class functionals and 12 other functionals. *Theoretical chemistry accounts* **2008**, *120*, 215–241.
- [98] Montgomery, J. A.; Frisch, M. J.; Ochterski, J. W.; Petersson, G. A. A Complete Basis Set Model Chemistry. VI. Use of Density Functional Geometries and Frequencies. *J. Chem. Phys.* **1999**, *110*, 2822–2827.
- [99] Dunning, T. H. Gaussian Basis Sets for Use in Correlated Molecular Calculations. I. The Atoms Boron Through Neon and Hydrogen. *J. Chem. Phys.* **1989**, *90*, 1007–1023.
- [100] Weigend, F.; Ahlrichs, R. Balanced Basis Sets of Split Valence, Triple Zeta Valence and Quadruple Zeta Valence Quality for H to Rn: Design and Assessment of Accuracy. *Phys. Chem. Chem. Phys.* **2005**, *7*, 3297–3305.

- [101] McLafferty, F. W.; Bente, P. F.; Kornfeld, R.; Tsai, S.-C.; Howe, I. Metastable Ion Characteristics. XXII. Collisional Activation Spectra of Organic Ions. *J. Am. Chem. Soc.* **1973**, *95*, 2120–2129.
- [102] Rabalais, J. W. Photoelectron Spectroscopic Investigation of the Electronic Structure of Nitromethane and Nitrobenzene. *J. Chem. Phys.* **1972**, *57*, 960–967.
- [103] Krylov, A. I. Equation-of-Motion Coupled-Cluster Methods for Open-Shell and Electronically Excited Species: The Hitchhiker's Guide to Fock Space. *Annual Review of Physical Chemistry* **2008**, *59*, 433–462, PMID: 18173379.
- [104] Shao, Y. et al. Advances in molecular quantum chemistry contained in the Q-Chem 4 program package. *Molecular Physics* **2015**, *113*, 184–215.
- [105] <http://webbook.nist.gov/chemistry/>. Last checked 7/17/20.
- [106] Bauernschmitt, R.; Ahlrichs, R. Treatment of Electronic Excitations Within the Adiabatic Approximation of Time Dependent Density Functional Theory. *Chem. Phys. Lett.* **1996**, *256*, 454 – 464.
- [107] Ampadu Boateng, D.; Tibbetts, K. M. Measurement of Ultrafast Vibrational Coherences in Polyatomic Radical Cations with Strong-Field Adiabatic Ionization. *JoVE* **2018**, *138*, e58263.
- [108] Gutsev, G. L.; Ampadu Boateng, D.; Jena, P.; Tibbetts, K. M. A Theoretical and Mass-Spectrometry Study of Dimethyl Methylphosphonate: New Isomers and Cation Decay Channels in an Intense Femtosecond Laser Field. *J. Phys. Chem. A* **2017**, *121*, 8414–8424.
- [109] Rose, T. S.; Rosker, M. J.; Zewail, A. H. Femtosecond real-time probing of reactions. IV. The reactions of alkali halides. *J. Chem. Phys.* **1989**, *91*, 7415–7436.
- [110] Nishimura, T.; Das, P. R.; Meisels, G. G. On the dissociation dynamics of energy-selected nitrobenzene ion. *J. Chem. Phys.* **1986**, *84*, 6190–6199.
- [111] Grimme, S.; Parac, M. Substantial Errors from Time-Dependent Density Functional Theory for the Calculation of Excited States of Large Systems. *ChemPhysChem* **2003**, *4*, 292–295.

- [112] Lopata, K.; Reslan, R.; Kowalska, M.; Neuhauser, D.; Govind, N.; Kowalski, K. Excited-State Studies of Polyacenes: A Comparative Picture Using EOMCCSD, CR-EOMCCSD(T), Range-Separated (LR/RT)-TDDFT, TD-PM3, and TD-ZINDO. *Journal of Chemical Theory and Computation* **2011**, *7*, 3686–3693, PMID: 26598263.
- [113] Prlj, A.; Curchod, B. F. E.; Fabrizio, A.; Floryan, L.; Corminboeuf, C. Qualitatively Incorrect Features in the TDDFT Spectrum of Thiophene-Based Compounds. *The Journal of Physical Chemistry Letters* **2015**, *6*, 13–21, PMID: 26263085.
- [114] Prlj, A.; Sandoval-Salinas, M. E.; Casanova, D.; Jacquemin, D.; Corminboeuf, C. Low-Lying \* States of Heteroaromatic Molecules: A Challenge for Excited State Methods. *Journal of Chemical Theory and Computation* **2016**, *12*, 2652–2660, PMID: 27144975.
- [115] Acharya, A.; Chaudhuri, S.; Batista, V. S. Can TDDFT Describe Excited Electronic States of Naphthol Photoacids? A Closer Look with EOM-CCSD. *Journal of Chemical Theory and Computation* **2018**, *14*, 867–876, PMID: 29298059.
- [116] López Peña, H. A.; Shusterman, J. M.; Ampadu Boateng, D.; Lao, K. U.; Tibbetts, K. M. Coherent Control of Molecular Dissociation by Selective Excitation of Nuclear Wave Packets. *Frontiers in Chemistry* **2022**, *10*.
- [117] Bloembergen, N.; Yablanovitch, E. Infrared laser induced unimolecular reactions. *Phys. Today* **1978**, *31*, 23–30.
- [118] Bloembergen, N.; Zewail, A. H. Energy Redistribution In Isolated Molecules and the Question of Mode-Selective Laser Chemistry Revisited. *The Journal of Physical Chemistry* **1984**, *88*, 5459–5465.
- [119] Judson, R. S.; Rabitz, H. Teaching lasers to control molecules. *Phys. Rev. Lett.* **1992**, *68*, 1500–1503.
- [120] Assion, A.; Baumert, T.; Bergt, M.; Brixner, T.; Kiefer, B.; Seyfried, V.; Strehle, M.; Gerber, G. Control of Chemical Reactions by Feedback-Optimized Phase-Shaped Femtosecond Laser Pulses. *Science* **1998**, *282*, 919–922.

- [121] Damrauer, N.; Dietl, C.; Krampert, G.; Lee, S.-H.; Jung, K.-H.; Gerber, G. Control of bond-selective photochemistry in  $\text{CH}_2\text{BrCl}$  using adaptive femtosecond pulse shaping. *Eur. Phys. J. D* **2002**, *20*, 71–76.
- [122] Langhojer, F.; Cardoza, D.; Baertschy, M.; Weinacht, T. Gaining mechanistic insight from closed loop learning control: The importance of basis in searching the phase space. *The Journal of Chemical Physics* **2005**, *122*, 014102.
- [123] Plenge, J.; Wirsing, A.; Wagner-Drebenstedt, I.; Halfpap, I.; Kieling, B.; Wassermann, B.; Rühl, E. Coherent control of the ultrafast dissociative ionization dynamics of bromochloroalkanes. *Phys. Chem. Chem. Phys.* **2011**, *13*, 8705–8714.
- [124] Tibbetts, K. M.; Xing, X.; Rabitz, H. Systematic Trends in Photonic Reagent Induced Reactions in a Homologous Chemical Family. *J. Phys. Chem. A* **2013**, *117*, 8205–8215.
- [125] Cardoza, D.; Pearson, B. J.; Baertschy, M.; Weinacht, T. Charge-transfer as a mechanism for controlling molecular fragmentation. *Journal of Photochemistry and Photobiology A: Chemistry* **2006**, *180*, 277–281.
- [126] Lozovoy, V. V.; Zhu, X.; Gunaratne, T. C.; Harris, D. A.; Shane, J. C.; Dantus, M. Control of Molecular Fragmentation Using Shaped Femtosecond Pulses. *J. Phys. Chem. A* **2008**, *112*, 3789–3812.
- [127] Xing, X.; Rey-de Castro, R.; Rabitz, H. Gaining Mechanistic Insight with Control Pulse Slicing: Application to the Dissociative Ionization of  $\text{CH}_2\text{BrI}$ . *J. Phys. Chem. A* **2017**, *121*, 8632–8641.
- [128] Tannor, D. J.; Rice, S. A. Control of selectivity of chemical reaction via control of wave packet evolution. *The Journal of Chemical Physics* **1985**, *83*, 5013–5018.
- [129] Zewail, A. H. Laser Femtochemistry. *Science* **1988**, *242*, 1645–1653.
- [130] Frisch, M. J. et al. Gaussian 16 Revision C.01. 2016; Gaussian Inc. Wallingford CT.
- [131] Weigend, F.; Ahlrichs, R. Balanced basis sets of split valence, triple zeta valence and quadruple zeta valence quality for H to Rn: Design and assessment of accuracy. *Phys. Chem. Chem. Phys.* **2005**, *7*, 3297–3305.

- [132] Shao, Y.; Gan, Z.; Epifanovsky, E.; Gilbert, A.T.B.; Wormit, M. Kussmann, J.; Lange, A.W.; Behn, A.; Deng, J.; Feng, X.; et al., Advances in Molecular Quantum Chemistry Contained in the Q-Chem 4 Program Package. *Mol. Phys.* **2015**, *113*, 184–215.
- [133] Kraus, P. M.; Mignolet, B.; Baykusheva, D.; Rupenyan, A.; Horný, L.; Penka, E. F.; Grassi, G.; Tolstikhin, O. I.; Schneider, J.; Jensen, F.; Madsen, L. B.; Bandrauk, A. D.; Remacle, F.; Wörner, H. J. Measurement and laser control of attosecond charge migration in ionized iodoacetylene. *Science* **2015**, *350*, 790–795.
- [134] Cristian, A.-M. C.; Krylov, A. I. Electronic structure of the  $\pi$ -bonded Al–C<sub>2</sub>H<sub>4</sub> complex: Characterization of the ground and low-lying excited states. *The Journal of Chemical Physics* **2003**, *118*, 10912–10918.
- [135] Laurent, A. D.; Blondel, A.; Jacquemin, D. Choosing an atomic basis set for TD-DFT, SOPPA, ADC, CC2 and EOM-CCSD calculations of low-lying excited states of organic dyes. *Theoretical chemistry accounts* **2015**, *134*, 76.
- [136] Zhang, Q.; Fang, W.; Xie, Y.; Cao, M.; Zhao, Y.; Shan, X.; Liu, F.; Wang, Z.; Sheng, L. Photoionization and Dissociation Study of P-Nitrotoluene: Experimental and Theoretical Insights. *J. Mol. Struct.* **2012**, *1020*, 105 – 111.
- [137] Wei, Z.; Li, J.; Wang, L.; See, S. T.; Jhon, M. H.; Zhang, Y.; Shi, F.; Yang, M.; Loh, Z.-H. Elucidating the origins of multimode vibrational coherences of polyatomic molecules induced by intense laser fields. *Nat. Commun.* **2017**, *8*, 735.
- [138] Dobratz, B. M. *The insensitive high explosive triaminotrinitrobenzene (TATB): Development and characterization, 1888 to 1994; 1995.*
- [139] Ojeda, O. U.; Çağın, T. Hydrogen Bonding and Molecular Rearrangement in 1,3,5-Triamino-2,4,6-trinitrobenzene under Compression. *The Journal of Physical Chemistry B* **2011**, *115*, 12085–12093.
- [140] Manaa, M. R.; Fried, L. E. Nearly Equivalent Inter- and Intramolecular Hydrogen Bonding in 1,3,5-Triamino-2,4,6-trinitrobenzene at High Pressure. *The Journal of Physical Chemistry C* **2012**, *116*, 2116–2122.

- [141] Zhang, C.; Wang, X.; Huang, H. -Stacked Interactions in Explosive Crystals: Buffers against External Mechanical Stimuli. *Journal of the American Chemical Society* **2008**, *130*, 8359–8365.
- [142] Liu, Y.; Yu, T.; Lai, W.; Ma, Y.; Ge, Z.; Yang, F.-L.; Liang, P.-Y.; Long, Y.; Zhou, P.-P.; Yang, Z. High-energetic and low-sensitive 1,3,5-triamino 2,4,6-trinitrobenzene (TATB) crystal: first principles investigation and Hirshfeld surface analysis. *New J. Chem.* **2021**, *45*, 6136–6143.
- [143] David Stephen, A.; Srinivasan, P.; Kumaradhas, P. Bond charge depletion, bond strength and the impact sensitivity of high energetic 1,3,5-triamino 2,4,6-trinitrobenzene (TATB) molecule: A theoretical charge density analysis. *Computational and Theoretical Chemistry* **2011**, *967*, 250–256.
- [144] Sharma, J.; Garrett, W. L.; Owens, F. J.; Vogel, V. L. X-ray photoelectron study of electronic structure, ultraviolet, and isothermal decomposition of 1,3,5-triamino-2,4,6-trinitrobenzene. *The Journal of Physical Chemistry* **1982**, *86*, 1657–1661.
- [145] Manaa, M.; Schmidt, R.; Overturf, G.; Watkins, B.; Fried, L.; Kolb, J. Towards unraveling the photochemistry of TATB. *Thermochimica Acta* **2002**, *384*, 85–90.
- [146] Williams, D. L.; Timmons, J. C.; Woodyard, J. D.; Rainwater, K. A.; Lightfoot, J. M.; Richardson, B. R.; Burgess, C. E.; Heh, J. L. UV-Induced Degradation Rates of 1,3,5-Triamino-2,4,6-Trinitrobenzene (TATB). *The Journal of Physical Chemistry A* **2003**, *107*, 9491–9494.
- [147] Xiong, Y.; Liu, J.; Zhong, F.; Xu, T.; Cheng, K. Identification of the Free Radical Produced in the Photolysis of 1,3,5-Triamino-2,4,6-trinitrobenzene (TATB). *J. Phys. Chem. A* **2014**, *118*, 6858–6863.
- [148] Zhu, J.; Lustig, D.; Sofer, I.; Lubman, D. M. Selective laser-induced resonant two-photon ionization and fragmentation of substituted nitrobenzenes at atmospheric pressure. *Analytical Chemistry* **1990**, *62*, 2225–2232.
- [149] Zhang, C.; Chen, M. Photo-induced intramolecular hydrogen transfer in ortho-nitroaniline: A matrix-isolation infrared spectroscopic and quantum-chemical study. *Journal of Molecular Structure* **2013**, *1037*, 144–147.

- [150] Tsyshevsky, R. V.; Sharia, O.; Kuklja, M. M. Molecular Theory of Detonation Initiation: Insight from First Principles Modeling of the Decomposition Mechanisms of Organic Nitro Energetic Materials. *Molecules* **2016**, *21*, 236.
- [151] Halasz, A.; Hawari, J.; Perreault, N. N. Photolysis of the Insensitive Explosive 1,3,5-Triamino-2,4,6-trinitrobenzene (TATB). *Molecules* **2022**, *27*, 214.
- [152] Reed, E. J.; Riad Manaa, M.; Fried, L. E.; Glaesemann, K. R.; Joannopoulos, J. D. A Transient Semimetallic Layer in Detonating Nitromethane. *Nat. Phys.* **2008**, *4*, 72–76.
- [153] Pellouchoud, L. A.; Reed, E. J. Optical Characterization of Chemistry in Shocked Nitromethane with Time-Dependent Density Functional Theory. *J. Phys. Chem. A* **2013**, *117*, 12288–12298.
- [154] Wu, C. J.; Fried, L. E. Ring Closure Mediated by Intramolecular Hydrogen Transfer in the Decomposition of a PushPull Nitroaromatic: TATB. *The Journal of Physical Chemistry A* **2000**, *104*, 6447–6452.
- [155] Kuklja, M. M.; Rashkeev, S. N. Self-Accelerated Mechanochemistry in Nitroarenes. *The Journal of Physical Chemistry Letters* **2010**, *1*, 363–367.
- [156] Jochim, B.; DeJesus, L.; Dantus, M. Ultrafast Disruptive Probing: Simultaneously Keeping Track of Tens of Reaction Pathways. *Rev. Sci. Instrum.* **2022**, *93*, 033003.
- [157] Epifanovsky, E.; Gilbert, A. T. B.; Feng, X.; Lee, J.; Mao, Y.; Mardirossian, N.; Pokhilko, P.; White, A. F.; Coons, M. P.; Dempwolff, A. L. et al., Software for the Frontiers of Quantum Chemistry: An Overview of Developments in the Q-Chem 5 Package. *J. Chem. Phys.* **2021**, *155*, 084801.
- [158] Grimme, S. Exploration of Chemical Compound, Conformer, and Reaction Space with Meta-Dynamics Simulations Based on Tight-Binding Quantum Chemical Calculations. *Journal of Chemical Theory and Computation* **2019**, *15*, 2847–2862, PMID: 30943025.
- [159] Pracht, P.; Bohle, F.; Grimme, S. Automated exploration of the low-energy chemical space with fast quantum chemical methods. *Phys. Chem. Chem. Phys.* **2020**, *22*, 7169–7192.

- [160] Bannwarth, C.; Caldeweyher, E.; Ehlert, S.; Hansen, A.; Pracht, P.; Seibert, J.; Spicher, S.; Grimme, S. Extended tight-binding quantum chemistry methods. *WIREs Computational Molecular Science* **2021**, *11*, e1493.
- [161] Behn, A.; Zimmerman, P. M.; Bell, A. T.; Head-Gordon, M. Efficient exploration of reaction paths via a freezing string method. *The Journal of Chemical Physics* **2011**, *135*, 224108.
- [162] Fukui, K. The Path of Chemical Reactions - The IRC Approach. *Acc. Chem. Res.* **1981**, *14*, 363–368.
- [163] Hratchian, H.; Schlegel, H. Accurate Reaction Paths Using a Hessian Based Predictor-Corrector Integrator. *J. Chem. Phys.* **2004**, *120*, 9918–9923.
- [164] Stanton, J. F.; Bartlett, R. J. The Equation of Motion Coupled-Cluster Method. A Systematic Biorthogonal Approach to Molecular Excitation Energies, Transition Probabilities, and Excited State Properties. *J. Chem. Phys.* **1993**, *98*, 7029–7039.
- [165] Dreuw, A.; Head-Gordon, M. Single-Reference ab Initio Methods for the Calculation of Excited States of Large Molecules. *Chem. Rev.* **2005**, *105*, 4009–4037.
- [166] Frisch, M.; Trucks, G.; Schlegel, H.; Scuseria, G.; Robb, M.; Cheeseman, J.; Scalmani, G.; Barone, V.; Mennucci, B.; Petersson, G.; et al, Gaussian 16 Rev. B.01. 2016.
- [167] Azhagiri, S.; Ramkumaar, G. R.; Jayakumar, S.; Kumaresan, S.; Arunbalaji, R.; Gunasekaran, S.; Srinivasan, S. Theoretical and experimental studies of vibrational spectra and thermal analysis of 2-nitroaniline and its cation. *Journal of Molecular Modeling* **2010**, *16*, 87–94.
- [168] Yi, J.; Xiong, Y.; Cheng, K.; Li, M.; Chu, G.; Pu, X.; Xu, T. A Combination of Chemometrics and Quantum Mechanics Methods Applied to Analysis of Femtosecond Transient Absorption Spectrum of Ortho-Nitroaniline. *Scientific Reports* **2016**, *6*, 19364.
- [169] Shusterman, J. M.; Gutsev, G. L.; López Peña, H. A.; Ramachandran, B. R.; Tibbetts, K. M. Coulomb Explosion Dynamics of Multiply Charged para-Nitrotoluene Cations. *The Journal of Physical Chemistry A* **2022**, *126*, 6617–6627.

- [170] Gutsev, G. L.; López Peña, H. A.; McPherson, S. L.; Ampadu Boateng, D.; Ramachandran, B. R.; Gutsev, L. G.; Tibbetts, K. M. From Neutral Aniline to Aniline Trication: A Computational and Experimental Study. *J. Phys. Chem. A* **2020**,
- [171] Chu, G.; Lu, F.; Xin, J.; Xi, T.; Shui, M.; He, W.; Gu, Y.; Xiong, Y.; Cheng, K.; Xu, T. Excited-state dynamics and electron transfer process of 1,3,5-triamino-2,4,6-trinitrobenzene. *RSC Adv.* **2016**, *6*, 55560–55567.
- [172] Feng, J.; Leszczynski, J.; Weiner, B.; Zerner, M. C. The reaction  $C_3H_3^+ + \text{acetylene}$  and the structural isomers of  $C_5H_5^+$ . *Journal of the American Chemical Society* **1989**, *111*, 4648–4655.
- [173] Glukhovtsev, M. N.; Bach, R. D.; Laiter, S. Computational Study of the Thermochemistry of  $C_5H_5^+$  Isomers: Which  $C_5H_5^+$  Isomer Is the Most Stable? *The Journal of Physical Chemistry* **1996**, *100*, 10952–10955.
- [174] Kharnaigor, K. S.; Chandra, A. K.; Lyngdoh, R. H. D. Generation, structures, relative energies, and isomerization reactions of  $C_5H_5^+$  cations. *Journal of molecular modeling* **2021**, *27*, 218–218.
- [175] Liang, K.; Tong, X.; Li, T.; Shi, B.; Wang, H.; Yan, P.; Xia, C. Enantioselective Radical Cyclization of Tryptamines by Visible Light-Excited Nitroxides. *The Journal of Organic Chemistry* **2018**, *83*, 10948–10958, PMID: 30091607.